Title
Stabilization of Alloy Anode Materials to Access High Capacities for Lithium/Sodium Ion Batteries

Author
Mazzetti, Joseph Alexander

Publication Date
2023

Peer reviewed|Thesis/dissertation

UNIVERSITY OF CALIFORNIA

Los Angeles

Stabilization of Alloy Anode Materials to Access High Capacities for Lithium/Sodium Ion Batteries

A dissertation submitted in partial satisfaction of the requirements for the degree Doctor of Philosophy in Chemistry

by

Joseph Alexander Mazzetti

2023

ABSTRACT OF THE DISSERTATION

Stabilization of Alloy Anode Materials to
Access High Capacities for Lithium/Sodium
Ion Batteries

by

Joseph Alexander Mazzetti
Doctor of Philosophy in Chemistry
University of California, Los Angeles, 2023
Professor Sarah H. Tolbert, Chair

Rechargeable battery systems are of increasing importance as the global demand for energy continues to skyrocket. Steps must be taken in regards to improving energy density and power density of battery materials in order to support a societal pivot from fossil fuel dependence to increasing reliance on renewable energy sources. This dissertation focuses on the improvement of anode materials for lithium and sodium-ion batteries with the goal of accessing higher energy densities. Alloy anode materials provide a much higher energy density than the commonly employed graphite anode, but suffer from volume expansion issues that give rise to particle pulverization and rapid capacity loss. Nanoporous architectures can be utilized to reduce this effect, as nanoporous alloy anodes have shorter lithium diffusion pathways, and reduced global

particle expansion which contributes greatly to improved cycle stability. The first part of this work details a mechanistic study for the lithiation of a multicomponent alloy anode material SbSn, and how the nanoporous architecture improves the lithiation kinetics of the active material. The nanoporous material was synthesized by a facile dealloying synthesis, and then characterized *in-situ* using X-ray diffraction (XRD) and pair distribution function (PDF) to track structural rearrangement during lithiation. XRD results demonstrate that the nanoporous system separates into Sb and Sn domains significantly faster than the bulk analog, and PDF tracks the evolution of lithiated Sn phases to determine final Sn lithation stoichiometry as amorphous Li_7Sn_3. The second chapter of this thesis focuses on the influence of amorphous intermediates on cycle stability. Sb evolves entirely through crystalline intermediates during lithiation, contrary to the fully amorphous intermediates it evolves through during sodiation. Nanoporous Sb is synthesized by a simple dealloying reaction, and then is characterized with *in-situ* transmission X-ray microscopy (TXM) and XRD. TXM images demonstrate the impressive reversibility of Sb particles during sodiation when compared to the destructive particle pulverization observed during lithiation. XRD confirms the absence of crystalline intermediates when Sb is cycled with sodium, and the amorphous nature of Sb during (de)sodiation is credited for this remarkably reversible volume expansion. The final chapter of this thesis describes a novel 3D battery cell geometry designed to enable easy access to *in-situ* tomographic datasets. 3D tomographic reconstructions provide an unprecedented glimpse into the evolution of interior structures of active particles, and provide great insight into the mechanistic behaviors of active materials. Traditional 2D cell geometries present differing beam path lengths and increasing amounts of attenuating materials when rotated, issues that are circumvented by a 3D cell geometry that remains largely unchanging even when being rotated in the X-ray beam.

The dissertation of Joseph Alexander Mazzetti is approved.

Justin R. Caram

Bruce S. Dunn

Xiangfeng Duan

Sarah H. Tolbert, Committee Chair

University of California, Los Angeles

2023

Table of Contents

LIST OF FIGURES

Chapter 2: Improving Structural and Long-Term Stability in SbSn Alloy Anodes via Control of Nanoarchitectures and Intermediates

Figure 4.3: a) SEM image of dropcast tip. b) EDX image of same dropcast tip, showing very low active Sb particle presence. c) SEM image of dipcoated tip. d) EDX image of same dipcoated tip, showing low active Sb particle present and unusual slurry structures. e) SEM image of dropcast and wicked tip. f) EDX image of same dropcast and wicked tip, showing significant active Sb particle presence. All scale bars are 100 μm.

Figure 4.4: a,b) SEM and EDX image of horizontally dried electrode. c,d) SEM and EDX image of vertically dried electrode. e,f) SEM and EDX image of electrode dried at a 45° angle. All scale bars are 200 μm.

Figure 4.5: SEM images of particles before and after electrochemical sodiation. a,b) Particle on surface of slurry that failed to sodiate, with a) pristine and b) post sodiation. c,d) Particle embedded deeper in slurry that successfully sodiated, with c) pristine and d) post sodiation. e,f) Two particles that demonstrate depth dependence on successful sodiation, with e) pristine and f) post sodiation, where red highlighted particle on surface failed to sodiate, and green highlighted particle embedded deeper in slurry successfully sodiated. All scale bars are 10 μm.

Figure 4.6: Cartoon cross-sectional representation of slurry deposited on graphite electrode tip. Active particle 1 is embedded deeper in conductive matrix and likely to demonstrate superior electrochemical performance than particle 2, which is instead only attached at slurry surface.

Figure 4.7: a) GV of bare graphite electrode, cycled in capillary cell environment. b) GV of SbSn system cycled in an ideal Swagelok cell environment. c) GV of SbSn system cycled in capillary cell environment.

Figure 4.8: 2D TXM images of Sb particle taken *in-situ* in capillary cell. a) Pristine Sb particle before lithation. b) Same particle after partial lithiation.

Figure 4.9: Galvanostat of *operando* cycling of capillary cell. Sharp highlighted plateaus indicate regions where potential was held constant during the gathering of tomographic dataset. Associated tomographic reconstructions are displayed next to the relevant galvanostat region, along with calculated particle volume for the area outlined in blue at each particle state of charge.

Figure 4.10: Interior slices into active Sb particle, heatmap gradient indicates increasing electron density. a) Interior view of pristine Sb particle. b) Interior view of same particle after undergoing partial lithation.

ACKNOWLEDGMENTS

I am endlessly thankful for all the support I have received from so many people over the years. A special thank you to my mom Anna and dad Joe who have always supported me through all the bizarre twists and turns of my unconventional path through life. Even though my dad didn't live to see the completion of this chapter, his influence will continue to be felt throughout my life. Thank you to my sister Maggie, my uncle Andrew, and Chuck for all their encouragement every time I visited home.

Thank you to my advisor Sarah Tolbert for believing in me and giving me the opportunity to work on projects that she knew would appeal strongly to my curiosity. Thank you to my committee members (Prof. Justin Caram, Prof. Bruce Dunn, Prof. Xiangfeng Duan) for all their advice and help, and in many cases our direct collaborations on battery related projects under the umbrella of the SCALAR battery center. Thank you to my mentor Andrew Dawson who taught me so much about electrochemistry and batteries. Thank you to all my collaborators and my mentees who helped on various projects, particularly Yiyi Yao and Kodi Thurber. Thank you to the beamline scientists who helped me gather a bulk of my relevant data during torturous synchrotron runs at SSRL, Jesse Ko, David Agyeman-Budu, and Johanna Nelson Weker.

I am overwhelmingly thankful for my friends from all different walks of my life who were here to support me in any capacity. Huge thank you to my amazing friends here at UCLA who kept my morale high even when times were tough, Eun Bin Go, Shanlin Hu, Charlene Salamat, and Julia Chang. A particularly special thank you to Yutong Wu and Bosi Peng, my wonderful friends who never failed to make sure I was keeping my spirits up, and were always there to introduce me to new delicious foods. Thank you to my friend from undergrad, Michael Aristov, who always checked in with me and offered advice. Thank you to Elizabeth Bracamontes, who

has supported me the entire time I have been in university, and never failed to keep a smile on my face. Thank you to Dani Dubian, for all her love and support while my dad was dying during my qualifying exams. Thank you to my friend and pseudo competitor from community college, Michelle Myers, who motivated me to overcome every single academic obstacle in my path. Thank you to my childhood friend Erich Blazeski for all the spring training and summer river trips. Thank you to Lola Chavez-Bourne, who has been through so much with me since we were children together, and has always had my back no matter what. Thank you to Tito Petch and her twin sister Janel Petch, who not only have always been incredibly supportive, but also took countless hours out from their lives over the past several years to play video games with me late into the night whenever I needed to get my mind off of work.

PREVIOUS PUBLICATIONS AND CONTRIBUTIONS OF CO-AUTHORS

Chapter 2 is a version of Yiyi Yao, Joseph Mazzetti, Kodi Thurber, David Agyeman-Budu, Johanna Nelson Weker, and Sarah H. Tolbert, "Improving Structural and Long-Term Stability in SbSn Alloy Anodes via Control of Nanoarchitectures and Intermediates." Kodi and I synthesized and characterized the raw material, fabricated electrodes, and performed electrochemical testing. Yiyi performed the *operando* XRD and *operando* PDF measurements, processed and analyzed the data. Yiyi and I wrote the manuscript. David and Johanna helped with some *operando* XRD experiments at SSRL. Prof Tolbert oversaw the research and edited the manuscript. This manuscript will be submitted for publication shortly after this dissertation is filed.

Chapter 3 is a version of Joseph Mazzetti, Andrew Dawson, Kodi Thurber, David, Agyeman-Budu, Johanna Nelson Weker, and Sarah H. Tolbert, "Understanding Stability in Nanoporous Antimony as Lithium and Sodium-Ion Battery Anodes Using *Operando* Diffraction and Microscopy." Andrew, Kodi, and I synthesized the raw material, fabricated electrodes, and performed electrochemical testing. Andrew and I performed the *operando* TXM imaging, processed and analyzed the data, and wrote the manuscript. David and Johanna helped with some *operando* TXM experiments at SSRL. Prof Tolbert oversaw the research and edited the manuscript. This manuscript will be submitted for publication shortly after this dissertation is filed.

Chapter 4 is a version of Joseph Mazzetti, Kodi Thurber, Andrew Dawson, Doran Pennington, David Agyeman-Budu, Johanna Nelson Weker, and Sarah H. Tolbert, "A Simple Capillary-Based Electrochemical Cell for 3D X-ray Nanotomography." I developed and optimized the cell design, and wrote the manscript. Andrew, Kodi, and I synthesized the raw material and fabricated the novel capillary cells for electrochemical testing, and performed *operando* TXM imaging. Doran processed and analyzed the data, and computationally created the 3D

reconstructions. David and Johanna helped with some *operando* TXM experiments at SSRL. Prof Tolbert oversaw the research and edited the manuscript. This manuscript will be submitted for publication shortly after this dissertation is filed.

VITA

2016	Provost's Research Fellowship
2017	B.S. in Chemistry from University of California, Davis
2017	Highest Honors in Research from University of California, Davis
2017-present	Electrochemical Society (ECS) Student Chapter Member, UCLA

LIST OF PUBLICATIONS AND PRESENTATIONS

1. Wang, J.; **Mazzetti, J.**; Kovnir, K.; Synthesis, crystal and electronic structures, and physical properties of a new quaternary phosphide $Ba_4Mg_{2+\delta}Cu_{12-\delta}P_{10}$ ($0 < \delta < 2$). *Inorg. Chem. Front.* **2017**, 4, 801-808.
2. Lin, T. C.; Dawson, A.; King, S. C.; Yan, Y.; Ashby, D. S.; **Mazzetti, J. A.**; Dunn, B. S.; Nelson Weker, J.; Tolbert, S. H.; Understanding Stabilization in Nanoporous Intermetallic Alloy Anodes for Li-Ion Batteries Using *Operando* Transmission X-ray Microscopy. *ACS Nano.* 2020, 14, 11, 14820-14830.
3. **Mazzetti, J. A.**; Yao, Y.; Tolbert, S. H.; Improving Structural and Long Term Stability in SbSn Alloy Anodes via Control of Nanoarchitectures and Intermediates. (*manuscript in preparation*)
4. **Mazzetti, J. A.**; Dawson, A.; Agyeman-Budu, D.; Weker, J. N.; Tolbert, S. H.; Understanding Stability in Nanoporous Antimony as Lithium and Sodium Ion Battery Anodes Using *Operando* Diffraction and Microscopy. (*manuscript in preparation*)
5. **Mazzetti, J. A.**; Thurber, K.; Dawson, A.; Pennington, D.; Agyeman-Budu, D.; Weker, J. N.; Tolbert, S. H.; A Simple Capillary-Based Electrochemical Cell for 3D X-ray Nanotomography. (*manuscript in preparation*)

CHAPTER 1: Introduction

In an increasingly energy dependent society, the ability to produce and store energy is of paramount importance. Traditional sources of energy generation, such as coal burning power plants, are steadily losing popularity due to their production of significant amounts of CO_2, while renewable sources of energy such as wind turbines and solar farms are poised to replace them. However, these sources of renewable energy are at peak efficiency at specific times of the day, and this peak efficiency often does not overlap with the times of highest demand for energy output. This disconnect between peak production and highest demand necessitates improvements to our current energy storage technology. Advancements in energy density, the quantity of charge a battery can store, and power density, the speed at which a battery can be charged or discharged, are necessary in order to enable renewable energy sources as a viable replacement for traditional fossil fuels. Lithium-ion batteries are the current face of energy storage technology, and this system must either be improved or replaced entirely to provide the superior energy and power densities that modern society demands.

Lithium-ion batteries (LIBs) were developed in 1991 by Sony Corporation, and have dominated the energy storage field for over 30 years.[1] The advent of LIBs spurred a rise in portable, rechargeable electronics such as laptop computers and personal smart phones, which have drastically transformed modern society. However, to make the significant leap from portable electronics to an effective energy grid storage system, energy and power densities need to be improved. Energy density, the total capacity of a battery to store charge per mass unit (gravimetric capacity) or per volume unit (volumetric capacity), and power density, the rate at which a battery can either be charged or discharged to produce electricity, combine to relate directly to battery efficiency. These two properties can be optimized by selecting alternate anode/cathode materials

to increase capacity, and utilizing interfacial engineering to promote fast charging/discharging. Additionally, toxicity issues with lithium mining and relatively poor global distribution of lithium resources motivates potentially replacing the lithium ion with one that is cheaper and more abundant such as Na^+ or even K^+.[2] While this is a fairly drastic step to make, sodium ion batteries (SIBs) could revolutionize the energy storage industry.

LIBs are simple in both design and principle. The anode and cathode materials are prevented from physically touching by a separator, while an electrolyte that is ionically conductive yet electronically insulating allows for the transfer of Li^+ ions. The difference in potential between the anode and cathode material is the driving force for a spontaneous redox reaction, where Li^+ ions are transferred from the anode to the cathode. In order to maintain charge balance, the transfer of these positively charged ions is accompanied by a simultaneous flow of electrons from the anode to the cathode, through an external circuit, powering a connected device. Commercial cathode materials are frequently transition metal oxides such as $LiCoO_2$ (LCO) or a stoichiometric derivative of $LiNi_xMn_yCo_zO_2$ (NMC), while anodes are often graphite.[3] This graphite anode material is capable of intercalating Li^+ ions between the carbon layers, in a stoichiometric ratio of 6 carbon atoms per single Li^+ ion.[4,5] This relatively low accommodation of Li^+ ions results in a gravimetric capacity of 372 mAh/g, which we seek to improve upon to increase energy density of LIBs.

LIB anode materials can usually be described in one of three classifications: intercalation type anodes, conversion type anodes, and alloying type anodes. Alloying anodes are typically metallic or metalloid elements such as Ge, Sb, Si, and Sn.[6] These materials are capable of forming an alloy with Li^+, which provides notably high capacities (1624 mAh/g for Ge, 660 mAh/g for Sb, 3590 mAh/g for Si, and 994 mAh/g for Sn) when compared to the intercalation type anode material

graphite (372 mAh/g).[7-10] Regrettably, this high capacity comes at a price, as the accommodation of such vast quantities of Li^+ result in significant volume expansion and contraction of active particles during cycling. For example, when alloyed with Li^+ the volume expansions of Si (280%), Sn (244%), Sb (147%), are much greater than the volume expansion seen by graphite (10%) during the Li^+ intercalation process.[11,12] This repeated process, of expansion and contraction during cycling results in particle cracking and pulverization, and eventual capacity fade. In order to access the high capacities of alloy anode materials, efforts must be undertaken to stabilize these active particles during cycling.

There are several potential methods to stabilize alloy anode particles during cycling. One efficient synthetic strategy to alleviate the volume expansion issue is the design of nanoporous architectures throughout the active particles.[13] These nanoporous materials allow for volume expansion to occur internally into the pore void space, significantly reducing global expansion of the particle while maintaining a connected, conductive network.[14] Reduced overall expansion increases particle stability and reversibility of cell redox reactions. Another strategy explored previously in this group involves the use of multicomponent intermetallic alloys to stabilize particles during volume expansion.[15] A nanoporous SbSn alloy was used since Sb and Sn metals undergo redox at different potentials (0.8V for Sb and 0.7, 0.6, and 0.5 V for Sn), allowing for the inactive component to mechanically buffer the active component during expansion and contraction. The increased stability offered by this nanoporous network and intermetallic alloy is demonstrated by a capacity retention of 595 mAh/g over 100 cycles at a rate of C/5. The phase evolution of this nanoporous intermetallic alloy during lithation is not well understood, as it consists of mostly amorphous components, and the study of this phase evolution make up a chapter of this dissertation.

Out of all the alloy anode materials, Sb demonstrates a unique characteristic of increased stability when cycled with Na^+.[16] Traditionally, since the Na^+ radius is larger than the Li^+, the volume expansion issue is exacerbated when materials are electrochemically alloyed with Na^+.[17-20] To elucidate the basis of this atypical stability, a study was conducted that combined *operando* transmission X-ray microscopy (TXM) and *operando* X-ray diffraction (XRD) to track particle expansion and phase evolution. The results of this study are presented in a chapter of this dissertation, while the observation of particularly interesting self-healing behavior in Sb particles when cycled with Na^+ motivates development of a new battery cell geometry.

TXM imaging is vital to the study of alloy anode materials, due to its ability to penetrate through all components of a cell and image high Z active particles within during normal battery operation.[21-23] This 2D imaging technique, while providing powerful insight into the volume expansion phenomenon, comes with some severe limitations. Most notably, 2D images gathered in transmission are unable to provide information about internal structure evolution during cycling. To overcome this limitation, a novel battery cell geometry was designed specifically to enable *operando* 3d TXM tomography. Reconstructing a 3D model of a particle from a series of 2D projections over a 180° angular range allows for observations to be made about the structural evolution of particle interiors, which is of particular importance for nanostructured alloy anode materials.[24,25] Traditional 2D battery cell designs increasingly attenuate X-rays when rotated in the beam, and large amounts of active particles entering the field of view obscure the particle of interest, necessitating a new 3D battery cell geometry. The design and development of this 3D battery cell is presented in the final chapter of this dissertation.

1.1 References

[1] Blomgren, G. E. The Development and Future of Lithium Ion Batteries. *J. Electrochem. Soc.* **2017,** 164, A5019.

[2] Kaunda, R. B. Potential Environmental Impacts of Lithium Mining. *Journal of Energy & Natural Resources Law.* **2020,** 38:3, 237-244.

[3] Kim, T.; Song W.; Son, D.-Y.; Ono, L. K.; Qi, Y. Lithium-ion Batteries: Outlook on Present, Future, and Hybridized Technologies. *J. Mater. Chem. A.* **2019,** 7, 2942-2964.

[4] Chang, Y.-C.; Jong, J.-H.; Fey, G. T.-K. Kinetic Characterization of the Electrochemical Intercalation of Lithium Ions into Graphite Electrodes. *J. Electrochem. Soc.* **2000,** 147 2033.

[5] Sethuraman, V. A.; Hardwick, L. J.; Srinivasan, V.; Kostecki, R. Surface structural disordering in graphite upon lithium intercalation/deintercalation. *Journal of Power Sources.* **2010,** 0378-7753.

[6] Park, C.-M.; Kim, J.-H.; Kim. H.; Sohn, H.-J. Li-alloy based anode materials for Li secondary batteries. *Chem. Soc. Rev*. **2010,** 39, 3115 – 3141.

[7] Wang, J. W.; He, Y.; Fan, F.; Liu, X. H.; Xia, S.; Liu, Y.; Harris, C. T.; Li, H.; Huang, J. Y.; Mao, S. X.; Zhu, T. Two-Phase Electrochemical Lithiation in Amorphous Silicon. *Nano Letters.* **2013,** 13 (2), 709–715.

[8] Liu, X.; Wu, X. Y.; Chang, B.; Wang, K. X. Recent Progress on Germanium-Based Anodes for Lithium Ion Batteries: Efficient Lithiation Strategies and Mechanisms. *Energy Storage Materials.* **2020**, 146–169.

[9] Cook, J. B.; Detsi, E.; Liu, Y.; Liang, Y. L.; Kim, H. S.; Petrissans, X.; Dunn, B.; Tolbert, S. H. Nanoporous Tin with a Granular Hierarchical Ligament Morphology as a Highly Stable Li-Ion Battery Anode. *ACS Appl Mater Interfaces.* **2017,** *9* (1), 293–303.

[10] Lv, H.; Qiu, S.; Lu, G.; Fu, Y.; Li, X.; Hu, C.; Liu, J. Nanostructured Antimony/Carbon Composite Fibers as Anode Material for Lithium-Ion Battery. *Electrochimica Acta.* **2015,** *151*, 214–221.

[11] Obrovac, M. N.; Chevrier, V. L. Alloy Negative Electrodes for Li-Ion Batteries. *Chem. Rev.* **2014,** 114,23,11444-11502.

[12] Moyassari E.; Roth, T.; Kücher, S.; Chang, C.-C.; Hou, S.-C.; Spingler, F. B.; Jossen, A. The Role of Silicon in Silicon-Graphite Composite Electrodes Regarding Specific Capacity, Cycle Stability, and Expansion. *J. Electrochem. Soc.* **2022,** 169, 010504.

[13] Corsi, J. S.; Welborn, S. S.; Stach, E. A.; Detsi, E. Insights into the Degradation Mechanism of Nanoporous Alloy-Type Li-Ion Battery Anodes. *ACS Energy Lett.* **2021,** 6, 5, 1749-1756.

[14] Cook, J. B.; Lin, T. C.; Detsi, E.; Nelson Weker, J.; Tolbert, S. H. Using X-ray Microscopy to Understand How Nanoporous Materials Can Be Used to Reduce the Large Volume Change in Alloy Anodes. *Nano Lett.* **2017,** 17, 2, 870-877.

[15] Lin, T. C.; Dawson, A.; King, S. C.; Yan, Y.; Ashby, D. S.; Mazzetti, J. A.; Dunn, B. S.; Nelson Weker, J.; Tolbert, S. H. Understanding Stabilization in Nanoporous Intermetallic Alloy

Anodes for Li-Ion Batteries Using *Operando* Transmission X-ray Microscopy. *ACS Nano*. **2020,** 14, 11, 14820-14830.

[16] Darwiche, A.; Marino, C.; Sougrati, M. T.; Fraisse, B.; Stievano, L.; Monconduit, L. Better Cycling Performances of Bulk Sb in Na-Ion Batteries Compared to Li-Ion Systems: An Unexpected Electrochemical Mechanism. *J. Am. Chem. Soc.* **2012,** 134, 51, 20805-20811.

[17] Liang, S.; Cheng, Y.-J.; Zhu, J.; Xia, Y.; Müller-Buschbaum, P. A Chronicle Review of Nonsilicon (Sn, Sb, Ge)-Based Lithium/Sodium-Ion Battery Alloying Anodes. *Small Methods.* **2020,** 4, 2000218.

[18] Xu, Y.; Zhu, Y.; Liu, Y.; Wang, C. Electrochemical Performance of Porous Carbon/Tin Composite Anodes for Sodium-Ion and Lithium-Ion Batteries. *Adv. Energy Mater.* **2013,** 3, 128-133.

[19] Han, Z.-J.; Yamagiwa, K.; Yabuuchi, N.; Son, J.-Y.; Cui, Y.-T.; Oji, H.; Kogure, A.; Harada, T.; Ishikawa, S.; Aoki, Y.; Komaba, S. Electrochemical lithiation performance and characterization of silicon-graphite composites with lithium, sodium, potassium, and ammonium polyacrylate binders. *Phys. Chem. Chem. Phys.* **2015,** 17, 3783-3795.

[20] Perveen, T.; Siddiq, M.; Shahzad, N.; Ihsan, R.; Ahmad, A.; Shahzad, M. I. Prospects in anode materials for sodium ion batteries – A review. *Renewable and Sustainable Energy Reviews.* **2020,** 119, 109549.

[21] Wu, Y.; Liu, N. Visualizing Battery Reactions and Processes by Using *In Situ* and *In Operando* Microscopies. *Chem.* **2018,** 4, 3, 438-465.

[22] Chao, S.-C.; Song, Y.-F.; Wang, C.-C.; Sheu, H.-S.; Wu, H.-C.; Wu, N.-L. Study on Microstructural Deformation of Working Sn and SnSb Anode Particles for Li-Ion Batteries by in Situ Transmission X-ray Microscopy. *J. Phys. Chem.* **2011,** 115, 44, 22040-22047.

[23] Chao, S.-C.; Yen, Y.-C.; Song, Y.-F.; Chen, Y.-M.; Wu, H.-C.; Wu, N.-L. A study on the interior microstructures of working Sn particle electrode of Li-ion batteries by in situ X-ray transmission microscopy. *Electrochemistry Communications.* **2010,** 12, 2, 234-237.

[24] Liu, D.; Shadike, Z.; Lin, R.; Qian, K.; Li, H.; Li, K.; Wang, S.; Yu, Q.; Liu, M.; Ganapathy, S.; Qin, X.; Yang, Q.-H.; Wagemaker, M.; Kang, F.; Yang, X.-Q.; Li, B. Review of Recent Development of In Situ/Operando Characterization Techniques for Lithium Battery Research. *Adv. Mater.* **2019,** 31, 1806620.

[25] Tang, F.; Wu, Z.; Yang, C.; Osenberg, M.; Hilger, A.; Dong, K.; Markötter, H.; Manke, I.; Sun, F.; Chen, L.; Cui, G. Synchrotron X-Ray Tomography for Rechargeable Battery Research: Fundamentals, Setups and Applications. *Small Methods*. **2021,** 5, 2100557.

CHAPTER 2: Improving Structural and Long-Term Stability in SbSn Alloy Anodes via Control of Nanoarchitectures and Intermediates

2.1: Abstract.

Multi-component alloy anode material SbSn is synthesized and nanostructured with a nanoporous architecture. This nanostructure provides pore void space for the particle to expand into during electrochemical lithiation, and helps mitigate particle pulverization and long term capacity fade. To gain an understanding into how this nanostructure affects the chemical mechanism of lithation, in addition to the formation and persistence of crystalline and amorphous intermediates, *operando* X-ray diffraction and pair distribution function analysis were utilized. The nanoporous architecture significantly improves the kinetics of electrochemical cycling, promoting easy separation of the alloy into Sb and Sn domains for lithiation. The nanoporous sample also remains largely amorphous after the first cycle, providing greater ductility for increased particle stability during expansion and contraction. Pair distribution function provides a glimpse into short range order during these lithiation events, and tracks the formation of the amorphous, under lithiated Li_7Sn_3 phase that forms at the lithiation cut-off potential.

2.2: Introduction.

Lithium-ion batteries (LIB) have demonstrated enormous success in powering our everyday portable electronics such as smartphones and laptops.[1-3] However, as we look towards future applications such as electric vehicles and smart electrical grids, significant advancements in energy density are required.[4-6] Graphite is currently the most popular anode material of choice, providing a gravimetric capacity of 372 $mAh \cdot g^{-1}$ with a one electron intercalation reaction to form LiC_6, but charging beyond this capacity can lead to problems such as Li metal plating.[7-9] Therefore,

to increase the cell energy density, it would be advantageous to utilize a material that can reversibly accommodate more than one Li-ion.

Alloy anode materials are an attractive candidate to replace graphite, as they are typically metalloid or metallic elements such as Si, Ge, Sn, Sb, Pb, or Bi that alloy with Li^+, which allows them to accommodate several more Li^+ per unit cell than an intercalation material.[10-12] This charge storage mechanism affords alloy anodes much higher gravimetric and volumetric capacities. For reference, Si, Sn, and Sb can provide 3579 mAh/g, 990 mAh/g, and 660 mAh/g, respectively.[13,14] However, since the Li^+ insertion forms an alloy with the material, huge structural rearrangements and volume expansion are induced. Again, Si, Sn, and Sb undergo 280%, 260%, and 147% volume expansion, respectively.[15] Repeated cycling causes mechanical stress, crack formation, which leads to disconnection of active material from the current collector and capacity fade. Therefore, significant research efforts have been focused on strategies for alleviating the volume expansion issue.

Previous work in our group has demonstrated the synthesis of a nanoporous antimony-tin (SbSn) intermetallic through de-alloying reaction and used transmission x-ray microscopy (TXM) to show that the volume expansion is less severe and more reversible than in pure Sn.[16-18] The nanoporous structure allows the material to expand into the pore volume while maintaining a connected network during lithiation. Because Sb and Sn can both alloy with Li^+, but at different voltages, one component acts an inactive matrix to buffer the volume expansion during lithiation of the other.[19] Sn affords a large gravimetric capacity of 990 mAh/g, while Sb undergoes a relatively smaller volume expansion (147%) compared to other alloying materials. Therefore, the combined intermetallic crystal structure and nanoporous architecture enable more reversible lithiation behavior and mitigate long-term capacity fade due to volume expansion.

However, we still have a limited understanding of the dynamic structural changes that occur during lithiation and de-lithiation because much of the material becomes very disordered and nearly amorphous after the first cycle. The extent of lithiation of Sn is unclear because several higher lithiated Sn phases are reported to be stable in pure Sn (e.g. Li_7Sn_3, Li_5Sn_2, $Li_{13}Sn_5$, Li_7Sn_2, $Li_{17}Sn_4$, and $Li_{22}Sn_5$) but have not been demonstrated in the intermetallic.[20-22] Therefore, we have performed a combined *operando* x-ray diffraction (XRD) and pair distribution function analysis (PDF) study on our nanoporous SbSn electrode to determine crystalline phases formed *in situ*, as well as local structure of the remaining disordered material.

The x-ray total scattering (TS) / pair distribution function analysis (PDF) method collects both Bragg scattering and diffuse scattering from the material up to high Q ~ 25 $Å^{-1}$, where Q is the scattering vector and related to the lattice spacing, d, and scattering angle, θ, by the equation: $Q = \frac{4\pi}{\lambda} sin(\theta) = \frac{2\pi}{d}$.[23] Bragg scattering is the diffraction signal due to the crystalline materials with long-range order, while diffuse scattering comes from elastic scattering of disordered or nanostructured materials. By taking the Fourier transform of the TS intensity, we obtain the pair distribution function (PDF), which effectively gives a histogram of all atom-atom correlations within the material, regardless of long-range order.[24,25] Therefore, PDF allows us to characterize the structure of amorphous material formed during lithiation and de-lithiation.[26-29]

In this work, we have synthesized both a bulk and nanoporous SbSn alloy anode to understand the effect of nanoscale architecture on improving the kinetics of phase separation and re-mixing of the alloy during cycling. We also characterize both crystalline and amorphous intermediates formed with paired *operando* XRD and PDF. We demonstrate that the phase-separation of nanoporous SbSn into crystalline Li_3Sb and β-Sn during first lithiation of Sb is much more facile than in the bulk, suggesting that the nanoporous structure by shortening the distance

which Li^+ must travel to form domain of Li_3Sb. In the *operando* XRD, we do not observe any crystalline lithiated tin phases in the final product, but through *operando* PDF, we have determined that the amorphous lithiated tin phases resemble Li_7Sn_3 in the short-range. We postulate that the amorphous nature of the lithiated tin phase provides an additional ductile matrix to buffer volume expansion during cycling.

2.3: Experimental

2.3.1. Synthesis of bulk SbSn alloy:

A parent alloy of $Sb_{20}Sn_{80}$ was synthesized by melting the stoichiometric amounts of Sb metal and Sn metal in a quartz ampule under Ar at 700°C, then cooled to room temperature. To make a homogeneous alloy, the alloy was then heated and cooled several times at 400 °C. The extra Sn in the parent alloy was then etched away with a 4 M HBr.

2.3.2. Synthesis of nanoporous SbSn alloy:

Stoichiometric ratios of elemental Sn and Sb are mixed in a quartz ampule and placed in a 700˚C oven for five days to achieve a 55:45 Sb:Sn ratio alloy, which is the intermetallic phase. This intermetallic SbSn is then cryomilled. 10 mL of room temperature 5.93M HBr is introduced to the cryomilled SbSn powder. (30mgs yields ~12mgs of NP-SbSn and 20mgs ~ 8mgs) After 30 minutes of selective dealloying, the reaction is quenched with water and rinsed extensively with deionized water. The powder is dried in the Schlenk vacuum line to remove residual water.

2.3.3. Material Characterization:

Scanning electron microscopy (SEM) images and energy dispersive spectroscopy (EDS) data were obtained using a JEOL model 6700F electron microscope. X-ray diffraction (XRD) patterns were collected with a PANalytical X'Pert Pro diffractometer operating with Cu Kα (λ = 1.5418 Å) using a 0.05° step size, an accelerating voltage of 45 kV, and a current of 40 mA.

2.3.4. Electrode fabrication and electrochemical characterization:

The nanoporous (NP) SbSn slurries were fabricated in a 70:15:15 ratio of active material: carbon nanofibers: carboxymethylcellulose (CMC), which is added as a 3% by weight solution in water. Each solid component (active and carbon fibers) is weighed and ground in a mortar and pestle. Once the powder is homogenous, 2 drops of deionized (DI) water are added to the mortar and pestle, then mixed. Then, the CMC solution is added and mixed in to create a more homogenous slurry. Drops of DI water are added until the proper viscosity is achieved. The slurry is cast with a doctor blade at 25 μm thickness onto Cu foil, which is first cleaned with isopropanol (IPA). The slurry is then allowed to ambiently dry, and the corners of the Cu foil are weighed down to prevent wrinkling. After ambient drying overnight, another glass casting sheet is placed over the slurry to sandwich the slurry between two casting sheets. This sandwich is then crimped together with binder clips and placed into the 80˚C oven overnight. Electrode discs with area of 0.71 cm^2 were punched out and assembled inside an Ar-filled glovebox into 2032 coin cells with 2 stainless steel spacers, a stainless steel spring, and a glass fiber separator. Polished Li foil was used as the counter and reference electrode. Commercial grade 1 M $LiPF_6$ in 1:1 ethylene carbonate (EC): dimethylene carbonate (DMC) was purchased from Sigma-Aldrich and used as the electrolyte. Cyclic voltammetry (CV) experiments were performed at 0.1 mV/s sweep rate from

1.5 V to 0.05 V. Galvanostatic cycling (GV) was performed at a C/5 current density from 2.0 V to 0.05 V. Potentiostatic electrochemical impedance spectroscopy (PEIS) measurements were taken in the frequency range from 900 kHz to 100 mHz with a 10 mV input. EIS data was taken at open-circuit voltage (OCV), which was approximately 1.5 to 2.0 V in the pristine state, in the fully lithiated state at 0.05V, and in the delithiated state at 2.0 V. A 15 minute potentiostatic hold at each state of charge was applied before each EIS measurement to ensure decay of residual current and equilibrium conditions. EIS Nyquist plots were fit to the equivalent circuit $R_1 + \frac{Q_2}{R_2} + Q_3$ in the ZFit module of EC-Lab software from Biologic.

2.3.5. *Operando* XRD:

Operando diffraction experiments were conducted at Stanford Synchrotron Radiation Lightsource (SSRL). Pouch cells were made of aluminized mylar, Ni and Al leads, and glass fiber separator. 1M $LiPF_6$ in EC:DMC was used as electrolyte. Li metal was used as counter and reference electrode. Pouch cells were pressurized using beryllium windows during operation. X-ray energy at SSRL beamline 11-3 was 12.7 keV (λ = 0.9763 Å). Exposure time to x-rays at SSRL ranged from 30 – 60 seconds. LaB_6 placed at the same sample-to-detector distance as the electrodes was used as calibration standard. Data integration and reduction was performed using GSAS-II.[30] Peak fitting was performed in Igor. Nanoporous and bulk SbSn were cycled at C/4 during *operando* XRD.

2.3.6. *Operando* PDF:

Operando total scattering / pair distribution function (PDF) analysis experiments were conducted at the Advanced Photon Source (APS) beamline 11-ID-C. Samples were pressed into

pellet electrodes with a composition of 60% active material, 20% carboxymethylcellulose (CMC) as binder, and 20% vulcan black. Pellet electrodes were loaded in AMPIX cells with glassy carbon windows to allow for conductivity and x-ray transparency.[31,32] Cells were constructed using Li metal as counter and reference electrode, glass fiber separator, and 1M $LiPF_6$ in EC:DMC as electrolyte. X-ray energy of 105.7 keV (λ = 0.1173 Å) was used. CeO_2 was used as a calibration standard. Exposure time to collect each pattern was approximately 5 minutes. Cycling in AMPIX cells was done galvanostatically at C/10. Scattering due to Li metal was masked away during 2D integration. Scattering due to electrolyte, separator, and glassy carbon was subtracted away to minimize interference in the G(r).

2.3.7. PDF Simulations:

PDFgui was used to simulate reference phase PDF patterns and refine structural parameters of experimental PDF data. Refinements were carried out in the G(r) range of 0 – 18 Å. Values of Q_{damp} = 0.038 and Q_{braod} = 0.02 were used to correct for instrument broadening. Crystal structure of SbSn alloy with tetragonal unit cell in space group P4/mmm (a = b = 3.075 Å, c = 6.259 Å, $\alpha = \beta = \gamma = 90^{\circ}$) was obtained from the Materials Project Database (mp ID: 1218920).[33] Crystal structure of β-Sn formed during cycling was obtained from Materials Project Database (mp ID: 84, ICSD: 236667). Crystal structure of Li_3Sb was obtained from Materials Project Database (space group Fm3m, mp ID: 2074). Crystal structures for Li_2Sn_5 (mp ID: 7924) and Li_7Sn_3 (mp ID: 30768) were obtained from the Materials Project Database. Single phase scale factor refinements were also performed on Li_2Sb, LiSn, Li_5Sn_2, Li_7Sn_2, $Li_{13}Sn_5$, $Li_{17}Sn_4$, and $Li_{22}Sn_5$ to determine whether any other lithiated antimony or lithiated tin phases were formed in *operando*,

but no evidence was found for the presence of these phases. Unit cell and bond distance visualizations were performed using VESTA.[34]

2.4: Results and Discussion

2.4.1. Material Characterization

From SEM images (**Figure 2.1**), we can see that the dealloying reaction produces particles with well-dispersed porosity with pores on the order of 30 nm in diameter. The porosity allows flexibility for volume expansion during cycling while maintaining an electrically connected network and enable better electrolyte penetration. EDS measurements show a 55:45 ratio of Sb:Sn in the product, which is within the intermetallic range.

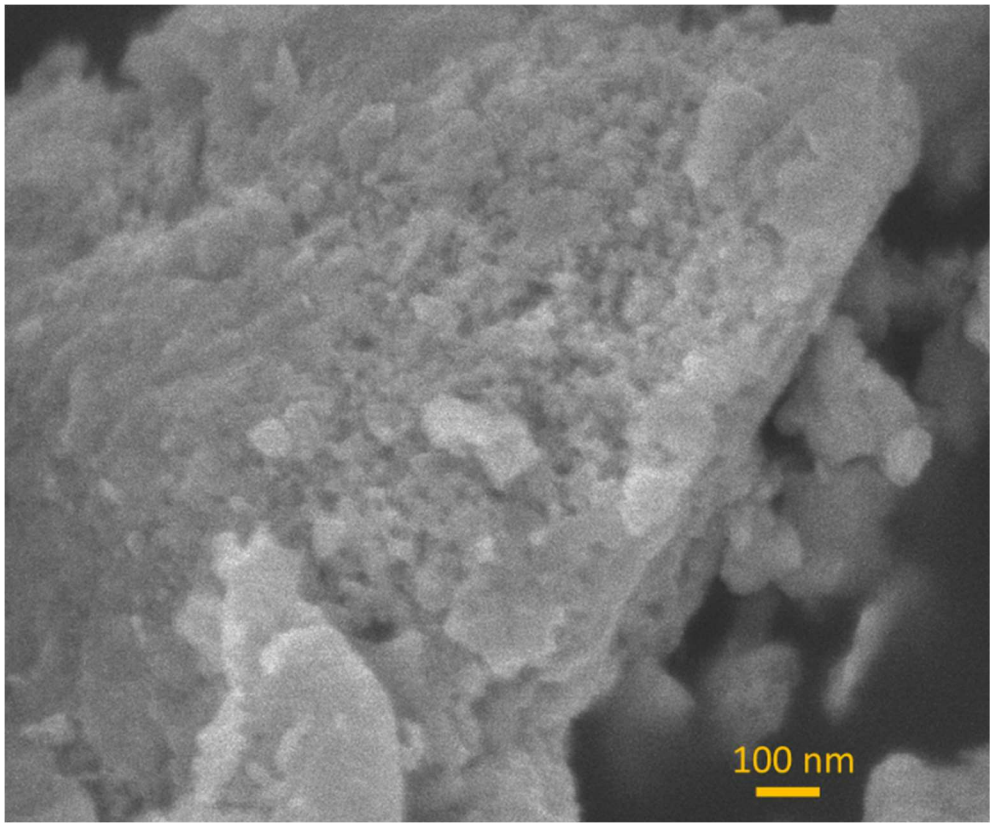

Figure 2.1. SEM image of nanoporous SbSn.

2.3.2. Electrochemical Characterization

The bulk and nanoporous SbSn were fabricated into slurry electrodes for electrochemical testing. Cyclic voltammetry (CV) was performed at 0.1 mV/s sweep rate to identify the redox processes (**Figure 2.2a**). On the reduction scan, the peak at 0.78 V corresponds to the lithiation of Sb, and subsequent three peaks at 0.68, 0.52, and 0.40 V correspond to lithiation of the Sn. On the oxidation scan, delithiation of Sn occurs at 0.65, 0.74, and 0.80 V. Interestingly, the delithiation of Sb has split into two peaks at 1.04 and 1.08 V. However, by cycle 10, the first Sb delithiation peak has declined in intensity and all peaks appear broadened. This hysteresis observed in the CV suggests that lithiation and delithiation mechanisms are not the same. Galvanostatic cycling (GV) was also performed at C/5 (Figure 5.2b) to measure charge and discharge capacity. As expected, the lithiation GV shows four plateaus corresponding to the four reduction peaks in CV, and delithiation GV shows five plateaus corresponding to the five oxidation peaks in CV.

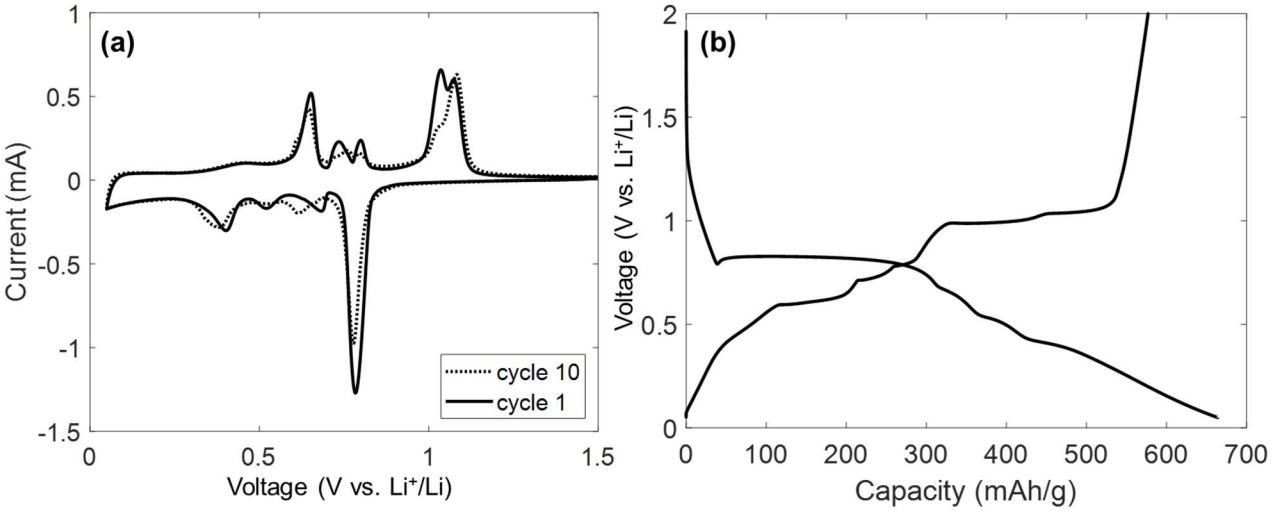

Figure 2.2 (a) CV of bulk SbSn during first and tenth cycle taken at 0.1 mV/s. (b) galvanostatic charge and discharge (GV) curves for bulk SbSn at C/5.

To measure the conductivity at different states of charge, electrochemical impedance spectroscopy (EIS) was performed (**Figure 2.3**) on bulk SbSn in the pristine state at open-circuit voltage (OCV), in the fully lithiated state at 0.05 V, and in the delithiated state 2.0 V. The EIS spectrum in the pristine state was fit to an equivalent circuit ($R_1 + \frac{Q_2}{R_2} + Q_3$) and the charge transfer resistance was determined to be 44 Ohm. In the fully lithiated state, we observe two semicircles, indicating that two distinct charge transfer processes are happening in the material. We attribute these two redox processes to charge transfer through the crystalline Li_3Sb and amorphous lithiated Sn product that are phase separated (see below discussion of *operando* XRD and PDF). Since the impedance shows two charge transfer events in fully lithiated state, the spectrum was fit to equivalent circuit ($R_1 + \frac{Q_2}{R_2} + \frac{Q_3}{R_3}$), and the two charge transfer resistances were calculated to be R_2 = 45 Ohm and R_3 = 82 Ohm. Interestingly, the delithiated state has the lowest charge transfer resistance of 25 Ohm, although it contains significantly more amorphous material, suggesting that the delithiated material is well-mixed for uniform metallic conductivity.

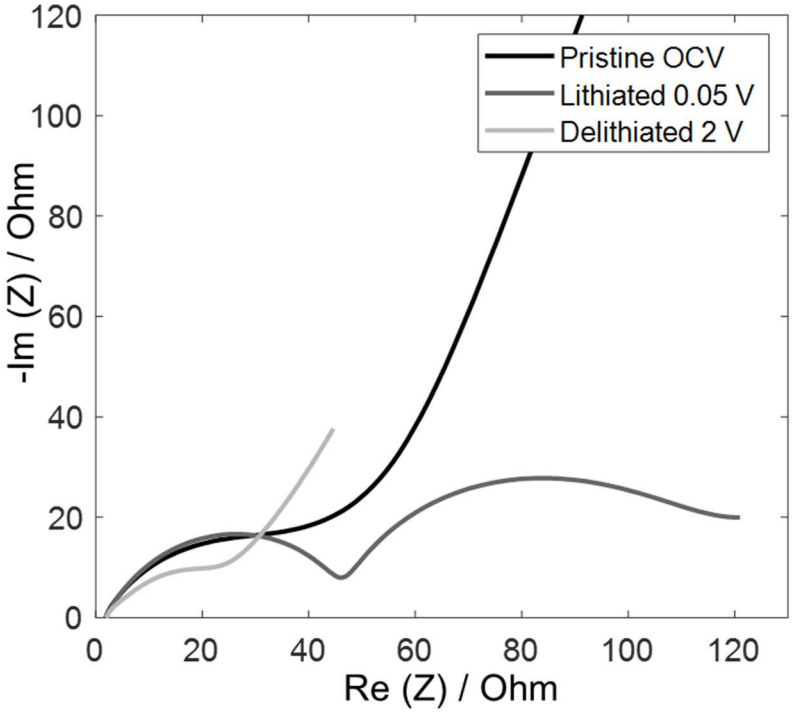

Figure 2.3. Nyquist plot of bulk SbSn EIS taken in the pristine, lithiated, and delithiated state.

2.4.3. *Operando* XRD

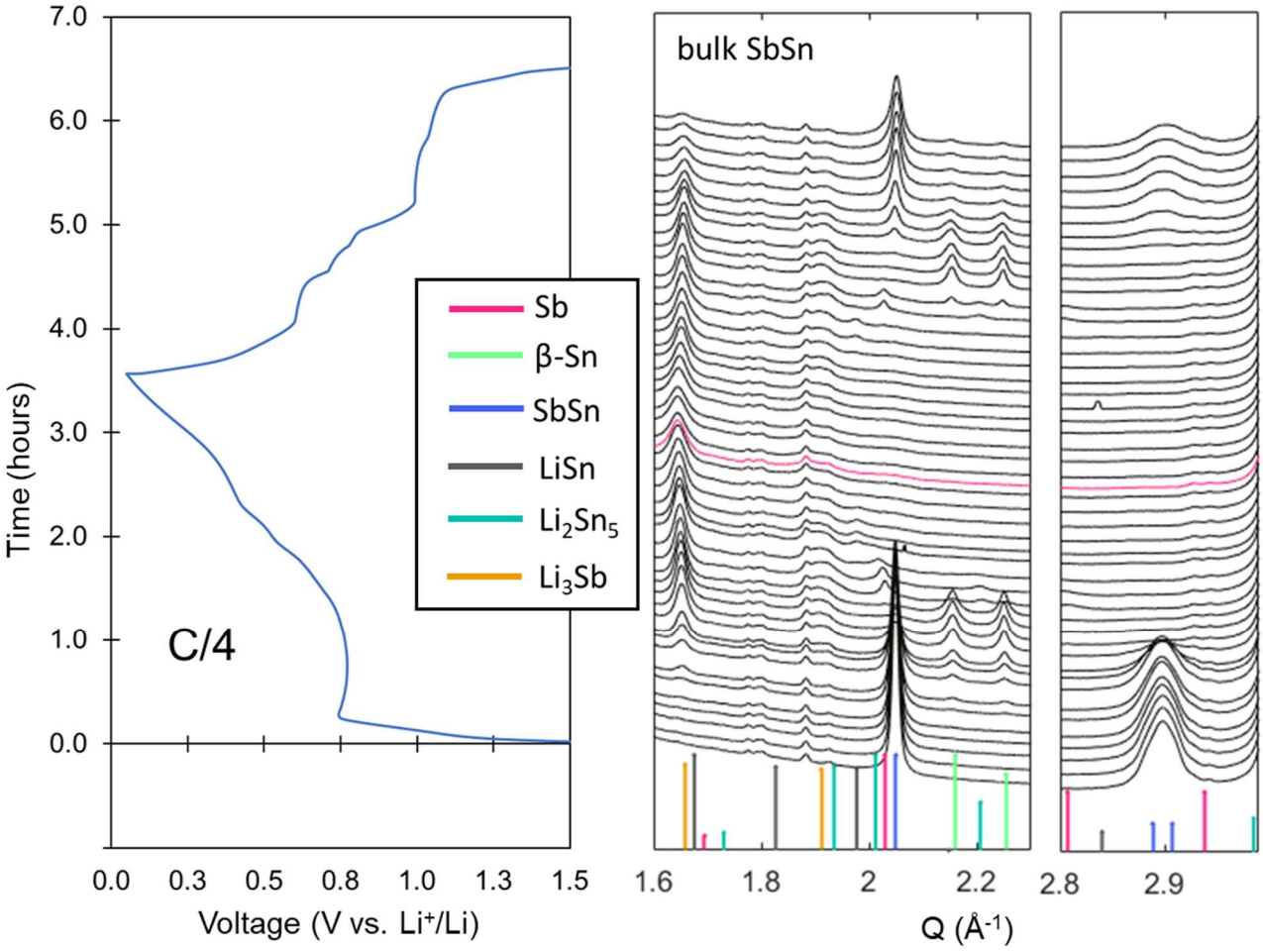

Figure 2.4. *Operando* XRD of bulk SbSn cycled with Li^+ at C/4. Reference pattern for Sb (pink) is shown to demonstrate that the material begins as a pure alloy with no phase separation of Sb and Sn. Reference pattern for LiSn (grey) is used to verify that no observable LiSn is formed in *operando*.

Bulk SbSn

The *operando* XRD (**Figure 2.4**) shows that the electrode material begins as a pure SbSn alloy with peaks at Q = 2.05, 2.89, and 2.91 $Å^{-1}$. No peaks for Sb are observed in the first scan, indicating no phase separation of Sb or Sn. As the lithiation proceeds, the plateau at 0.8 V (vs. Li^+/Li) corresponds to the lithiation potential of Sb. This can be seen simultaneously with the appearance of Li_3Sb peaks at Q = 1.66 and 1.91 $Å^{-1}$, while the Sn phase separates out of the alloy, forming domains of β-Sn, showing peaks at Q = 2.16 and 2.25 $Å^{-1}$. After the initial appearance of the Li_3Sb peak at 1.66 $Å^{-1}$, the peak shifts to smaller Q (larger d-spacing) as lithiation continues. By fitting the peak positions to calculate d-spacing, we find that the Li_3Sb undergoes at 0.7% lattice expansion during insertion of Li^+. Once lithiation of Sb is complete, the lithiation of Sn begins at plateaus 0.6, 0.5, and 0.4 V. As Li^+ is inserted into Sn, the Sn metal peaks disappear. Some small peaks at Q = 1.94 and 2.01 $Å^{-1}$ appear that may correspond to a Li_2Sn_5 intermediate. As further lithiation proceeds, these peaks disappear, and no new peaks appear. Reference pattern for LiSn has been plotted (Figure 5.4, grey) to show this crystalline phase does not form. Other phases with higher stoichiometry of Li:Sn, such as Li_5Sn_2, $Li_{13}Sn_5$, Li_7Sn_2, and $Li_{22}Sn_5$, were also compared and no matching peaks were found. The lack of crystalline lithiated Sn phase peaks at the end of lithiation indicates that the highest lithiated Sn phase is amorphous. During de-lithiation, the reverse pathway is taken, as peaks for Li_2Sn_5 and β-Sn intermediates appear and disappear again. The SbSn alloy is reformed at the end of delithiation, but not to the same initial degree of crystallinity. Comparing peak areas of the SbSn peak at Q = 2.05 $Å^{-1}$ in first scan at OCV to the last scan at 1.5 V, 24% of the bulk SbSn alloy is recovered.

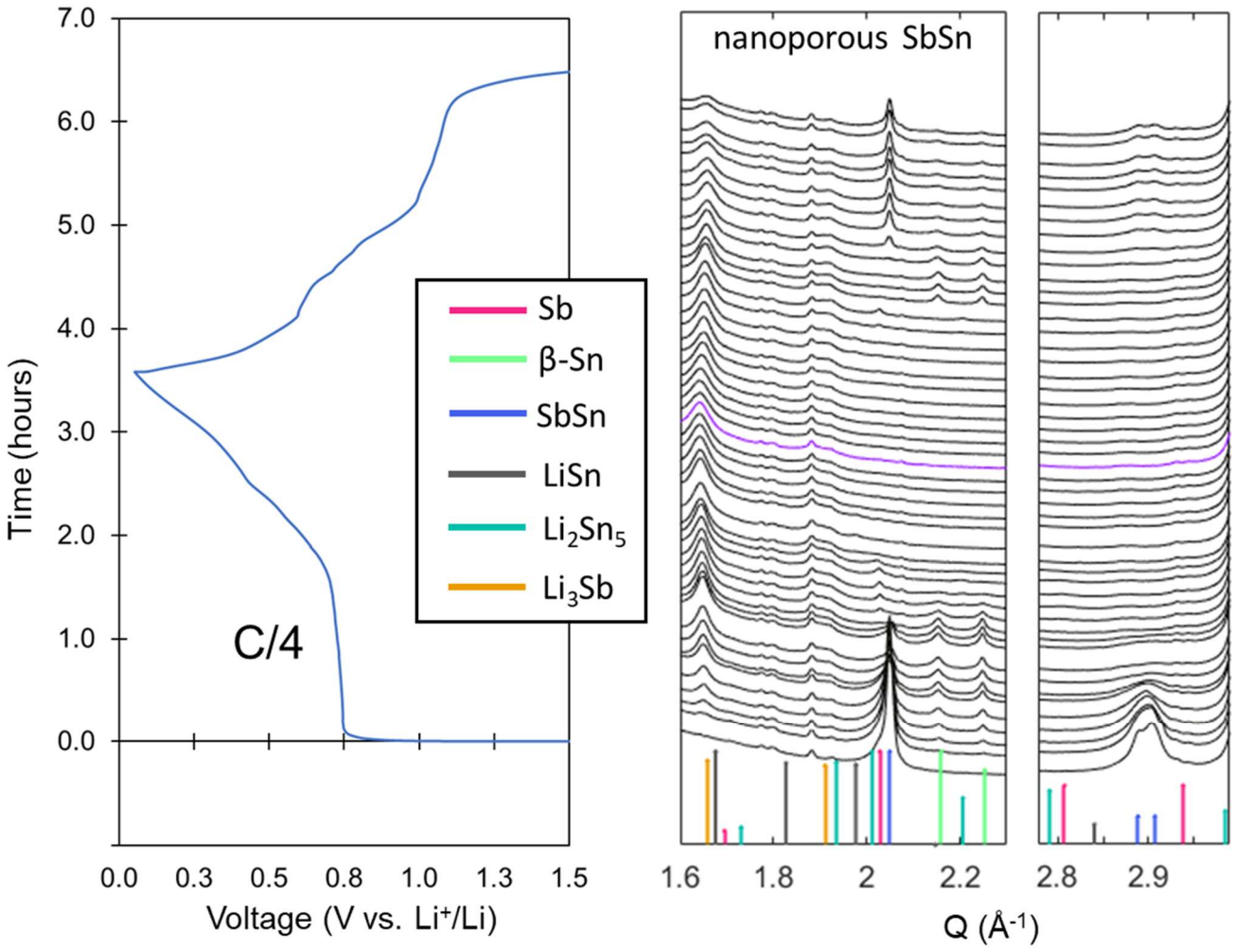

Figure 2.5. *Operando* XRD of nanoporous SbSn cycled with Li^+ at C/4. Reference pattern for Sb (pink) is shown to demonstrate that the material begins as a pure alloy with no phase separation of Sb and Sn. Reference pattern for LiSn (grey) is used to verify that no observable LiSn is formed in *operando*.

Nanoporous SbSn

The same phase evolution behavior is observed in the *operando* XRD of nanoporous SbSn (**Figure 2.5**). However, it can be noted that the Li_3Sb and β-Sn phases appear at an earlier time in the nanoporous SbSn compared to the bulk SbSn. This suggests that lithiation of the Sb in the

nanoporous alloy is more facile than in the bulk due to easier phase separation into nanoscale domains. The 1.66 $Å^{-1}$ peak of Li_3Sb also shifts to the left as lithiation proceeds, resulting in a 1% lattice spacing expansion. This value is larger than the 0.7% expansion that the Li_3Sb in bulk SbSn experiences, supporting the idea that the nanoporous architecture is able to accommodate more strain. The lithiation plateaus in the GV of nanoporous SbSn (Figure 5.5) are not as sharply defined as those observed in bulk , which is a commonly observed behavior for nanomaterials as the distribution of redox potentials is broadened and the material can accommodate more strain. Comparing peak areas of the SbSn peak at Q = 2.05 $Å^{-1}$ in first scan at OCV to the last scan at 1.5 V, 11% of the nanoporous SbSn alloy is recovered. Therefore, more of the bulk SbSn is able to re-alloy after de-lithiation than in the nanoporous material. The Li_3Sb peak at 1.66 $Å^{-1}$ has not completely disappeared in the last scan, indicating some Sb has not been fully delithiated.

Again, no peaks corresponding to lithiated Sn phases appear at the end of lithiation, demonstrating that the fully lithiated Sn is amorphous. This discovery is notable since several crystalline lithiated Sn phases have been reported, including Li_2Sn_5, LiSn, Li_7Sn_3, Li_5Sn_2, $Li_{13}Sn_5$, Li_7Sn_2, $Li_{17}Sn_4$, and $Li_{22}Sn_5$.[35] An *operando* XRD study by Frerichs *et al*. showed that lithiation of Sn nanoparticle-based electrodes results in the formation of crystalline Li_2Sn_5 and LiSn phases.[36] However, our operando XRD on the SbSn intermetallic only shows evidence for Li_2Sn_5 phase, suggesting that the crystallization of higher Li-content Sn phases is frustrated by the presence of the surrounding Li_3Sb matrix.

2.4.4. *Operando* PDF

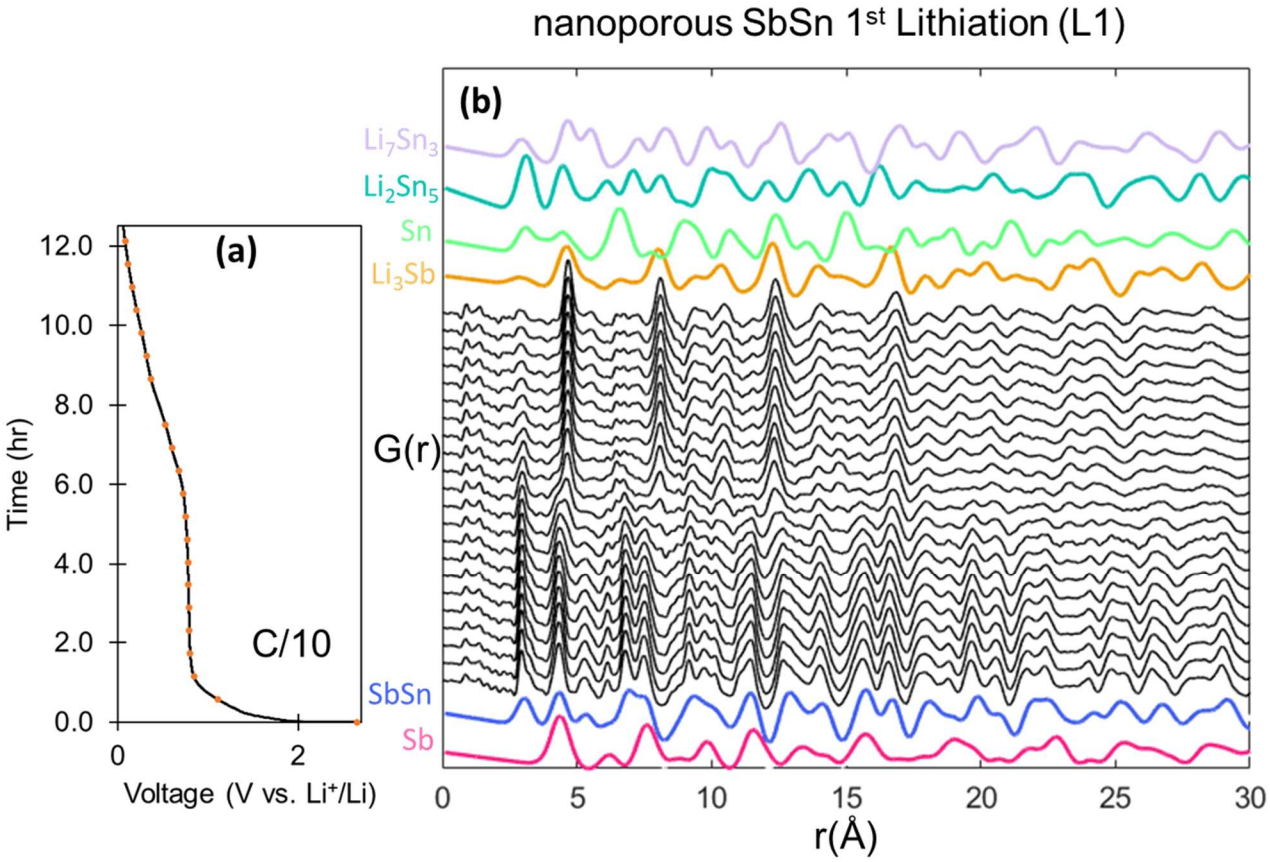

Figure 2.6. *Operando* PDF of nanoporous SbSn cycled with Li^+ at C/10. (a) First lithiation GV curve and (b) normalized operando PDF during first lithiation with simulated reference PDF patterns for Sb, SbSn, Li_3Sb, β-Sn, Li_2Sn_5, and Li_7Sn_3. Orange dots indicate voltages where PDF scans were taken.

The significant amount of amorphous material formed during cycling of SbSn makes unequivocal phase identification by XRD challenging. In particular, the nanoporous SbSn is only able to recover 11% of the original alloy. Therefore, we turn to *operando* PDF to give complementary structural information about the amorphous phases formed during cycling. The first scan matches well with the PDF pattern of SbSn alloy (**Figure 2.6b**), as expected. In the

reference pattern for SbSn, the first peak at r = 3.06 Å corresponds to a nearest neighbor Sb-Sn bond length assuming that the alloy is perfectly uniform and all Sb-Sn bonds are equal length. The relative contribution of Sn-Sb compared to Sb-Sb (or Sn-Sn) contributions to each PDF peak can be decomposed in the simulation (**Figure 2.7**). In the experimental data, the sharp peak at 2.95 Å and shoulder at 3.24 Å in the first scan suggests that the alloy is not atomically uniform and there are two distributions of nearest neighbor bonds, likely a result of annealing conditions during synthesis. In the middle of the PDF series, and at the end of 0.8 V plateau, we can see the loss of crystallinity and long-range order as the PDF peaks at r > 20 Å disappear. For the sake of discussion, we consider r = 0 – 18 Å as "short-range" and r > 20 Å as "long-range". At the end of the 0.8 V plateau (Figure 5.6a), the short-range peaks corresponding to SbSn disappear and peaks resembling Li_3Sb (orange) appear at r = 4.65, 8.09, 12.33, and 16.8 Å. As the lithiation of Sb is completed, the crystallinity is restored, as peaks appear again at r > 20 Å corresponding to Li_3Sb. These observations are consistent with the *operando* XRD (Figure 5.5), as Li_3Sb peaks appear towards the end of the 0.8 V plateau. Furthermore, as lithiation of the Sn proceeds (after 0.8 V plateau and after 6 hrs), the long-range PDF does not change at all, indicating that no new crystalline phases are being formed. Again, this data is consistent with the *operando* XRD which does not show any new peaks forming during lithiation of Sn, confirming that the lithiated Sn is amorphous. Because PDF gives all atom-atom correlations within the materials, the bonds in the amorphous lithiated Sn phase can still be identified to give some picture of structure. Specifically, a peak at 5.54 Å begins to grow during lithiation of Sn **(Figure 5.6b)**.

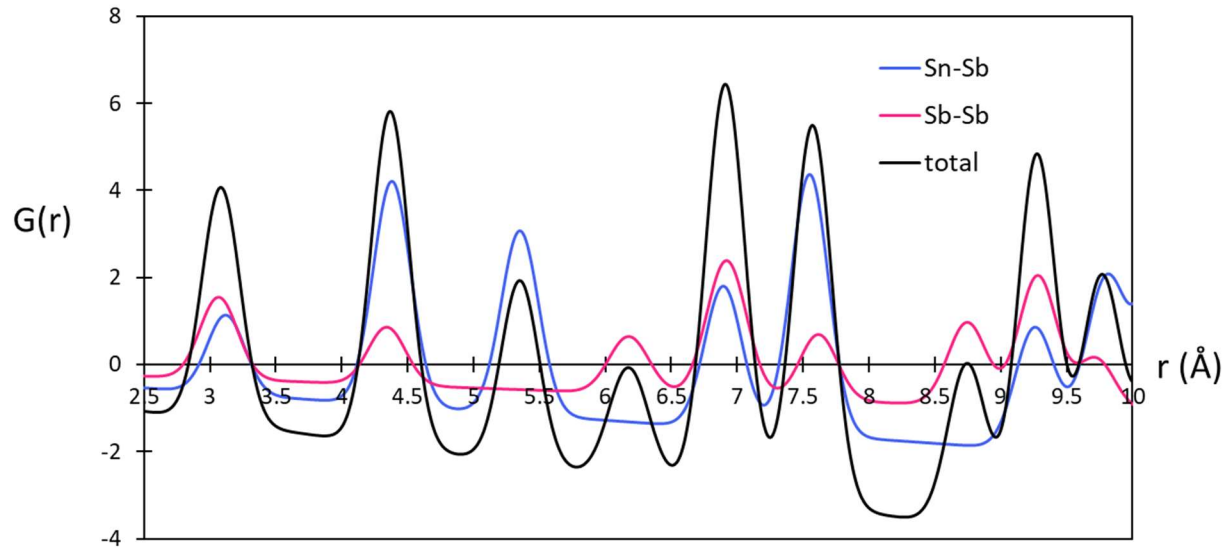

Figure 2.7. Simulated PDF for SbSn alloy (black) with partial PDF from Sn-Sb correlation contributions (blue) and Sb-Sb contributions (pink).

As the appearance and disappearance of several phases overlap in time, it becomes difficult to assign peaks in the PDF to distinct phases. Therefore, we have carried out multi-phase refinement on the scale factor of G(r) using PDFgui to quantify amounts of each phase during cycling (**Figure 2.8**). Based on the *operando* XRD, the presence of crystalline phases of SbSn, β-Sn metal, and Li_3Sb has been established. This is also confirmed in the multi-phase refinement of the PDF patterns. The active material begins as 80% SbSn alloy which decreases as lithiation proceeds. β-Sn is formed as an intermediate as the Li_3Sb phase separates out, but is consumed as Sn starts to lithiate. We also include additional phases of Li_2Sn_5 and Li_7Sn_3 to determine if the local structure of lithiated Sn formed in *operando* resembles any of these phases. The presence of Li_2Sn_5 as an intermediate, which was suggested by *operando* XRD but unclear due to low signal, is confirmed by multi-phase fitting of the PDF. Interestingly, as the Li_2Sn_5 intermediate breaks down and disappears, an amorphous phase resembling Li_7Sn_3 appears and persists to the end of

lithiation. Refinements were also performed on Li_2Sb, LiSn (Li:Sn ratio 1:1), Li_5Sn_2 (Li:Sn 2.5:1), Li_7Sn_2 (Li:Sn 3.5:1), $Li_{13}Sn_5$ (Li:Sn 2.6:1), $Li_{17}Sn_4$ (4.25:1), and $Li_{22}Sn_5$ (Li:Sn 4.4:1) to determine whether any other lithiated antimony or lithiated tin phases were formed in *operando*, but no evidence was found for the presence of these phases (see Appendix B). Therefore, we have confirmed that the highest extent of lithiation of Sn is Li_7Sn_3 or Li:Sn ratio of 2.33:1. The formation of an amorphous lithiated Sn phase resembling Li_7Sn_3 in short-range ordering has been suggested with in *operando* solid state NMR on Sn nanoparticles.

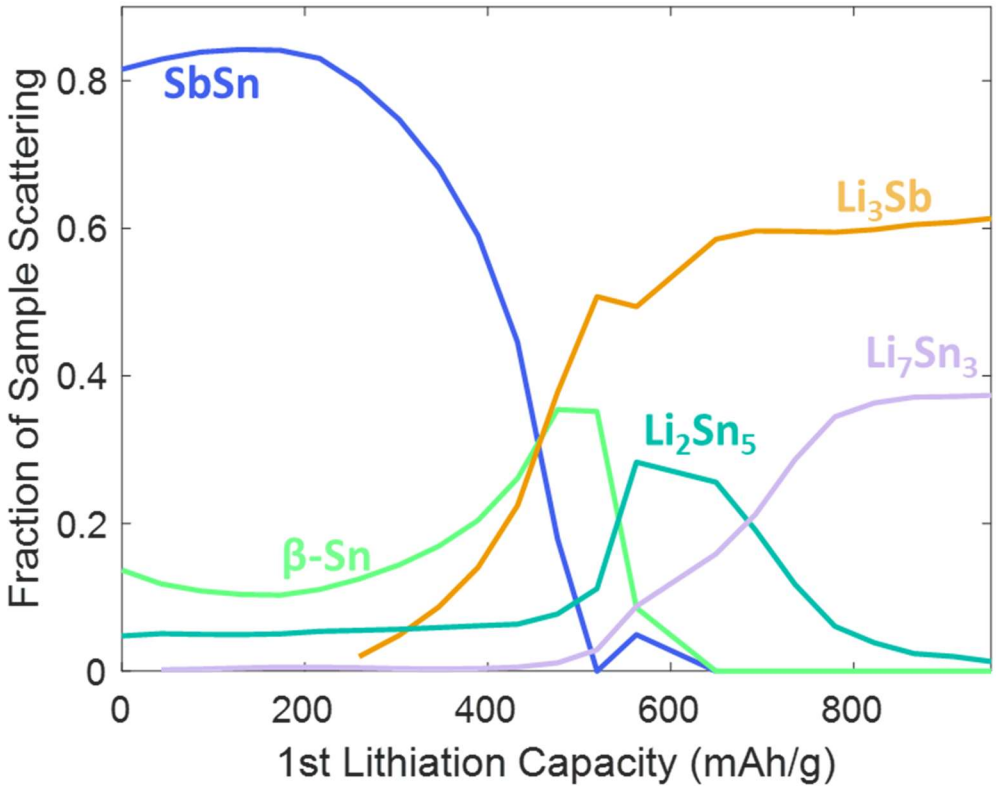

Figure 2.8. Multi-phase refinement of the 1st lithiation *operando* PDF of nanoporous SbSn. Fraction is calculated from the fraction of each phase of total refined scale factors.

Interestingly, in pure Sn electrodes, several more crystalline lithiated tin phases are formed as intermediates during cycling. In contrast, we never observe any crystalline lithiated tin phases

formed during cycling in our SbSn intermetallic. This frustration of the crystallization of lithiated tin phases may be due to the fact that the β-Sn formed after lithiation of Sb is in dispersed nanocrystalline domains embedded in a Li_3Sb matrix. We postulate that the amorphous nature of the lithiated Sn phases provides further stabilization of volume expansion as the amorphous material is more ductile, resulting in more stable electrochemical performance.

Looking at the PDF during delithiation (**Figure 2.9**), it is evident that the evolution of local structure is not merely the reverse of the lithiation scan. As expected, the first delithiation PDF pattern most closely resembles Li_3Sb reference pattern, with some contribution from Li_7Sn_3 peak at 5.58 Å. At the end of delithiation (Figure 5.9b), the correlations in the region from 20 – 30 Å are very weak, confirming that much of the material is amorphous, without long-range order. In the short range from 2 – 15 Å, the delithiation product closely resembles the reference pattern for SbSn. However, it can be noted that there is a sharp peak at 2.98 Å, whose shape looks different from the initial SbSn alloy PDF (Figure 5.6b). Allan *et al.* have observed a very similar amorphous phase in *operando* PDF studies of Na^+ intercalation into pure Sb.[26] They attribute the new sharp peak at 2.9 Å to a Sb-Sb dumbbell-like dimer bonding motif.[26] The peak at 4.44 Å also appears to be two closely overlapping peaks, likely corresponding to SbSn and Sb, suggesting some degree of phase separation of the amorphous material formed at the end of delithiation.

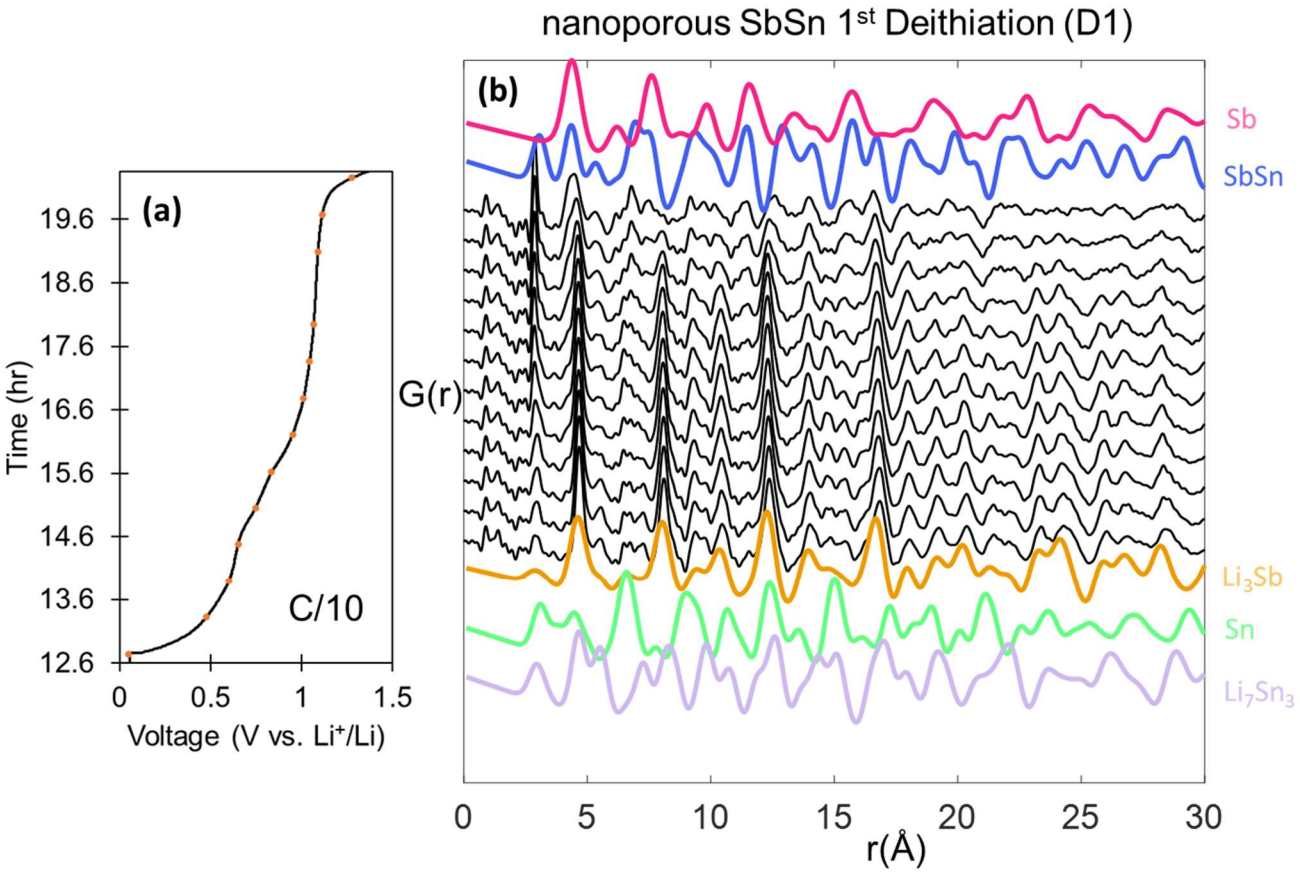

Figure 2.9. *Operando* PDF of nanoporous SbSn cycled with Li^+ at C/10. (a) First delithiation GV curve and (b) normalized operando PDF during first delithiation with simulated reference PDF patterns for Sb, SbSn, Li_3Sb, β-Sn, and Li_7Sn_3. Orange dots indicate voltages where PDF scans were taken.

Again, by performing a multi-phase refinement with Li_3Sb, Li_7Sn_3, Sb, SbSn, and β-Sn (**Figure 2.10**), we can estimate the percentage of each phase throughout the delithiation process. Although Li_2Sn_5 was observed in the operando XRD and lithiation operando PDF, it was not included in the delithiation PDF multi-phase refinment due to the restriction in PDFgui of allowing a maximum of 5 phases. These 5 phases were chosen because they gave the lowest error through the multi-phase refinment. As expected, the material begins primarily as Li_3Sb and Li_7Sn_3, which

decline in intensity as delithiation proceeds. Some β-Sn appears as an intermediate as Li_xSn gets delithiated first. We see the reappearance and growth of SbSn alloy phase to about 45% at the end of delithiation, and the reappearance of Sb. From the *operando* XRD peak area **(Figure 5.5)**, we recall that about 11% of the crystalline nanoporous SbSn is recovered. While the 45% SbSn calcualted from *operando* PDF is a mixture of both crystalline and amoprhous SbSn, the PDF signal due to Sb and β-Sn at the end of delithiation must be amorphous material.

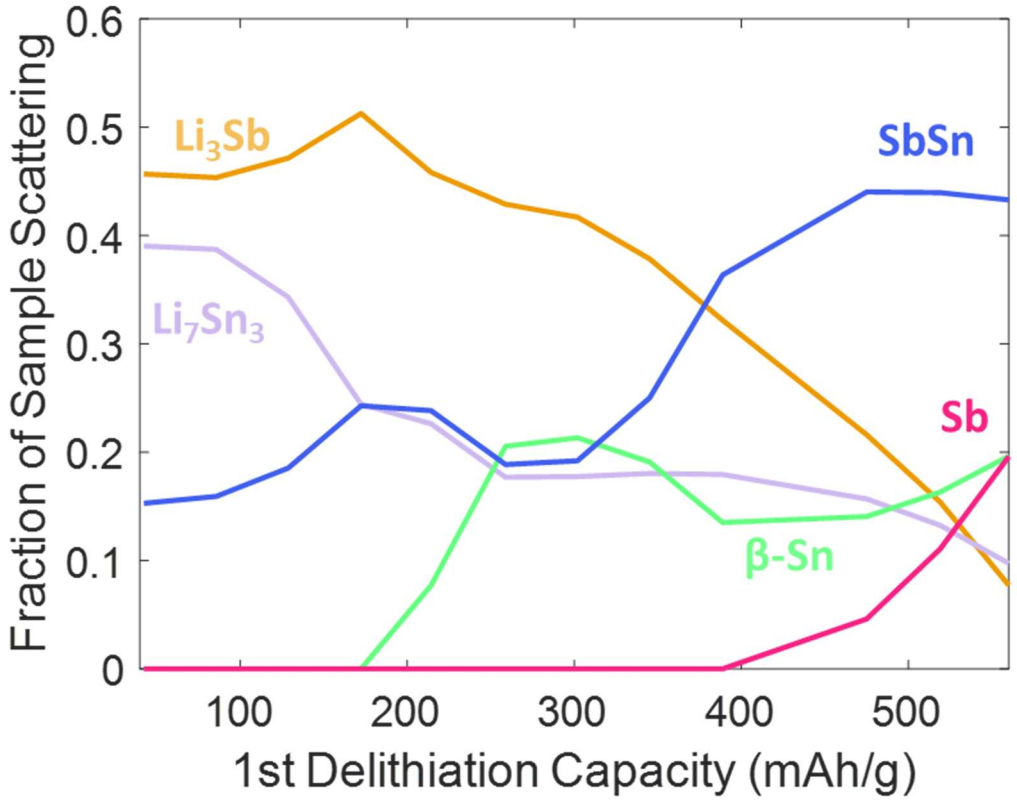

Figure 2.10. Multi-phase refinement of the 1st delithiation during *operando* PDF of nanoporous SbSn. Fraction is calculated from the fraction of each phase of total refined scale factors.

2.5. Conclusions

We have demonstrated the synthesis and characterization of a nanoporous SbSn alloying anode material. The nanoporous architecture promotes volume expansion into the pores, mitigating

crack formation and long-term capacity fade. *Operando* XRD on both nanoporous and bulk SbSn systems clearly shows phase separation, and the formation of Li_3Sb, β-Sn, and Li_2Sn_5 intermediates, and an amorphous lithiated Sn final product. The nanoporous architecture is shown to promote faster lithiation of the Sb and easier phase separation of the alloy. Upon delithiation, bulk SbSn is able to recover 24% of the original crystalline alloy, while nanoporous SbSn recovers only 11% of the original crystalline alloy. Therefore, we employ *operando* PDF as a complementary structural probe to characterize the local structure of the amorphous phase. We discover that lithiation of the Sn goes through Li_2Sn_5 intermediate to reach a final amorphous product that resembles the Li_7Sn_3 phase. The nanoporous intermetallic structure prevents formation of crystalline lithiated Sn phases, buffering the volume expansion and enabling better cycling stability.

2.6. References

[1] Blomgren, G. E. The Development and Future of Lithium Ion Batteries. *Journal of The Electrochemical Society*. **2017**, 164, A5019.

[2] Whittingham, M. Stanley. "Lithium Batteries and Cathode Materials." *Chemical Reviews*, **2004**, 104, 4271 – 4301.

[3] Winter, M.; Brodd, R. "What Are Batteries, Fuel Cells, and Supercapacitors?" *Chemical Reviews*, **2004**, 104, 4245 – 4269.

[4] https://energystorageforum.com/energy-storage-technologies/smart-grid-energy-storage-systems

[5] Dedes, I.-C.; Tsampasis, E.; Elias, C.; Gkonis, P. "Energy Storage in Smart Electrical Grids." 10th Mediterranean Conference on Embedded Computing (MECO), **2021**, p. 1 – 4. doi: 10.1109/MECO52532.2021.9460169.

[6] Goodenough, J.B.; Kim, Y. "Challenges for Rechargeable Li Batteries." *Chemistry of Materials*, **2010**, 22, 587 – 603.

[7] Moyassari, E.; Roth, T.; Kucher, S.; Chang, C.-C.; Hou, S.-C.; Spingler, F.B.; Jossen, A. "The Role of Silicon in Silicon-Graphite Composite Electrodes Regarding Specific Capacity, Cycle Stability, and Expansion." *Journal of The Electrochemical Society*, **2022**, 169, 010504.

[8] An, S.J.; Li, J.; Daniel, C.; Mohanty, D.; Nagpure, S.; Wood, D.L.W. "The state of understanding of the lithium-ion-battery graphite solid electrolyte interphase (SEI) and its relationship to formation cycling." *Carbon*, **2016**, 105, 52 – 76.

[9] Waldmann, T.; Kasper, M.; Wohlfahrt-Mehrens, M. "Optimization of Charging Strategy by Prevention of Lithium Deposition on Anodes in high-energy Lithium-ion Batteries – Electrochemical Experiments." *Electrochimica Acta*, **2015**, 178, 525 – 532.

[10] Obrovac, M.N., et al. Alloy Negative Electrodes for Li-Ion Batteries. *Chem. Rev.* **2014**, 114, 11444 – 11502.

[11] Park, C.-M., et al. Li-alloy based anode materials for Li secondary batteries. *Chem. Soc. Rev*. **2010**, 39, 3115 – 3141.

[12] Xie, H.; Kalisvaart, W.P.; Olsen, B.C.; Luber, E.J.; Mitlin, D.; Buriak, J.M. "Sn-Bi-Sb alloys as anode materials for sodium ion batteries." *Journal of Materials Chemistry A*, **2017**, 5, 9661 – 9670.

[13] Zhao, Y.; Manthiram, A. "High-Capacity, High-Rate Bi-Sb Alloy Anodes for Lithium-Ion and Sodium-Ion Batteries." *Chemistry of Materials*, **2015**, 27, 3096 – 3101.

[14] Augustyn, V., et al. High-rate electrochemical energy storage through Li^+ intercalation pseudocapacitance. *Nature Materials.* **2013**, 12, 518 – 522.

[15] Cook, J.B.; Lin, T.C.; Detsi, E.; Weker, J.N.; Tolbert, S.H. "Using X-ray Microscopy to Understand How Nanoporous Materials Can Be Used to Reduce the Large Volume Change in Alloy Anodes." *Nano Letters*, **2017**, 17, 870 – 877.

[16] Cook, J.B.; Detsi, E.; Liu, Y.; Liang, Y.-L.; Kim, H.-S.; Petrissans, X.; Dunn, B.; Tolbert, S.H. "Nanoporous Tin with a Granular Hierarchical Ligament Morphology as a Highly Stable Li-Ion Battery Anode." *ACS Applied Materials & Interfaces*, **2017**, 9, 293 – 303.

[17] Detsi, E.; Petrissans, X.; Yan, Y.; Cook, J.B.; Deng, Z.; Liang, Y.-L.; Dunn, B.; Tolbert, S.H. "Tuning ligament shape in dealloyed nanoporous tin and the impact of nanoscale morphology on its applications in Na-ion alloy battery anodes." *Physical Review Materials*, **2018**, 2, 055404.

[18] Cook, J.B., et al. Suppression of Electrochemically Driven Phase Transitions in Nanostructure MoS_2 Pseudocapacitors Probed Using Operando X-ray Diffraction. *ACS Nano.* **2019**, 13, 1223 – 1231.

[19] Ruiz, O.; Cochrane, M.; Li, M.; Yan, Y.; Ma, K.; Fu, J.; Wang, Z.; Tolbert, S.H.; Shenoy, V.B.; Detsi, E. "Enhanced Cycling Stability of Macroporous Bulk Antimony-Based Sodium-Ion Battery Anodes Enabled through Active/Inactive Composites." *Advanced Energy Materials*, **2018**, 8, 1801781.

[20] Courtney, I.A.; Dahn, J.R. "Electrochemical and In Situ X-Ray Diffraction Studies of the Reaction of Lithium with Tin Oxide Composites." *Journal of The Electrochemical Society*, **1997**, 144, 2045.

[21] Hwang, S.; Yao, Z.; Zhang, L.; Fu, M.; He, K.; Mai, L.; Wolverton, C.; Su, D. "Multistep Lithiation of Tin Sulfide: An Investigation Using in Situ Electron Microscopy." *ACS Nano*, **2018**, 12, 3638 – 3645.

[22] Xu, H.; Li, S.; Zhang, C.; Chen, X.; Liu, W.; Zheng, Y.; Xie, Y.; Huang, Y.; Li, J. "Roll-to-roll prelithiation of Sn foil anode suppresses gassing and enables stable full-cell cycling of lithium-ion batteries." *Energy & Environmental Science*, **2019**, 12, 2991 – 3000.

[23] Farrow, C.L.; Juhas, P.; Liu, J.W.; Bryndin, D.; Bozin, E.S.; Block. J.; Proffen, Th.; and S.J.L. Billinge. "PDFfit2 and PDFgui: computer programs for studying nanostructure in crystals." *J. Phys.: Condens. Mat.*, **2007**, 19, 335219.

[24] Egami, T. and Billinge, S.J.L. *Underneath the Bragg Peaks: Structural Analysis of Complex Materials*; Pergamon, **2003**.

[25] Jeong, I.-K.; Proffen, T.; Mahiuddin-Jacobs, F.; Billinge, S.J.L. "Measuring Correlated Atomic Motion Using X-ray Diffraction." *Journal of Physical Chemistry A*, **1999**, 103, 921 – 924.

[26] Allan, P.K.; Griffin, J.M.; Darwiche, A.; Borkiewicz, O.J.; Wiaderek, K.M.; Chapman, K.W.; Morris, A.J.; Chupas, P.J.; Monconduit, L.; Grey, C.P. "Tracking Sodium-Antimonide Phase Transformations in Sodium-Ion Anodes: Insights from Operando Pair Distribution Function Analysis and Solid-State NMR Spectroscopy." *JACS*, **2016**, 138, 2352 – 2365.

[27] Wang, X.; Tan, S.; Yang, X.-Q.; Hu, E. "Pair distribution function analysis: Fundamentals and application to battery materials." *Chinese Physics B*, **2020**, 29, 028802.

[28] Chapman, K.W. "Emerging *operando* and x-ray pair distribution function methods for energy materials development." *MRS Bulletin*, **2016**, 41, 231 – 238.

[29] Billinge, Simon J.L. "The rise of the X-ray atomic pair distribution function method: a series of fortunate events." *Phil. Trans. R. Soc. A.*, **2019**, 377:20180413.

[30] Toby, B.H. and R.B. Von Dreele. "GSAS-II: the genesis of a modern open-source all purpose crystallography software package." *Journal of Applied Crystallography*, **2013**, 46, 544 – 549.

[31] Borkiewicz, O.J.; Shyam, B.; Wiaderek, K.M.; Kurtz, C.; Chupas, P.J.; Chapman, K.W. "The AMPIX electrochemical cell: a versatile apparatus for in situ X-ray scattering and spectroscopic measurements." *Journal of Applied Crystallography*, **2012**, 45, 1261 – 1269.

[32] Borkiewicz, O.J.; Wiaderek, K.M.; Chupas, P.J.; Chapman, K.W. "Best Practices for Operando Battery Experiments: Influences of X-ray Experiment Design on Observed Electrochemical Reactivity." *Journal of Physical Chemistry Letters*, **2015**, 6, 2081 – 2085.

[33] Jain, A.; Ong, S.P.; Hautier, G.; Chen, W.; Richards, W.D.; Dacek, S.; Cholia, S.; Gunter, D.; Skinner, D.; Ceder, G.; Persson, K.A. "Commentary: The Materials Project: A materials genome approach to accelerating materials innovation." *APL Materials*, **2013**, 1, 011002.

[34] Momma, K.; Izumi, F. "VESTA 3 for three-dimensional visualization of crystal, volumetric and morphology data." *Journal of Applied Crystallography*, **2011**, 44, 1272 – 1276.

[35] Berger, P.; Flandorfer, H. "Sb-Sn alloy anodes for Li-ion batteries: The ternary system Li-Sb-Sn." *Journal of Alloys and Compounds*, **2021**, 855, 157381.

[36] Frerichs, J.; Ruttert, M.; Bockmann, S.; Winter, M.; Placke, T.; and M. R. Hansen. "Identification of Li_xSn Phase Transitions During Lithiation of Tin Nanoparticle-Based Negative

Electrodes from Ex Situ ^{119}Sn MAS and Operando ^{7}Li NMR and XRD." *ACS Applied Energy Materials*, **2021**, 4, 7278 – 7287.

CHAPTER 3: Understanding Stability in Nanoporous Antimony as Lithium and Sodium Ion Battery Anodes Using *Operando* Diffraction and Microscopy

3.1: Abstract.

Antimony, an alloy anode material, demonstrates the unique property of increased cycle stability when cycled with sodium instead of lithium. Mesoporous antimony was synthesized and cycled against lithium and sodium to determine the synergistic effects of nanoarchitectures and amorphous intermediates in regards to cycle stability. *Operando* 2D transmission X-ray microscopy images confirm the increased reversibility of mesoporous antimony particles when cycled with sodium, by demonstrating the elastic expansion/contraction of active particles with no obvious signs of fracture, contrary to the bulk analog. *Operando* X-ray diffraction provides greater insight into this phenomenon, by demonstrating that antimony evolves entirely through amorphous intermediates when cycled with sodium, instead of the multi-phase coexistence of crystalline phases that are present when cycled with lithium. This amorphous intermediate pathway allows for ductile expansion/contraction, and alleviation of the strain that is expected in active particles where crystalline phase coexistence is present.

3.2: Introduction.

Lithium ion batteries have revolutionized energy storage devices. To further this growth to electric vehicles and grid-scale storage, increased energy densities is vital. Alloy anodes are materials that alloy with the alkali metal leading to very high capacities, charge per gram or cubic centimeter of material. Compared to graphite (372 mAh/g or 756 mAh/cm^3), alloy anodes such as Si (4200 mAh/g or 2190 mAh/cm^3), Sn (993 mAh/g or 1991 mAh/cm^3), Bi (384 mAh/g or 3800 mAh/cm^3), Ge (1600 mAh/g or 2180 mAh/cm^3), and Sb (660 mAh/g or 1889 mAh/cm^3) can offer

more than double the capacity, which has a linear relationship to energy density.[1-4] However, because these materials alloy with so much lithium, they expand and contract, >200% expansion, leading to detrimental cracking of the electrode and material. This fracturing happens within the first few cycles resulting in extreme capacity fade. As a result, stabilizing alloy anodes for repeated cycling has been of interest for decades.

One very powerful tool to stabilize these materials is to nanostructure them. At the nanoscale, grains are more ductile so that repeated expansion and contraction will not fracture the material. The surface to volume ratios of nanoparticles are high so the stress of lithiation dissipates easier across the particle. Secondly, the small volume particles prevent formation of a core shell structure during lithiation and delithiation which can lead to fracture.[5-7] The nanoparticles, in particular, have garnered a lot of interest, and there are many nanoparticle alloy anodes that perform very well.[8-15] One issue is the repeated outward expansion. Even though nanoparticles do not fracture, expansion and contraction can disrupt the slurry made of carbon and polymer binder leading to active material that is no longer electronically connected to the rest of the slurry. To prevent this, increasing the carbon content or synthesizing, or embedding, the material onto the carbon is most common.[8,10,12-14] Other nanoarchitecture designs have been proposed to utilize nanoscale features.

To prevent disruption of the slurry, architectures with void space have proven to be valuable. In this way, the void space is space for expansion to occur into. Hollow structures like hollow nanoparticles and wires have been successfully used to stabilize cycling.[16-19] However, these structures, even though can perform better than dense nanoparticles still have issues with electronic connectivity. Similar to nanoparticles, these hollow particles are often embedded in the carbon additive to maintain conductivity.[18] Hard surface coatings that limit the volume expansion

of the particle have also been successful. These coatings prevent the alloy anode material from disrupting the slurry because they are electronically connected to the slurry and confine the material.[11,20] These coatings undergo a lot of stress confining the anode material and can prevent full lithiation. Alternatively, yolk-shell structures are an impressive nanostructure that can mitigate issues related to a surface coating.[21-23] The yolk is the active anode material that is inside a shell that is connected to the slurry. This is different than a surface coating because there is void space between the yolk and the shell. In this way, expansion can freely occur if the shell is maintained, and the core stays connected to the shell. Even though this strategy is very effective, one limitation is the economic viability of creating such structures. A structure that expands internally would not disrupt the slurry and inexpensive to synthesize would be ideal for alloy anodes.

Selective dealloying is a relatively inexpensive way to create mesoporous networks.[24] The particles can be microns big, but the porosity and pore walls are tens of nanometers. These networks preserve the nanoscale nature of the grains, and the pores can act as space for the small grains to expand into. This process involves an alloy of a sacrificial metal and a more noble metal. When exposed to acid or base, the sacrificial component etches out, and the more noble component re-arranges on the surface creating a mesoporous network. A schematic of this is shown in Figure 3.1a. This method has been used to create alloy anode architectures extensively.[3,25-29] Our group has observed stabilization in Sn and SbSn.[28,30] In the case of lithiation of mesoporous SbSn, we have observed that the pore walls are more structurally sound than in mesoporous Sn. Secondly, in trying to understand the mechanism of lithiation we observed amorphization of the material. We hypothesize that this amorphization is key to stabilizing structure because it allows for easier re-arrangement of atoms and does not involve rigid domain walls between crystallites. Interestingly,

amorphization has been seen in other alloy anode systems like Si and Ge.[1,2,31] Here we aim to study the role of nanoscale architecture and amorphization in alloy anodes.

Sb, in particular, has very interesting behavior when cycled with lithium vs sodium. Sodium ion batteries are an attractive alternative to lithium ion batteries because sodium is more abundant and cheaper than lithium. However, because of its size, the volume expansion and contraction due to incorporation of the alkali is often more severe for sodium than lithium. Consequently, many alloy anode systems that work with lithium are worse with sodium. Sb is an exception, where Sb with sodium performs as well if not better than lithium. Literature suggests that this is the case because Sb cycles through crystalline intermediates when against lithium and amorphous intermediates when against sodium. Commonly referenced mechanisms are seen below in equations 3.1 and 3.2:

$$Sb + 3Li^+ + 3e^- \rightarrow Li_2Sb_{crystalline} + 1Li^+ + 1e^- \rightarrow Li_3Sb_{crystalline} \quad \text{(Equation 3.1)}$$

$$Sb + 3Na^+ + 3e^- \rightarrow Na_xSb_{amorphous} + (3-x)\,Na^+ + (3-x)e^- \rightarrow Na_3Sb_{crystalline} \quad \text{(Equation 3.2)}$$

Here, we synthesize mesoporous Sb using selective dealloying and study how mechanism on the atomic scale affects macroscale features. To accomplish this, we use *operando* transmission X-ray microscopy (TXM) at BL 6-2c at the Stanford Synchrotron Radiation Lightsource (SSRL). This is a powerful technique that allows imaging of large fields of view, ~30 μm, with high resolution, ~30 nm. We observe porosity changes as well as full particle changes. Secondly, this technique can be used on pouch cells, in a real-world environment. However, the electrodes have lower mass loadings, ~25%, compared to normal electrodes.[28,30,32] With this technique, we aim to learn how nanostructure and amorphous intermediates play a role in stabilizing alloy anodes for repeated cycling.

In this work, we synthesized nanoporous Sb (NP-Sb) via selective dealloying as an alloy anode for both lithium and sodium ion batteries. We obtain good capacity retention, 430 mAh/g over 50 cycles with lithium. We, then, use *operando* X-ray diffraction to observe the atomic-scale, crystalline changes of the NP-Sb. We correlate these results with results from *operando* TXM on both the bulk and porous material to identify how these atomic-scale changes affect the mesoscale structure and the overall macroscale particle. These results can help conclude how nanoscale architecture and mechanism synergistically work together to preserve capacity in alloy anodes.

3.3: Results and discussion.

3.3.1. Synthesis and Electrochemistry:

We synthesized NP-Sb using selective dealloying. We started with a Sn and Sb alloy (8:2 Sn:Sb at. ratio). The alloy was etched in heated conc. HBr for 20 minutes. A schematic for selective dealloying is in Figure 3.1a. Figure 3.1b is the corresponding isotherm from N_2 porosimetry with a surface area of 7.964 m^2/g. SEM images in Figure 3.1c and 3.1d confirm porosity along with the TEM image in Figure 3.1e.

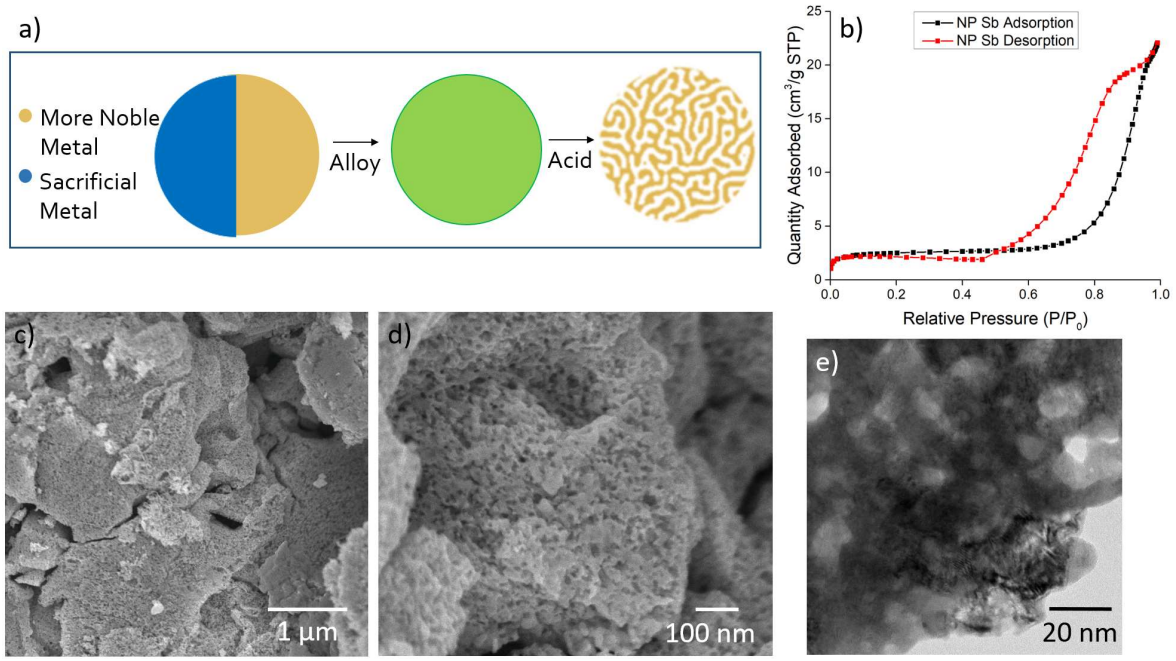

Figure 3.1: a) Cartoon explaining selective dealloying, where a sacrificial component of an alloy is etched out using acid. b) Nitrogen porosimetry isotherm with adsportion and desorption curves shown. c) SEM image of mesoporous antimony synthesized using dealloying with scale bar of 1 micron. d) SEM image of mesoporous antimony synthesized using dealloying with scale bar of 100 nanometers. e) TEM image of mesoporous antimony synthesized using dealloying, where the nonuniform contrast indicated porosity.

This resulting material was cycled in coin cells with a slurry of active material (66% wt), carbon fiber (16% wt), and carboxymethyl cellulose (18% wt). The cyclic voltammograms cycled at 0.1mV/s from 0.05 to 1.5 V are seen in Figure 3.2a and 3.2b for the NP-Sb vs lithium and sodium, respectively. For lithium, there is a reduction peak at 0.85 V consistent with the lithiation potential of Sb with its corresponding oxidation at 1.1 V. Against sodium, there is a reduction peak at 0.5 V consistent with sodiation of Sb and its corresponding oxidation at 0.8 V. The peaks are a

broader for the sodium case suggesting that the sodiation mechanism is less crystalline than the lithiation mechanism which suggests more complex intermediate behavior. Figure 3.2c shows long term cycling of the NP-Sb with lithium and sodium. We see that after an initial drop in capacity both curves stabilize and cycle well with a capacity retention of 430 mAh/g for lithium and 350 mAh/g for sodium after 50 cycles.

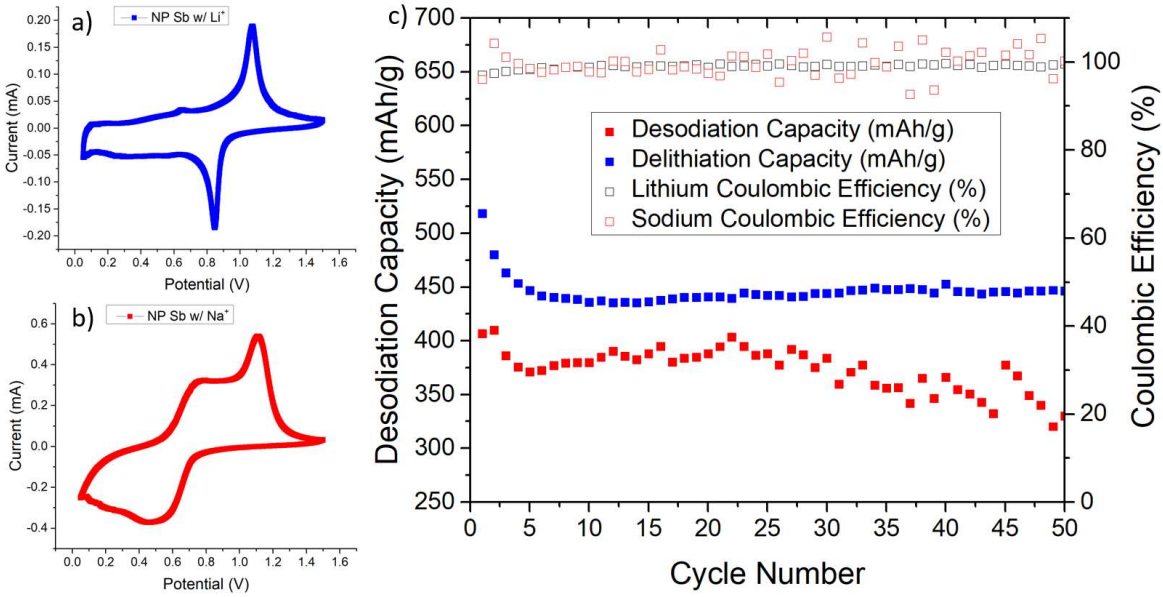

Figure 3.2: Electrochemical data for NP Sb cycled with both sodium and lithium. a) CV for NP Sb cycled with lithium. b) CV for NP Sb cycled with sodium. c) Graph showing capacity retention for NP Sb when cycled with lithium and sodium, and the corresponding coulombic efficiency values.

3.3.2. Operando X-Ray Diffraction:

It is commonly understood that bulk Sb has crystalline intermediates with lithiation and amorphous intermediates with sodiation. However, it has been shown that nanostructured materials can incorporate the alkali differently than bulk. To verify the mechanism, we performed *operando*

X-ray diffraction at SSRL BL 11-3. Figure 3.3 shows the galvanostat along with the diffraction patterns associated with the states of charge. In the beginning, crystalline antimony is present at around 2.02 $Å^{-1}$. Although, the peak is broad suggesting that it is nanoscale and poorly crystalline, this is common for dealloyed materials. As lithiation occurs, the peak corresponding to Sb decreases while peaks grow at around 1.55 $Å^{-1}$ corresponding to Li_2Sb. Similarly, as lithiation continues, peaks of Li_2Sb disappear while peaks for Li_3Sb appear at around 1.67 and 1.92 $Å^{-1}$. One observation of note is that the peaks do not fully disappear before the next peaks appear resulting in two phase co-existence. Upon delithiation, crystalline Sb grows larger than when fully lithiated. However, it is much broader than the start suggesting that it is even less crystalline than when it started. There is also remnant Li_3Sb which implies that not all of the material is fully delithiated.

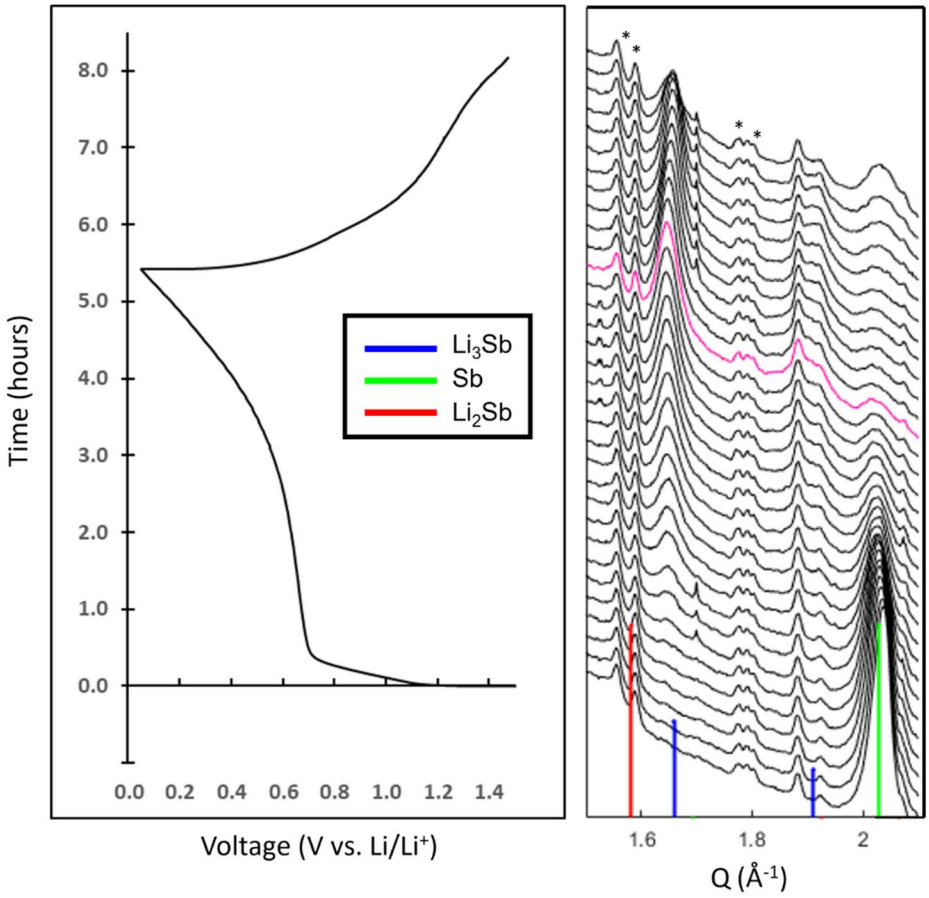

Figure 3.3: Galvanostat on the left with the corresponding diffraction pattern at that state of charge on the right. The key shows various crystal structures that are possibly present. Peaks that are starred are indicative of peaks associated with the pouch cell that are always present.

Figure 3.4 is the galvanostat with corresponding diffraction patterns for the sodiation and desodiation of NP-Sb. As with the lithium case, crystalline Sb peaks at around 2.02 $Å^{-1}$ are at the beginning. These peaks fade with sodiation, and no peaks associated with the active material occur for several scans. Na_3Sb peaks emerge at around 1.32, 1.35, 1.55, 2.38, and 2.01 $Å^{-1}$ with continued sodiation. Unlike with lithium, no new crystalline phases form while another crystalline phase fades with sodium. This corroborates literature suggesting that Sb forms amorphous intermediates during sodiation. Upon desodiation, there are no discernible diffraction peaks. Crystalline Sb does not return, unlike with lithium. Another difference between the two mechanisms seen from diffraction is that we observe that lithiation of NP-Sb goes through a crystalline intermediates and that crystalline phases grow from another crystalline phase. Under sodiation, NP-Sb loses crystallinity before forming crystalline Na_3Sb. There are no crystalline intermediates when sodiated.

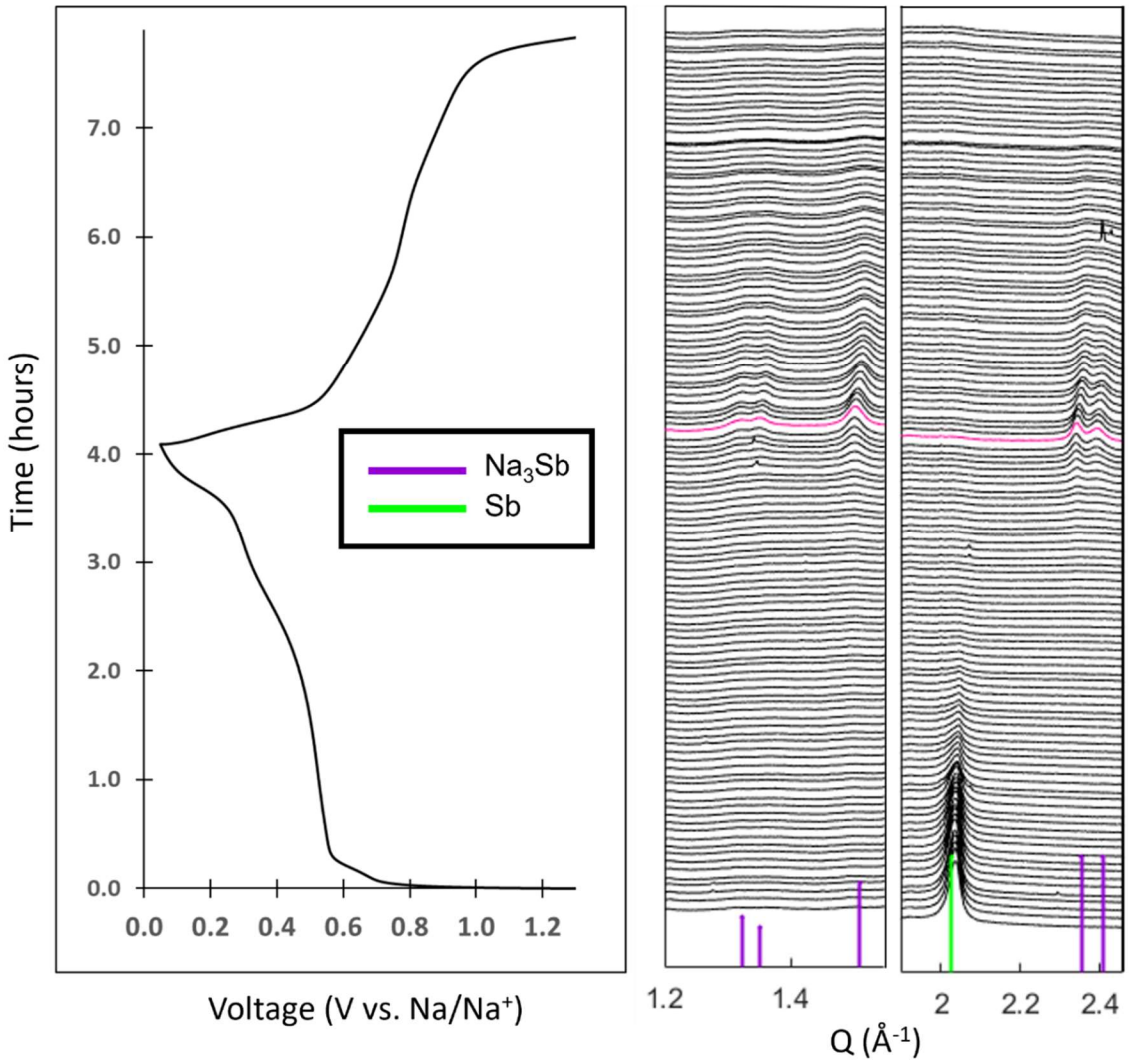

Figure 3.4: Galvanostat on the left with the corresponding diffraction pattern at that state of charge on the right. The key shows various crystal structures expected.

3.3.3. Macroscale Operando TXM:

TXM from beamline 6-2c at SSRL is a powerful tool in understanding how particles change when cycled. Figure 3.5 shows images of bulk particles at different states of charge under sodiation and lithiation. It is important to understand how the bulk behaves in comparison to the nanoporous system to examine how nanostructure affects cycling. Figure 3.5a-c is bulk Sb under

lithiation. We observe areal expansion of 65% and fracturing of the particle in the first cycle. Figure 3.5d has a graph of the areal expansion throughout cycling for both lithiation and sodiation. In both graphs, there is burst of expansion during certain states of charge which is consistent with the alloying reactions at specific voltages. For sodiation, the bulk particle expands more than lithium (120%), seen in Figure 3.5e-g. This is expected because sodium is larger than lithium so incorporating a larger ion would result in increased volume expansion. Interestingly, fewer fractures are observed with sodiation than with lithiation suggesting that the particles accommodate sodium better than lithium even though the volume expansion is greater with sodium. Other bulk particle images are in Figure ESI 3.1.

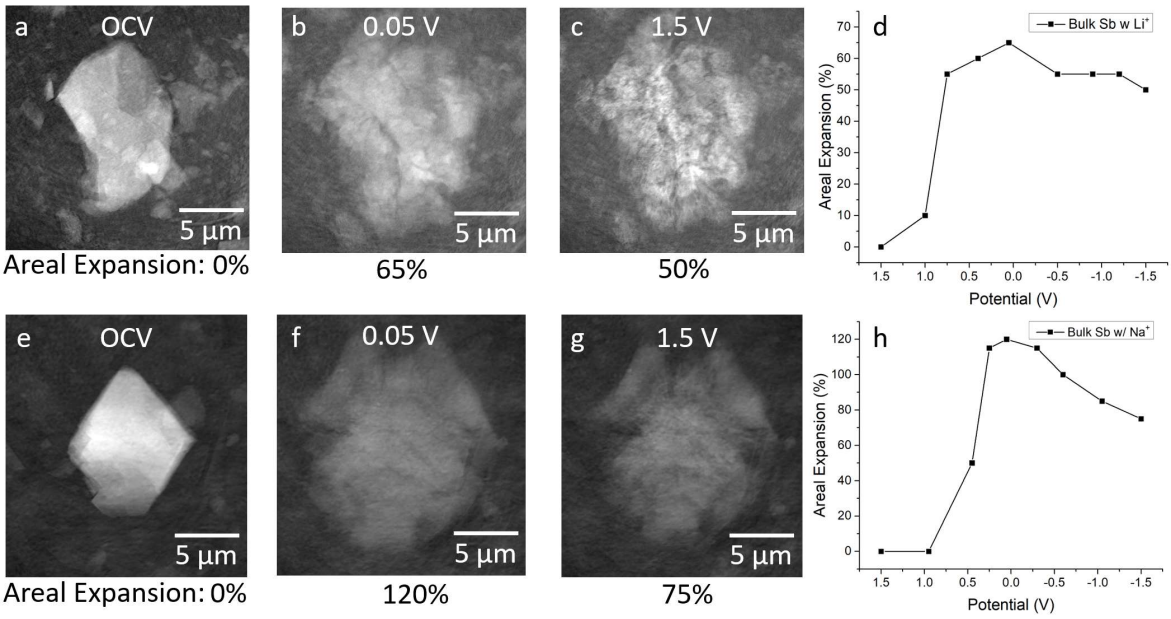

Figure 3.5: a) Bulk Sb particle at OCV. b) Bulk Sb particle at 0.05 V (vs Li/Li^+), or fully lithiated. c) Bulk Sb particle fully delithiated at 1.5 V (vs Li/Li^+). d) Graph of areal expansion versus state of charge where the peak of the expansion is full lithiation. e) Bulk Sb particle at OCV. f) Bulk Sb particle when fully sodiated at 0.05 V (vs. Na/Na^+). g) Bulk Sb particle when fully desodiated at

1.2 V (vs Na/Na^+). h) Graph of the areal expansion versus the state of charge where the peak is full sodiation.

NP-Sb behaves differently than bulk Sb. Figure 3.6 is images of NP-Sb under different states of charge for lithium and sodium. Figure 3.6d graphs the areal expansion of the NP-Sb against the voltage for lithiation. The overall shape of the graph is similar to Figure 3.5d which is expected because the alloying and dealloying reaction is at the same voltage for NP-Sb and bulk Sb. In both cases, the spike in volume expansion occurs around 1.0 V (vs. Li/Li^+) for lithiation and 0.8 V (vs. Na/Na^+) for sodiation. Even though the shape is the same, the nanoporous sample had much less volume expansion than the bulk counterpart: 50% and 100% for lithiation and sodiation, respectively. This shows that nanostructure can mitigate outward volume expansion. The void space created by dealloying allows for inward volume expansion, resulting in less outward expansion. This would result in less disruption of the slurry. A second observation is that during delithiation and desodiation, the nanoporous system shrinks in size whereas the bulk has minimal shrinking. This corroborates that our particles have nanocrystalline domains that expand and shrink similar to nanoparticles. In the case of sodium, the particle almost returns exactly to its original size even though it expands more than lithium. This suggests that the structural changes under sodiation allow for increased reversibility and structural rearrangement.

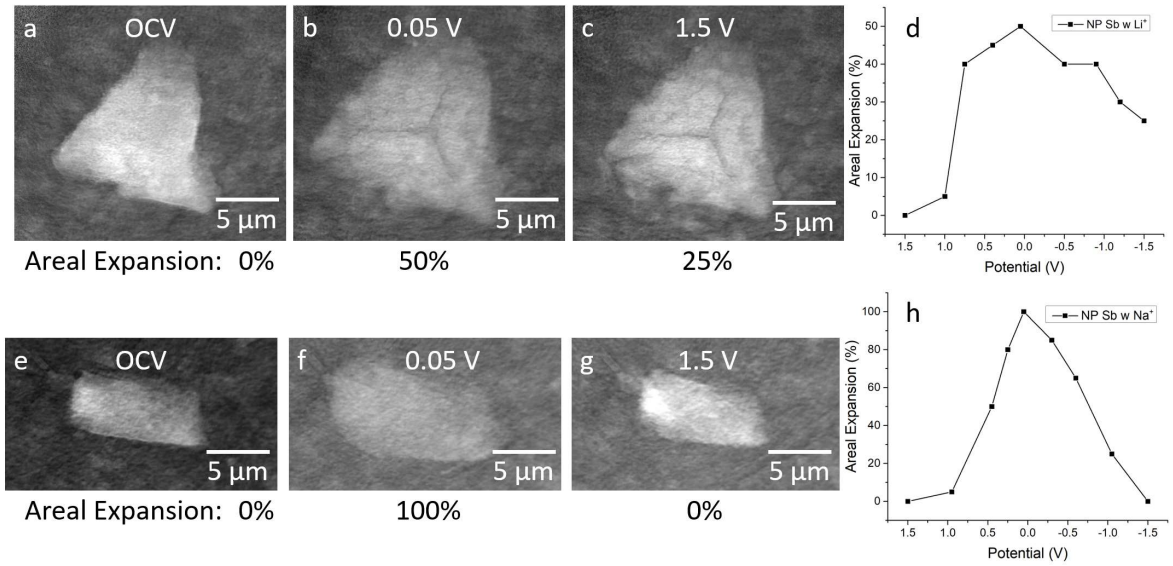

Figure 3.6: a) NP Sb particle at OCV. b) NP Sb particle at 0.05 V (vs Li/Li^+), or fully lithiated. c) NP Sb particle fully delithiated at 1.5 V (vs Li/Li^+). d) Graph of areal expansion versus state of charge where the peak of the expansion is full lithiation. e) NP Sb particle at OCV. f) NP Sb particle when fully sodiated at 0.05 V (vs. Na/Na^+). g) NP Sb particle when fully desodiated at 1.2 V (vs Na/Na^+). h) Graph of the areal expansion versus the state of charge where the peak is full sodiation.

Figure 3.6a-c and 3.6e-g are the images of NP-Sb particles at different states of charge against lithium and sodium, respectively. Figure ESI 3.2 has other particles that exhibit similar behavior. Against sodium in Figure 3.6e-g, the particle expands and returns to a similar size and shape to when it started. This is highly unique even compared against other porous systems. When incorporating lithium in Figure 3.6a-c, there is some contraction, but the particle does not return to its original size or shape. In addition, fracturing and cracking appear in particles that are lithiated. This suggests that the pore walls are under more stress in lithiation than sodiation, even though sodium is larger than lithium. Interestingly, when matched to the diffraction, the fractures

begin to appear around the same time as the crystalline Li_2Sb appears. We believe the stresses by having two phase co-existence and domain walls between crystalline regions force the particle to fracture. This is not the case for sodiation because NP-Sb has non-crystalline intermediates allowing for structural adjustment.

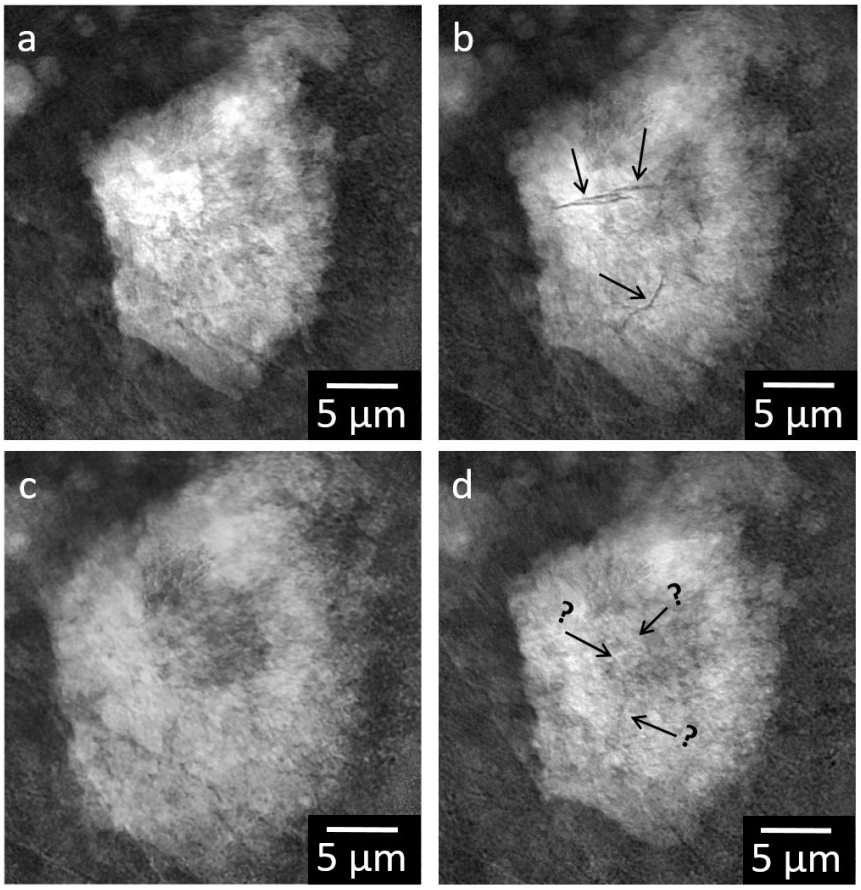

Figure 3.7: a) NP Sb particle at OCV. b) NP Sb particle partially sodiated, showing interior cracking. c) NP Sb particle fully sodiated at 0.05 V (vs Na/Na^+). d) NP Sb particle fully desodiated at 1.5 V (vs Na/Na^+).

For some bigger particles, we observe intriguing behavior. Figure 3.7 is images of a larger NP-Sb particle at different states of charge when sodiated. Similar to Figure 3.6 and 3.5 the particle

expands. However, at a certain state of charge the particle cracks in the middle, seen in Figure 3.7b. It is odd that the particle begins fracturing in the middle because most fractures and stress start at the outer surface of the particle. After continued sodiation, the cracks disappear, seemingly healing in Figure 3.7c. When correlated to the diffraction results show previously, the cracks begin to appear when crystallinity starts decreasing around the 22nd scan from the bottom. The stresses forming from domains walls between crystalline and non-crystalline domains fracture the particle. However, during the region where no crystalline Sb or sodiated Sb appear is where the apparent healing occurs which suggests that amorphization can lead to self-healing behavior. We hypothesize the amorphization allows for increased structural rearrangement. We only observe this behavior in NP-Sb and not bulk Sb. Thus, it is a combination of nanostructure and amorphous intermediates that cause this effect which is more than any one of them alone. When combined, the effect is not additive, but synergistic.

3.4. Conclusions:

In this study, we synthesize mesoporous antimony through selective dealloying of antimony tin with hydrobromic acid. Interestingly, when cycled against sodium and lithium, the porous antimony performs better with sodium. Through X-ray diffraction at SSRL, we observe crystalline intermediates when cycled against lithium. In fact, as one phase shrinks, another one grows, suggesting two phase co-existence. With sodium, there are non-crystalline intermediate phases between the starting and ending crystalline phases. To understand how these crystallinity changes affect structure, we used TXM. With bulk samples, fracturing occurs. However, there is more fracturing with lithium even though the volume expansion is smaller. For porous samples, the particles do not expand as much as the bulk because the void volume can help accommodate particle expansion. In terms of fracturing, lithiation still cracks the particles. When mapped onto

the diffraction, we notice the cracking starts to occur when the first lithiated phase appears, suggesting that shifting from one crystalline phase to another induces stresses to crack the particle. Sodium is much different. For one, when cycled, the particles expand and return to their original size. This is unusual, even for porous systems. Secondly, cracks that appear seemingly heal with further cycling. This healing occurs when no crystalline phases appear in diffraction. We hypothesize that the non-crystalline phases allow for structural rearrangement so that fractures are healed. This is only observed in the nanostructured antimony. Thus, when amorphous intermediates and nanostructure are combined in one system, the effect is synergistic. We obtain new behavior that is not additive to each one individually: the system is highly reversible and self-healing. This is important in designing materials for anodes in rechargeable batteries because it provides design rules and phenomenon to achieve long lasting and high capacity materials. By using these design principles, we help propel rechargeable batteries to industries not yet capable of using these devices.

3.5. References

[1] Wang, J. W.; He, Y.; Fan, F.; Liu, X. H.; Xia, S.; Liu, Y.; Harris, C. T.; Li, H.; Huang, J. Y.; Mao, S. X.; Zhu, T. Two-Phase Electrochemical Lithiation in Amorphous Silicon. *Nano Letters* **2013**, *13* (2), 709–715. https://doi.org/10.1021/nl304379k.

[2] Liu, X.; Wu, X. Y.; Chang, B.; Wang, K. X. Recent Progress on Germanium-Based Anodes for Lithium Ion Batteries: Efficient Lithiation Strategies and Mechanisms. *Energy Storage Materials*. Elsevier B.V. September 1, **2020**, pp 146–169. https://doi.org/10.1016/j.ensm.2020.05.010.

[3] Cook, J. B.; Detsi, E.; Liu, Y.; Liang, Y. L.; Kim, H. S.; Petrissans, X.; Dunn, B.; Tolbert, S. H. Nanoporous Tin with a Granular Hierarchical Ligament Morphology as a Highly Stable Li-Ion Battery Anode. *ACS Appl Mater Interfaces* **2017**, *9* (1), 293–303. https://doi.org/10.1021/acsami.6b09014.

[4] Lv, H.; Qiu, S.; Lu, G.; Fu, Y.; Li, X.; Hu, C.; Liu, J. Nanostructured Antimony/Carbon Composite Fibers as Anode Material for Lithium-Ion Battery. *Electrochimica Acta* **2015**, *151*, 214–221. https://doi.org/10.1016/j.electacta.2014.11.013.

[5] Lee, K. T.; Cho, J. Roles of Nanosize in Lithium Reactive Nanomaterials for Lithium Ion Batteries. *Nano Today*. February 2011, pp 28–41. https://doi.org/10.1016/j.nantod.2010.11.002.

[6] Im, H. S.; Cho, Y. J.; Lim, Y. R.; Jung, C. S.; Jang, D. M.; Park, J.; Shojaei, F.; Kang, H. S. Phase Evolution of Tin Nanocrystals in Lithium Ion Batteries. *ACS Nano* **2013**, *7* (12), 11103–11111. https://doi.org/10.1021/nn404837d.

[7] Xu, L.; Kim, C.; Shukla, A. K.; Dong, A.; Mattox, T. M.; Milliron, D. J.; Cabana, J. Monodisperse Sn Nanocrystals as a Platform for the Study of Mechanical Damage during Electrochemical Reactions with Li. *Nano Letters* **2013**, *13* (4), 1800–1805. https://doi.org/10.1021/nl400418c.

[8] Xiong, P.; Wu, J.; Zhou, M.; Xu, Y. Bismuth-Antimony Alloy Nanoparticle@Porous Carbon Nanosheet Composite Anode for High-Performance Potassium-Ion Batteries. *ACS Nano* **2020**, *14* (1), 1018–1026. https://doi.org/10.1021/acsnano.9b08526.

[9] Bryngelsson, H.; Eskhult, J.; Nyholm, L.; Herranen, M.; Alm, O.; Edström, K. Electrodeposited Sb and Sb/Sb2O3 Nanoparticle Coatings as Anode Materials for Li-Ion Batteries. *Chemistry of Materials* **2007**, *19* (5), 1170–1180. https://doi.org/10.1021/cm0624769.

[10] Nguyen, A. G.; Le, H. T. T.; Verma, R.; Vu, D. L.; Park, C. J. Boosting Sodium-Ion Battery Performance Using an Antimony Nanoparticle Self-Embedded in a 3D Nitrogen-Doped Carbon Framework Anode. *Chemical Engineering Journal* **2022**, *429*. https://doi.org/10.1016/j.cej.2021.132359.

[11] Fang, G.; Deng, X.; Zou, J.; Zeng, X. Amorphous/Ordered Dual Carbon Coated Silicon Nanoparticles as Anode to Enhance Cycle Performance in Lithium Ion Batteries. *Electrochimica Acta* **2019**, *295*, 498–506. https://doi.org/10.1016/j.electacta.2018.10.186.

[12] Luo, W.; Zhang, P.; Wang, X.; Li, Q.; Dong, Y.; Hua, J.; Zhou, L.; Mai, L. Antimony Nanoparticles Anchored in Three-Dimensional Carbon Network as Promising Sodium-Ion Battery Anode. *Journal of Power Sources* **2016**, *304*, 340–345. https://doi.org/10.1016/j.jpowsour.2015.11.047.

[13] Yuan, Z.; Dong, L.; Gao, Q.; Huang, Z.; Wang, L.; Wang, G.; Yu, X. SnSb Alloy Nanoparticles Embedded in N-Doped Porous Carbon Nanofibers as a High-Capacity Anode Material for Lithium-Ion Batteries. *Journal of Alloys and Compounds* **2019**, *777*, 775–783. https://doi.org/10.1016/j.jallcom.2018.10.295.

[14] Pan, Q.; Wu, Y.; Zheng, F.; Ou, X.; Yang, C.; Xiong, X.; Liu, M. Facile Synthesis of M-Sb (M = Ni, Sn) Alloy Nanoparticles Embedded in N-Doped Carbon Nanosheets as High Performance Anode Materials for Lithium Ion Batteries. *Chemical Engineering Journal* **2018**, *348*, 653–660. https://doi.org/10.1016/j.cej.2018.05.043.

[15] Zhang, W.; Miao, W.; Liu, X.; Li, L.; Yu, Z.; Zhang, Q. High-Rate and Ultralong-Stable Potassium-Ion Batteries Based on Antimony-Nanoparticles Encapsulated in Nitrogen and Phosphorus Co-Doped Mesoporous Carbon Nanofibers as an Anode Material. *Journal of Alloys and Compounds* **2018**, *769*, 141–148. https://doi.org/10.1016/j.jallcom.2018.07.369.

[16] Cheng, Y.; Huang, J.; Li, R.; Xu, Z.; Cao, L.; Ouyang, H.; Li, J.; Qi, H.; Wang, C. Enhanced Cycling Performances of Hollow Sn Compared to Solid Sn in Na-Ion Battery. *Electrochimica Acta* **2015**, *180*, 227–233. https://doi.org/10.1016/j.electacta.2015.08.125.

[17] Liu, J.; Yang, Z.; Wang, J.; Gu, L.; Maier, J.; Yu, Y. Three-Dimensionally Interconnected Nickel-Antimony Intermetallic Hollow Nanospheres as Anode Material for High-Rate Sodium-Ion Batteries. *Nano Energy* **2015**, *16*, 389–398. https://doi.org/10.1016/j.nanoen.2015.07.020.

[18] Lin, Z.; Wang, G.; Xiong, X.; Zheng, J.; Ou, X.; Yang, C. Ni-Polymer Gels-Derived Hollow NiSb Alloy Confined in 3D Interconnected Carbon as Superior Sodium-Ion Battery Anode. *Electrochimica Acta* **2018**, *269*, 225–231. https://doi.org/10.1016/j.electacta.2018.03.010.

[19] Boebinger, M. G.; Yarema, O.; Yarema, M.; Unocic, K. A.; Unocic, R. R.; Wood, V.; McDowell, M. T. Spontaneous and Reversible Hollowing of Alloy Anode Nanocrystals for Stable Battery Cycling. *Nature Nanotechnology* **2020**, *15* (6), 475–481. https://doi.org/10.1038/s41565-020-0690-9.

[20] Zhou, D.; Song, W. L.; Fan, L. Z. Hollow Core-Shell SnO2/C Fibers as Highly Stable Anodes for Lithium-Ion Batteries. *ACS Applied Materials and Interfaces* **2015**, *7* (38), 21472–21478. https://doi.org/10.1021/acsami.5b06512.

[21] Hong, W.; Ge, P.; Jiang, Y.; Yang, L.; Tian, Y.; Zou, G.; Cao, X.; Hou, H.; Ji, X. Yolk-Shell-Structured Bismuth@N-Doped Carbon Anode for Lithium-Ion Battery with High Volumetric Capacity. *ACS Applied Materials and Interfaces* **2019**, *11* (11), 10829–10840. https://doi.org/10.1021/acsami.8b20477.

[22] Li, S.; Niu, J.; Zhao, Y. C.; So, K. P.; Wang, C.; Wang, C. A.; Li, J. High-Rate Aluminium Yolk-Shell Nanoparticle Anode for Li-Ion Battery with Long Cycle Life and Ultrahigh Capacity. *Nature Communications* **2015**, *6*. https://doi.org/10.1038/ncomms8872.

[23] Liu, N.; Lu, Z.; Zhao, J.; Mcdowell, M. T.; Lee, H. W.; Zhao, W.; Cui, Y. A Pomegranate-Inspired Nanoscale Design for Large-Volume-Change Lithium Battery Anodes. *Nature Nanotechnology* **2014**, *9* (3), 187–192. https://doi.org/10.1038/nnano.2014.6.

[24] McCue, I.; Benn, E.; Gaskey, B.; Erlebacher, J. Dealloying and Dealloyed Materials. *Annual Review of Materials Research* **2016**, *46* (1), 263–286. https://doi.org/10.1146/annurev-matsci-070115-031739.

[25] Kunduraci, M. Dealloying Technique in the Synthesis of Lithium-Ion Battery Anode Materials. *Journal of Solid State Electrochemistry*. Springer New York LLC August 1, 2016, pp 2105–2111. https://doi.org/10.1007/s10008-016-3226-3.

[26] Wang, Z.; Fei, P.; Xiong, H.; Qin, C.; Zhao, W.; Liu, X. CoFe2O4 Nanoplates Synthesized by Dealloying Method as High Performance Li-Ion Battery Anodes. *Electrochimica Acta* **2017**, *252*, 295–305. https://doi.org/10.1016/j.electacta.2017.08.189.

[27] Zhang, H.; An, W.; Song, H.; Xiang, B.; Mei, S.; Hu, Y.; Gao, B. Synthesis of Micro-Sized Porous Antimony via Vapor Dealloying for High-Performance Na-Ion Battery Anode. *Solid State Ionics* **2020**, *352*. https://doi.org/10.1016/j.ssi.2020.115365.

[28] Cook, J. B.; Lin, T. C.; Detsi, E.; Weker, J. N.; Tolbert, S. H. Using X-Ray Microscopy to Understand How Nanoporous Materials Can Be Used to Reduce the Large Volume Change in Alloy Anodes. *Nano Letters* **2017**, *17* (2), 870–877. https://doi.org/10.1021/acs.nanolett.6b04181.

[29] Li, M.; Qiu, T.; Foucher, A. C.; Fu, J.; Wang, Z.; Zhang, D.; Rappe, A. M.; Stach, E. A.; Detsi, E. Impact of Hierarchical Nanoporous Architectures on Sodium Storage in Antimony-Based Sodium-Ion Battery Anodes. *ACS Applied Energy Materials* **2020**, *3* (11), 11231–11241. https://doi.org/10.1021/acsaem.0c02161.

[30] Lin, T. C.; Dawson, A.; King, S. C.; Yan, Y.; Ashby, D. S.; Mazzetti, J. A.; Dunn, B. S.; Weker, J. N.; Tolbert, S. H. Understanding Stabilization in Nanoporous Intermetallic Alloy Anodes for Li-Ion Batteries Using Operando Transmission x-Ray Microscopy. *ACS Nano* **2020**, *14* (11), 14820–14830. https://doi.org/10.1021/acsnano.0c03756.

[31] Chou, C. Y.; Hwang, G. S. On the Origin of the Significant Difference in Lithiation Behavior between Silicon and Germanium. *Journal of Power Sources* **2014**, *263*, 252–258. https://doi.org/10.1016/j.jpowsour.2014.04.011.

[32] Cook, J. B.; Lin, T. C.; Detsi, E.; Weker, J. N.; Tolbert, S. H. Using X-Ray Microscopy to Understand How Nanoporous Materials Can Be Used to Reduce the Large Volume Change in Alloy Anodes. *Nano Letters* **2017**, *17* (2), 870–877. https://doi.org/10.1021/acs.nanolett.6b04181.

Chapter 4: A Simple Capillary-Based Electrochemical Cell for 3D X-ray Nanotomography

4.1: Abstract.

Acquisition of *operando* tomographic datasets is difficult due to the inherent incompatibility of traditional battery cell geometries with the data gathering technique itself. By designing a new battery cell geometry specifically optimized to perform electrochemically, while presenting a largely unchanging environment for X-rays to pass through during cell rotation, the difficulty in gathering these *operando* tomographic datasets is largely mitigated. This cell has been shown to electrochemically perform similarly to an ideal cell environment, and the *operando* data gathered using this cell has been used to successfully perform tomographic reconstructions and analysis. This cell design offers a simple, low cost alternative to other complicated, highly specialized tomography cell designs, and its simple adaptability makes it applicable to a myriad of different battery materials. This report aims to share this simple design, so that these *operando* tomographic datasets can be gathered by any research group that has access to these common cell components.

4.2: Introduction.

Energy storage devices are becoming increasingly relevant, as the global economy undergoes a shift from traditional fossil fuel sources to renewable energy sources. Rechargeable battery systems are at the forefront of this transition, with lithium-ion batteries making up the bulk of energy storage, not just for portable electronics, but also for the burgeoning electric vehicle field.[1-3] Lithium-ion batteries, and similar analogs such as sodium-ion and potassium-ion batteries, operate by shuttling ions from a graphite anode to a transition metal oxide cathode during discharge, and back again during charging processes.[4-6] While this intercalation type of cell is

widely used in commercial applications, research continues on other promising systems, including lithium-sulfur conversion chemistry, and silicon anode alloying chemistry cells.[7] While these systems and their derivatives offer significant improvements in energy density over a commercial lithium-ion battery, they are hindered by irreversible chemical changes and destructive volume change issues, respectively.[8-10]

Despite the robust depth of electrochemical cell designs, many of these materials typically employ a nanostructured architecture, which undergo distinctly different structural evolution during electrochemical events, compared to their bulk counterparts.[11] When anode materials are electrochemically cycled, the accommodation of varying amounts of lithium-ions result in large expansion of particle grains. The expansion of grains within a particle results in accumulation of extensive strain throughout the particle, which typically manifests destructively as grain fracture and particle pulverization. Porous nanostructures have been shown to alleviate some of this strain, by providing channels for electrolyte infiltration, shortening lithium-ion diffusion pathways, and mechanically buffering volume expansion. These cohesive properties inherently increases single particle stability, which holistically contributes towards the overall performance and lifetime of the battery cell.[12] Alloy anode materials in particular, have shown significantly improved electrochemical stability when these nanostructured architectures are applied.

Substantial research has been conducted to understand the failure mechanism of active battery materials during damaging volume expansion and contraction events. Most notably transmission X-ray microscopy (TXM) imaging has been utilized extensively in understanding the behavior of these particles during cycling.[13,14] TXM has proven its capabilities for operando battery studies, as fast imaging reduces active material radiation exposure, and the 2D images yield high resolution of ~30 nm. Traditionally, single 2D TXM images, produce a field of view of ~30

μm, but it is common practice to stitch together single images to yield a larger field of view, without losing resolution. *In-situ* 2D TXM imaging provides a detailed view of active particle evolution, including areal expansion and global particle pulverization, but fails to provide insight into the evolution of porous architectures and interior crack formation. *In-situ* 2D TXM images are common in analyzing new battery materials, as significant information can be gleaned about particle stability, ranging from observing expansion reversibility and crack propagation.[15] However, since these 2D images are taken by transmission imaging, all porous networks within a single particle are overlaid and are indistinguishable from one another, limiting the interior particle information that can be obtained.

Tomographic data sets overcome some of the limitations of 2D TXM images, and can provide a detailed view of nanoarchitecture evolution, including the filling of porous networks and the origin of interior cracking.[16-18] Utilizing a series of 2D images, of a single particle, taken across a range of different angles, the images can be computationally reconstructed into a detailed 3D model.[19] These tomographic reconstructions allow for an interior view of particle evolution, particularly well-suited for nanostructured materials like alloy anodes, providing unprecedented insight into the mechanisms by which these architectures buffer volume expansion and stabilize active particles.[20-22] Furthermore, synchrotron radiation monochromators provide the adaptability to pinpoint or scan X-ray imaging energies. This ability allows for wide varieties of battery materials to be imaged, or to scan absorption edges of multicomponent systems. In the case of multicomponent systems, elemental mapping by imaging above and below absorption edges of individual elements in a process known as X-ray absorption near edge spectroscopy (XANES), provide 2D image contrast corresponding to the presence of targeted element.[23,24] For example, in multicomponent alloy anodes, different elements lithiate at different potentials resulting in

formation of bulk domains, a phenomenon that can, conceivably, be tracked in real time within a particle by utilizing *operando* tomography and XANES. Thus, combining 3D tomography with XANES allows for the observation of the particles interior phase segregation during lithiation of multicomponent alloy systems.[25]

While battery research involving tomographic reconstruction has typically been performed *ex-situ,* largely due to the incompatibility of the technique with traditional cell geometries, increasing efforts are being made to enable easy access to *in-situ* tomographic analysis.[26-28] Previous *ex-situ* tomography research demonstrates the versatility of the technique, as the literature reports studies on cathode materials, anode materials, intercalation materials, conversion type materials, alloying type materials, and even sodium/potassium-ion batteries.[29-33] *In-situ* tomographic studies have emerged as a powerful analytical technique in the energy storage field, and has been able to provide new insight into the initial irreversibility of metal sulfides, and the improved cycling stability of heterogeneous alloy anodes versus their homogenous analogs.[34,35] The major consideration for gathering a 3D tomography data set is the incompatibility of traditional battery cell geometries with the tomographic imaging technique itself, driving the necessity for a novel 3D battery cell geometry.

During the acquisition of a tomographic data set *in-situ*, the cell must be rotated across 180° while 2D images are taken, which necessitates a cell geometry that appears largely unchanging to the beam path, at all angles. Rotation of traditional 2D battery cell geometries, such as pouch and coin cells, result in a changing path length, subsequently increasing the quantities of attenuating materials and active particles. The resulting change in transmission, and the large amount of active particles entering the field of view at higher angles, creates poor quality 3D reconstructions that do not accurately represent the particle being imaged. A 3D cell geometry

mitigates these problems, and presents a homogenous environment for beam transmission at all angles. The ideal 3D cell should offer an identical path length for beam transmission during rotation, minimize beam exposure to highly attenuating materials, and attempt to reduce number of active particles entering and exiting field of view during tomography acquisition.

The novel 3D tomography cell design described in this paper successfully overcomes the limitations of traditional 2D cells, and attempts to improve upon other previously established 3D cell geometries by reducing the requirement for specialized equipment and experimental cell preparation. Other 3D cells have previously been proposed, including a modified coin cell geometry, a modified PFA Swagelok type cell, and a PEEK cell.[36] Unfortunately, these cells all come with drawbacks, reconstruction artifacts due to truncated angles, large cell diameters reducing resolution, and requirement of custom built cell components, respectively. By reducing the complexity of the cell design, while maintaining a 3D cell geometry free of highly attenuating materials, our cell has overcome many of these limitations. This new cell design, represented in Figure 1a and shown practically in Figure 1b, utilizes a quartz X-ray powder capillary and a graphite working electrode to minimize beam attenuation. A pointed electrode tip to reduces the quantity of additional active materials in the field of view during imaging, and the flooded cell design eliminates dependence on high stack pressure for electrochemical performance. This cell requires only common components like graphite and copper wire, and this low-tech composition makes the design ideal for any research group considering *in-situ* tomography studies of battery materials.

As a representative study to demonstrate the efficacy of this novel cell design, porous alloy anode materials were chosen for *in-situ* analysis. Alloy anode materials, which are typically metallic or metalloid elements like Si, Ge, Sn, or Sb, have potential to replace commercial

intercalation graphite anodes due to their immense gravimetric and volumetric capacities.[37] These materials alloy with Li^+ ions, accommodating multiple Li^+ per host atom, and possess the ability to perform multielectron redox, which affords these materials notably greater energy density than traditional intercalation anodes.[38] While graphite offers a theoretical capacity of 372 mAh/g, represenftative alloy anode materials Si, Ge, Sn, and Sb offer 3579 mAh/g, 1384 mAh/g. 990 mAh/g, and 660mAh/g, respectively.[39,40] However, these high capacity materials, due to their alloying charge storage mechanism, undergo large volume expansion events that can reduce their cycle life (280% for Si, 270% for Ge, 260% for Sn, and 147% for Sb).[41] This repeated expansion and contraction during electrochemical cycling results in particle pulverization and delamination from the current collector, causing significant capacity fade.[42] This system is ideal for this demonstrative tomographic study, as not only will volume expansion be observed in particles, but the interior pore system should evolve significantly as the particle expands into the pores. This model system will provide an opportunity to not only track particle volume expansion *in-situ*, but also will allow for an evaluation of the limits of resolution this technique provides, as changes in porous architectures will be on a much smaller length scale than global particle expansion.

4.3: Materials/Theory Used.

The novel capillary cell described in this paper consists primarily of two rod-like electrodes and a quartz X-ray capillary casing. The X-ray capillary (10-SQZ, Charles Supper Company) is cut to the specifications detailed in Figure 1c, as are the rest of the components described here. Graphite electrodes are cut from common pencil lead (0.9 mm 2H, Pentel), and the copper current collector is cut and mechanically straightened from copper wire (20 Gauge Pure Copper Wire, Craft). 1 M $LiPF_6$ commercial electrolyte (MFCD00011096, Sigma-Aldrich) with 10% FEC additive (MFCD06247543, Sigma-Aldrich) is used to provide an ionically conductive connection

between electrodes. Paraffin wax (MFCD00132833, Sigma-Aldrich) is used to form an inert seal to contain electrolyte within the cell, while an epoxy (Instant Setting Epoxy Adhesive, HPT) is used to provide mechanical stability between cell electrodes and capillary casing. Electrolyte is injected into cell using a disposable syringe and a 0.7 mm diameter (22 gauge) needle.

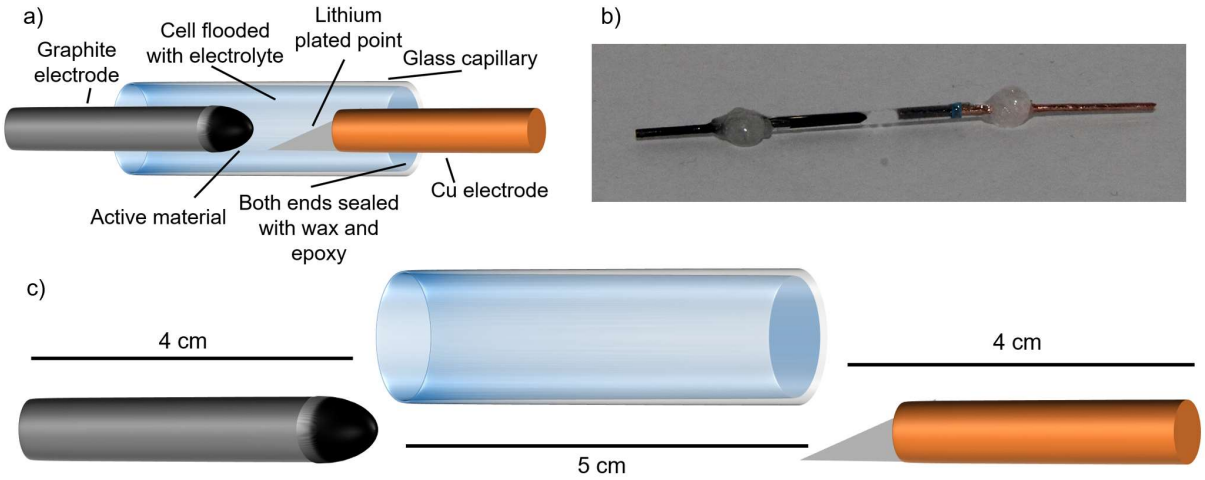

Figure 4.1: a) Cartoon representation of 3d cell design. b) Graphite electrode paired with copper current collector in a functional cell. c) Representation of cell showing component dimensions as assembled.

4.4: Procedure.

The cell assembly procedure can be done partially in atmosphere, and partially in an inert glovebox environment. A majority of the initial preparation can be completed outside the glovebox for ease of work, before being pumped into an inert atmosphere glovebox for final cell assembly. First, a 4 cm piece of graphite is cut for use as a working electrode. The tip of this graphite rod is delicately sharpened into a point using a grinding wheel. The purpose of this sharpened point is to isolate active particles at the tip for unobstructed tomography imaging, since graphite is largely transparent to X-ray energies used for TXM, while the sloping sides of the point

encompass sufficient active material to provide a measurable electrochemical signal during battery cycling. A typical battery slurry is prepared with mass ratios of 50% active material, 25% polyvinylidene fluoride binder (PVDF) dissolved in N-methylpyrrolidone (NMP), and 25% carbon nanofibers to provide a conductive matrix. The sharpened graphite rods are suspended horizontally using toothless alligator clips, and the slurry is drop-cast onto the sharpened graphite tip using a disposable glass pipet. Any excess solution is vertically wicked away with Kimwipes (Kemtech) by touching the slurry droplet perpendicular to the wipe. The electrodes, still suspended horizontally, are subsequently dried in a vacuum oven at 80 °C for a minimum of 8 hours. After the slurry has dried, these electrodes are used immediately in the next step of cell assembly.

A 5 cm length of X-ray capillary tube is cut carefully using a diamond scribe, in order to serve as the outer casing of the battery cell. One of the sharpened graphite electrodes with active slurry is then inserted about 2 cm into one end of the glass capillary. The junction between the graphite electrode and edge of capillary is sealed with melted paraffin wax, where it solidifies into a small bead, preventing further movement of the electrode and providing an inert seal for the electrolyte to be injected later. Once the wax has cooled, a two-component epoxy is mixed and then immediately spread over the wax bead to provide additional mechanical stability to the graphite electrode-capillary assembly, described henceforth as a "half-capillary cell." The epoxy must be applied carefully in order to make sure there is good contact to both the bare graphite electrode surface and the surface of the capillary without occluding the graphite tip inside the capillary, and must completely encapsulate the wax bead. This half-capillary cell is allowed to dry overnight to promote easier handling during further assembly, and is then pumped into the inert atmosphere glovebox.

The final component requiring preparation is the copper current collector. A 4 cm piece of copper wire is cut, and then the cut edges are flattened using a grinding wheel, reducing any mushrooming of the tip that can result in a local increase of wire diameter. One end of this copper wire is sharpened into an asymmetrical right angle point using a grinding wheel, and it is this end that will be electroplated with lithium. This sharpened point, lying against the wall of the capillary, provides a gap for any bubbles formed from electrolyte degradation, so that these bubbles can pass by the lithium tip without breaking electrolyte continuity between electrodes in the cell. To ensure a clean surface for lithium electroplating, the current collector is washed with ethanol, acetone, and isopropyl alcohol in order, etched in 1 M H_2SO_4 for 1 minute, then washed a final time in anhydrous acetone. After this washing procedure is completed, the current collector is pumped immediately into the glovebox. Inside the glovebox inert atmosphere, a simple 3-neck flooded cell is assembled for lithium electroplating. The cell is set up as follows, 1 M $LiPF_6$ electrolyte, metallic lithium as the current collector and reference electrode, and a piece of cleaned copper wire is submerged 1 cm deep in the electrolyte to operate as the working electrode. Utilizing a potentiostat, a constant current of -1 mA is applied for 30 minutes, which compels lithium ions to electroplate on the copper current collector surface. After electroplating, the copper current collectors are subsequently annealed for 45 minutes on a hotplate at 140 °C, using a thin sheet of stainless steel to prevent any contamination of hotplate surface.

With all individual components prepared, the full capillary cell can now be assembled. For full cell assembly, the following cell components must be present in the glovebox inert environment: half-capillary cell, copper current collector with lithium electroplated tip, 1 M $LiPF_6$ with 10% FEC additive, paraffin wax, and 2 component epoxy. First, electrolyte must be injected into the half-capillary cell, with particular care being taken to ensure no bubbles are present to

disrupt electrolyte continuity between the two electrodes. This is done using a disposable 1 mL syringe by delicately inserting the needle into the open half-capillary cell until it contacts the graphite electrode tip within. The needle is slowly withdrawn while electrolyte is injected, so that the displacement of the needle itself does not give rise to bubble formation. The electrolyte should be filled to the very tip of the capillary before the next step, as insertion of the current collector can force air pockets into the cell otherwise. Once electrolyte is filled, the cell is held horizontally with surface tension preventing any electrolyte spills, and the copper current collector is carefully inserted into the capillary, lithium side first, to a depth of ~2 cm, leaving a small gap between working electrode and current collector. It is worth noting that this insertion displaces small quantities of electrolyte from the cell, so having a Kimwipe on hand to absorb this displaced electrolyte is recommended. Before sealing the current collector, it is important to keep the cell horizontal to prevent the current collector slipping further in or out of the capillary, which can result in an electrical short or detrimental bubble formation, respectively. The current collector end is sealed in an identical manner to the half-capillary sealing procedure outlined above, with molten wax being dripped over the capillary-copper junction to form an inert sealing bead, and epoxy being applied over this bead to provide mechanical stability. The epoxy seal is allowed to dry for at least 30 minutes, and once this is completed the capillary cell is ready for cycling.

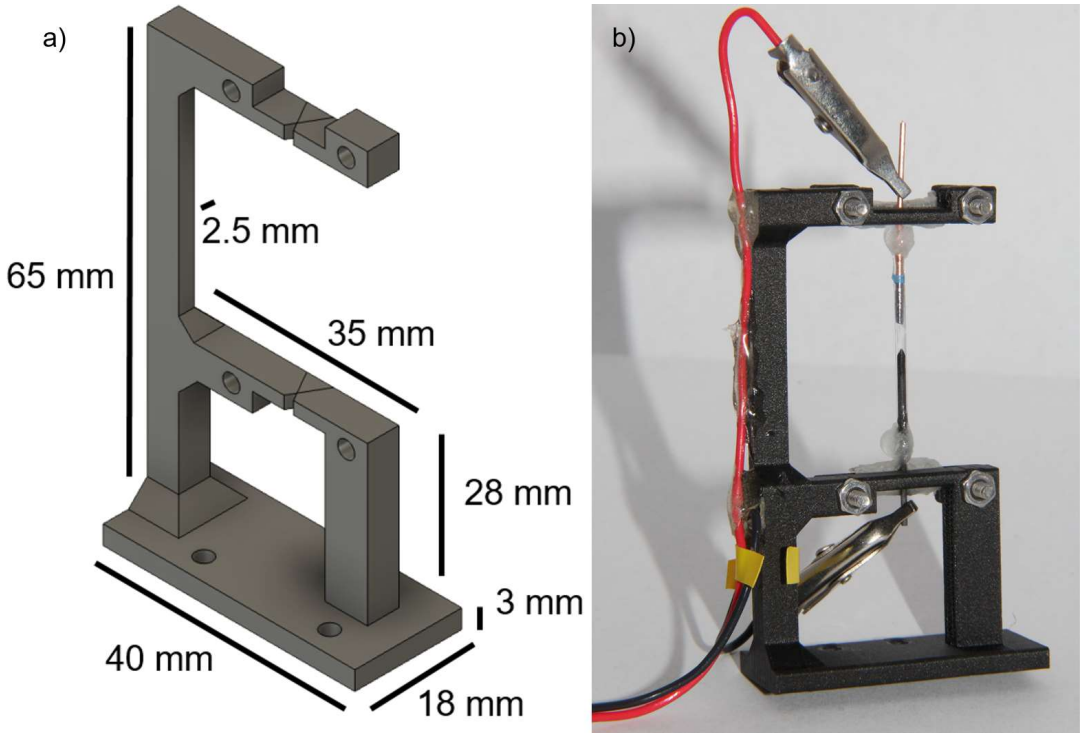

Figure 4.2: Custom capillary cell mount. a) Model of mount with specific dimensions. b) Functional mount electronically connected to a capillary cell.

To utilize a non-traditional battery cell geometry such as this capillary cell, a new cell mount must be designed. The main considerations for this mount design is it must prevent any motion of the cell, it must provide torque points for the wires necessary to electrochemically cycle a cell so they do not torque on the cell itself, and it must occlude as few angles as possible to maximize data quality. With these considerations in mind, a mount was designed that can be seen in Figure 2. Holding the cell from both electrodes prevents any undesired movement of the cell during stage rotation, a pair of secondary wires mechanically attached the mount prevents any torqueing on the cell from potentiostat wires, and the spine of the mount is deliberately kept thin to minimize occluded angles during rotation. It should be noted that this cell was designed for the specific stage conditions at Stanford Synchrotron Radiation Lightsource (SSRL) beamline #6-2,

and that different synchrotrons will have unique stage dimensions to consider when designing an appropriate mount.

4.5: Safety.

The primary safety concerns for this cell assembly are almost unanimously involved with the inherent dangers in using a hotplate. The quantity of lithium electroplated onto the copper current collector is negligible, as is the volume of electrolyte necessary to fill the cell, and neither present a notable safety issue.

4.6: Troubleshooting.

The PVDF in NMP binder solution selected for this cell assembly was chosen specifically for two reasons. Many alloy anode systems utilize carboxymethyl cellulose (CMC) as a binder due to its rigidity and ability to resist volume expansion in active particles, but prolonged radiation exposure during TXM imaging can degrade CMC binder and result in particle drift and disconnection from the surrounding conductive matrix. PVDF is significantly more stable in radiation, allowing for a greater amount of exposure before degradation, which is crucial for tomography gathering. In addition, the organic NMP solvent allows this slurry to wet the graphite tip effectively, and provides a more even distribution of active material when dried.

The slurry deposition on the graphite tip is a vitally important step for successful gathering of topographies. The use of PVDF binder in NMP solvent is a necessary step to help prevent slurry clumping due to unfavorable solvent interactions with the graphite electrode surface. The purpose of the sharpened graphite tip is to isolate particles at the very top for unobstructed imaging at all angles, as discussed in the procedure section, but if the slurry clumps up during drying, many particles are clustered, even at the tip, preventing imaging. Similarly, slurry viscosity is an

important factor to control to ensure proper slurry deposition. A slurry solution should be dilute enough to prevent deposition of protruding slurry monoliths during drying, while remaining viscous enough to prevent active particles settling to the lowest point of the electrode due to gravity. For this application, a proper slurry application should provide a slight discoloration of the graphite tip, without changing the topography of the electrode shape itself.

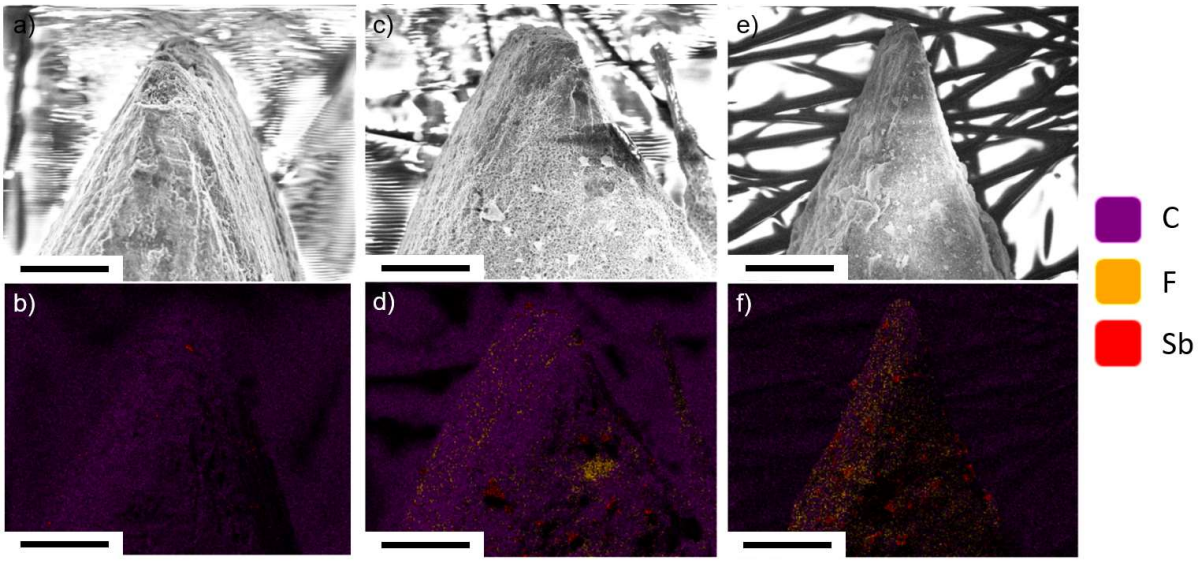

Figure 4.3: a) SEM image of dropcast tip. b) EDX image of same dropcast tip, showing very low active Sb particle presence. c) SEM image of dipcoated tip. d) EDX image of same dipcoated tip, showing low active Sb particle present and unusual slurry structures. e) SEM image of dropcast and wicked tip. f) EDX image of same dropcast and wicked tip, showing significant active Sb particle presence. All scale bars are 100 μm.

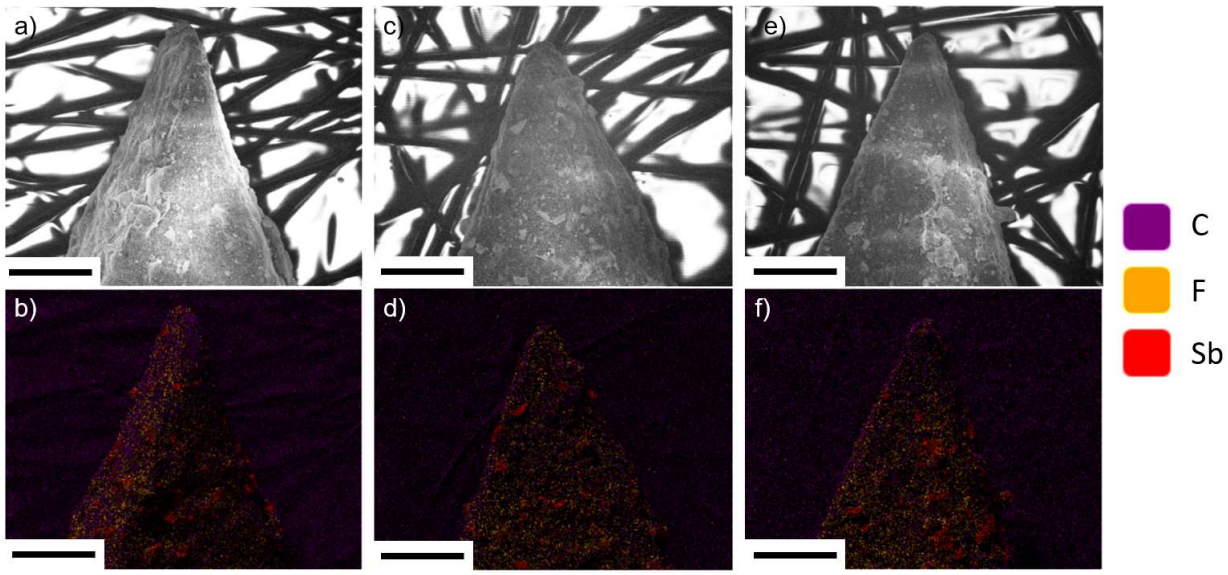

Figure 4.4: a,b) SEM and EDX image of horizontally dried electrode. c,d) SEM and EDX image of vertically dried electrode. e,f) SEM and EDX image of electrode dried at a 45° angle. All scale bars are 200 µm.

Several different methods of slurry deposition were explored in order to determine the ideal method for slurry deposition that produces an adequate quantity of uniformly distributed active material particles on the graphite electrode tip. Three different deposition methods were explored, a simple dropcasting method, a dipcoating method using acetone as a volatile solvent for fast drying, and a dropcasting method where excess solvent was wicked away using a Kimwipe before drying, and the tips were imaging using a scanning electron microscope (SEM) in conjunction with energy-dispersive X-ray spectroscopy (EDX), which can be seen in Figure 3. The simple dropcast electrode, seen in Figure 3a,b, shows very little active particle distribution on the tip, as does the dipcoated electrode in Figure 3c,d. In contrast, the dropcast and wicked method seen in Figure 3e,f reliably produces impressive active particle presence and uniform distribution, establishing itself as the ideal method for slurry deposition for this cell. After establishing the dropcast and wicked

deposition method as the superior method, the angle at which electrodes are dried in the vacuum oven were explored to determine if this also had an effect on slurry deposition quality. Using the dropcast and wicked deposition method, electrodes were then dried horizontally, vertically, and at a 45° angle. The SEM and EDX results for all three drying angles are show in Figure 4, and the results all demonstrate a good distribution of active particles on the electrode tip. The horizontally dried electrodes, seen in Figure 4a,b, appear to show a slightly greater proclivity to deposit active particles up to the absolute tip of the electrode, and was selected as the drying angle for this cell assembly.

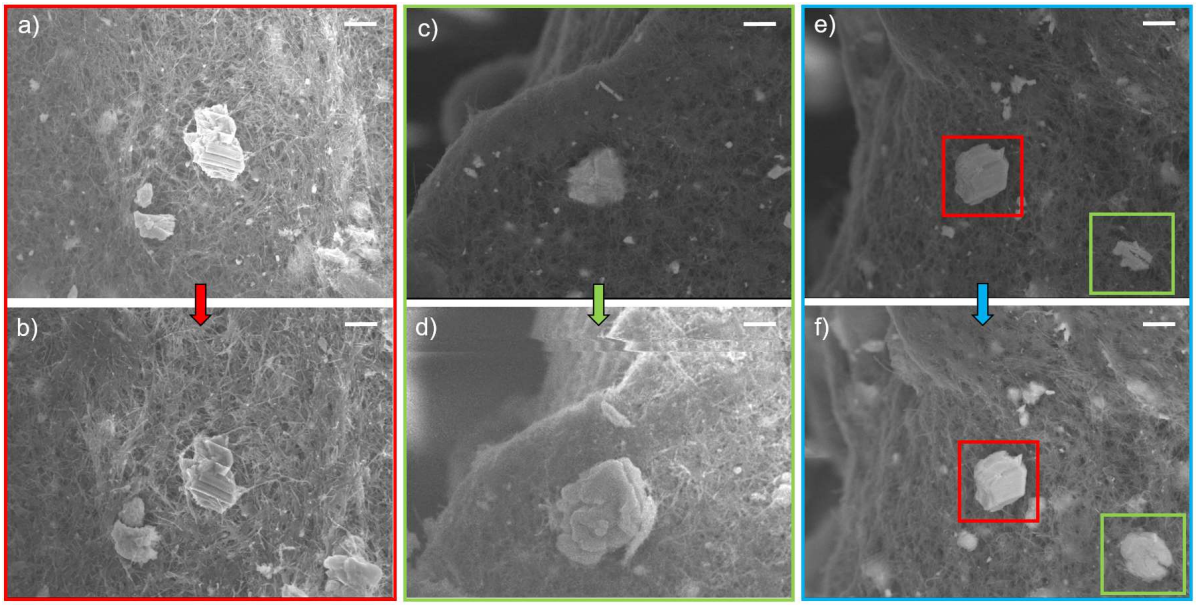

Figure 4.5: SEM images of particles before and after electrochemical sodiation. a,b) Particle on surface of slurry that failed to sodiate, with a) pristine and b) post sodiation. c,d) Particle embedded deeper in slurry that successfully sodiated, with c) pristine and d) post sodiation. e,f) Two particles that demonstrate depth dependence on successful sodiation, with e) pristine and f) post sodiation, where red highlighted particle on surface failed to sodiate, and green highlighted particle embedded deeper in slurry successfully sodiated. All scale bars are 10 µm.

Even in an ideal battery environment with an appropriate stack pressure, there is a portion of active particles that will fail to perform electrochemically for a variety of factors, and this portion is predictably greater in this non-ideal cell environment. As *in-situ* tomography experiments require a substantial time investment, it is important to select a particle that will perform electrochemically so the relevant data can be gathered. To gain insight into this issue, graphite electrodes were cycled in a glovebox inert environment, and imaged *ex-situ* with an SEM. The images of representative particles that cycled or failed to cycle are shown in Figure 5. By imaging the same electrode before and after electrochemical sodiation, it is possible to highlight the different behavior of two types of particles: particles that are exposed on the surface of the slurry, and particles that are buried in the conductive matrix. Particles buried deeper in the slurry, seen in Figure 5c-d, perform electrochemically at a much higher rate than particles on the surface, seen in Figure 5a-b, as particles on the surface either are not well electronically connected, or detach from the conductive matrix early in the first cycle. Figure 6 helps visualizes the difference between what are referred to as surface particles, and particles embedded deeper in conductive carbon matrix. This preferential electrochemical performance of particles embedded deeply in carbon matrix should be strongly considered during particle selection while setting up an *in-situ* TXM tomography experiment.

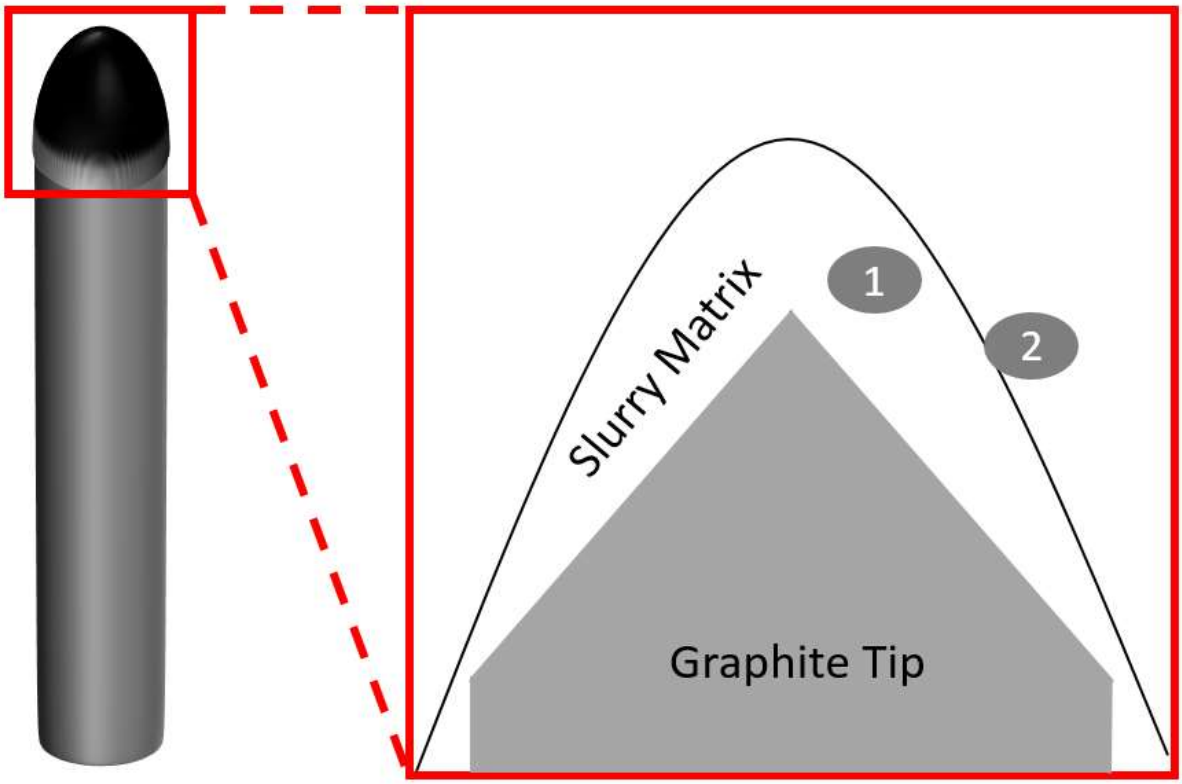

Figure 4.6: Cartoon cross-sectional representation of slurry deposited on graphite electrode tip. Active particle 1 is embedded deeper in conductive matrix and likely to demonstrate superior electrochemical performance than particle 2, which is instead only attached at slurry surface.

Besides the obvious extensively discussed benefits this cell provides to *in-situ* 3D tomography imaging, the strength of this cell lies in its adaptability. While the dimensions of the cell described here were used to successfully gather tomographic datasets, none of these specific dimensions or parameters are essential for cell operation. Different electrode materials and lengths can be easily integrated into a custom cell, different slurry compositions can be employed to deposit a slurry of desired properties, different electrode tip shapes can be used to image different slurry environments in this cell. Even more importantly, not only can a wide range of active materials be imaged in this cell by simply depositing a different slurry on the graphite electrode,

but this cell could be operated as a full cell by pairing two appropriate electrodes together in the capillary and could be easily adapted to accommodate different systems such as sodium or potassium ion batteries. This low-tech cell design lends itself to simple modification, and is poised to enable access to *in-situ* 3D tomography imaging for a wide range of energy storage systems.

4.7: Characterization.

Tomographic datasets are collected as a series of 2D TXM projection images from -90° to +89° (180 projections at 1° angular resolution) or to +89.5° (360 projections at 0.5° angular resolution). The projections are prepared for reconstruction using a two-step alignment procedure. The reference-corrected projections are first manually aligned to the center of rotation of a particle using TXMWizard.[43] Next, the projections are cropped, any obstructed angles are removed, and the manually-aligned projections are imported into TomoPyUI, a graphical user interface for TomoPy.[44,45] The center of rotation of the particle is refined to minimize the image entropy of the central slice. The manual alignment is then refined using the joint iterative reprojection alignment algorithm until convergence.[46] The reprojected dataset is then recentered and realigned iteratively until the image entropy of the central slice converges to a minimum. The computationally-aligned projections are then reconstructed using the simultaneous iterative reconstruction technique algorithm (SIRT) for 5 iterations to generate a 3D reconstruction.[47] The reconstructed 3-dimensional dataset is then evaluated in Dragonfly for volume measurements, qualitative assessment of the particle interior, and pore space mapping using image segmentation.

4.8: Discussion.

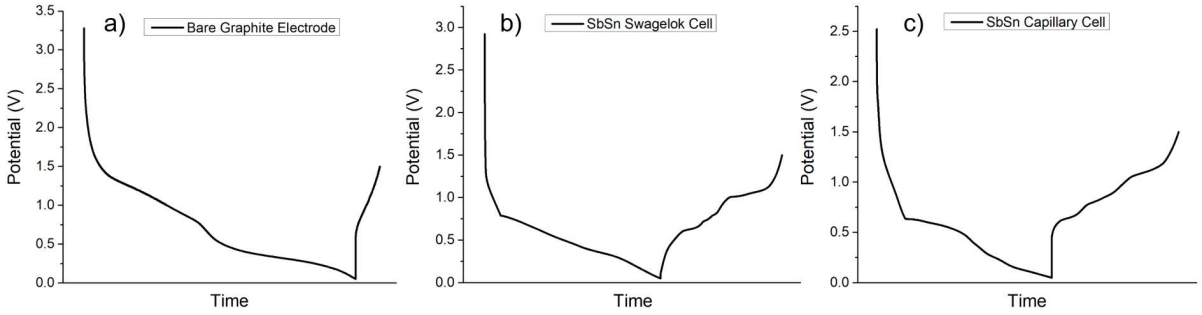

Figure 4.7: a) GV of bare graphite electrode, cycled in capillary cell environment. b) GV of SbSn system cycled in an ideal Swagelok cell environment. c) GV of SbSn system cycled in capillary cell environment.

A comparison of representative galvanostats demonstrates the ability of this capillary cell to electrochemically perform. Figure 7a shows the galvanostat for a capillary cell cycling with no active slurry, just a bare graphite electrode. The electrochemical contribution of the graphite can be observed, and the irreversibility of lithation intercalation is evident. Figure 7b is the galvanostat of an SbSn system in an ideal cell environment, and Figure 7c is the galvanostat of this same SbSn system cycled in a capillary cell. While the lithiation step can be slightly less clear, the delithation step in both the ideal cell and the capillary cell environments shows definitive SbSn electrochemical activity, with multiple visible plateaus corresponding to delithiation of Sn and Sb components. This clear delithation of SbSn allows for positive identification of successful electrochemical cycling of active material in the capillary cell, similar to the electrochemical cycling we observe in an idea cell environment. It is important to note that the lack of stack pressure within this flooded cell design makes subsequent cycles increasingly difficult, as active material has a tendency to delaminate from the graphite electrode after the first cycle.

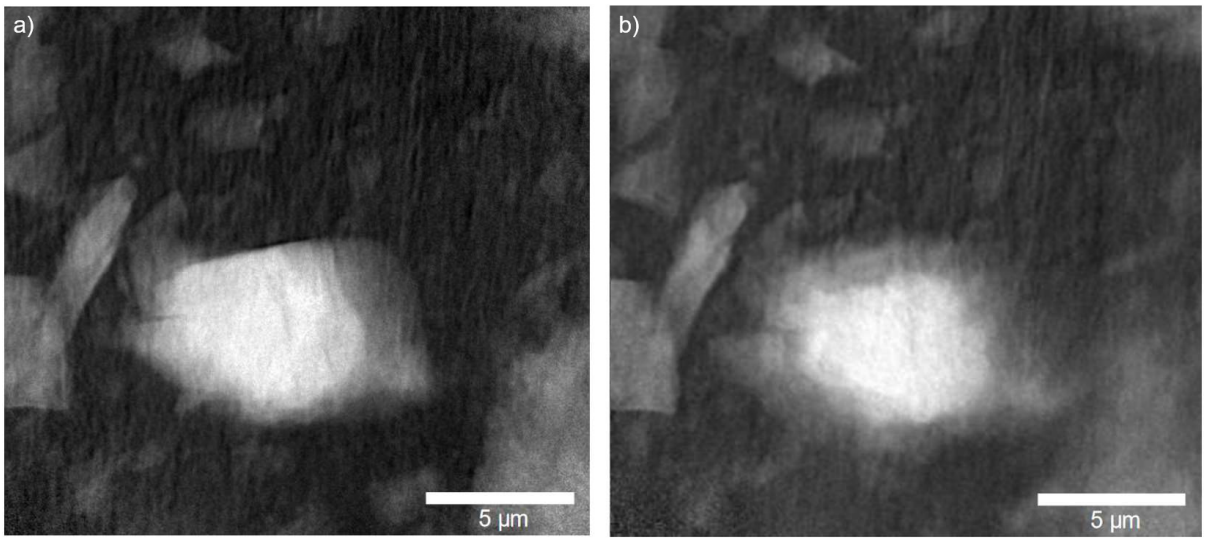

Figure 4.8: 2D TXM images of Sb particle taken *in-situ* in capillary cell. a) Pristine Sb particle before lithation. b) Same particle after partial lithiation.

TXM images taken on particles within this cell demonstrate the transparency of components within this cell, highlighting the active particles being imaged. In Figure 8a, a 2D image of Sb can be observed before cycling, and in Figure 8b this same particle can be seen after partial lithiation, showing the expanding, low contrast shell of the propagating lithiated phase surrounding the dense, unlithiated Sb core. The quality 2D TXM images across a wide range of angles that this cell provides access to can be used for areal expansion analysis and observation of dramatic structural evolution during electrochemical cycling, and then can be reconstructed into 3D tomographic models for volume expansion calculations and analysis of interior architecture changes.

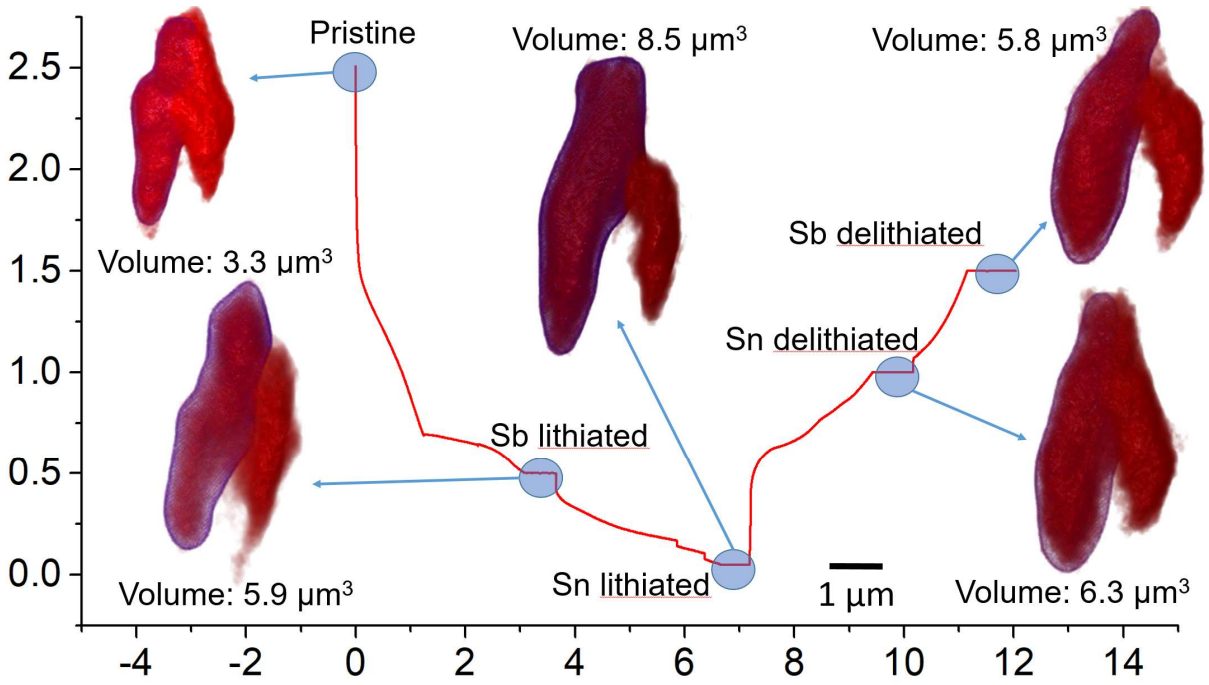

Figure 4.9: Galvanostat of *operando* cycling of capillary cell. Sharp highlighted plateaus indicate regions where potential was held constant during the gathering of tomographic dataset. Associated tomographic reconstructions are displayed next to the relevant galvanostat region, along with calculated particle volume for the area outlined in blue at each particle state of charge.

In Figure 9, the galvanostat of a successfully cycled *operando* SbSn capillary cell is shown along with the associated reconstructions. The horizontal plateaus on the galvanostat correspond to relevant states of charge, where the potential was pinned briefly while the tomographic dataset was collected, in order to prevent any further electrochemical changes to the particle during the data gathering process. The reconstructions in Figure 9 clearly show two distinct particles that are contacting each other, and the associated volume values displayed in this figure are for the left-hand particle only. The volume shows a trend that is expected of an alloy anode material, volume

expansion during lithiation, and subsequent contraction during delithiation, confirming the electrochemical performance of this particle during cycling.

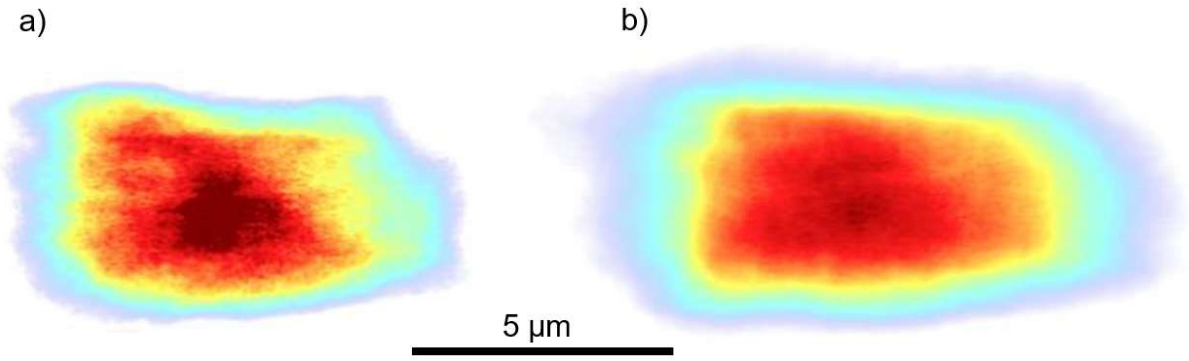

Figure 4.10: Interior slices into active Sb particle, heatmap gradient indicates increasing electron density. a) Interior view of pristine Sb particle. b) Interior view of same particle after undergoing partial lithation.

Tomographic reconstructions provide more than just another way to evaluate volume expansion, but also allow a view into the evolution of interior architectures of electrochemically active particles during cycling. Figure 10 shows this interior view, where the heatmap colors denote electron density and are globally scaled across images. Figure 10a shows an interior view of a pristine Sb particle, where the dark region in the center is representative of a dense, unlithiated core. Figure 10b shows this same particle after partial lithation, where the expanded low density fringe surrounding the particle suggests a highly lithiated phase, and the loss of electron density in the center indicates lithium-ion penetration throughout the entire particle. These techniques demonstrate just a few of the ways these tomographic datasets can be analyzed, and motivate use of this capillary cell design as a simple method to gather these *operando* tomographic datasets.

4.9: Conclusions.

The cell design described here provides access to the powerful analytical technique of *in-situ* 3D TXM tomography imaging for electrochemical systems. The 3D model reconstructions that result from a successful tomography experiment provide unparalleled insight into the mechanical evolution, internal and external, of active particles and their nanoporous networks. While this capillary cell has been demonstrated here to operate effectively to gather 3D tomography data as a lithium-ion half-cell battery for anode materials, it can easily be modified to analyze cathode materials, a full-cell, or even additional battery systems such as sodium or potassium-ion batteries. While many other cells designed for *in-situ* 3D tomography experiments require complicated machining of custom parts or other specialized components, this cell design relies entirely on cheap, common materials that can often be found in a research lab or ordered from any vendor. This low tech cell design allows different research groups to access this analytical technique regardless of their level of involvement in the energy storage research field. By enabling easy access to *in-situ* 3D tomography datasets, this cell is poised to increase the prevalence of 3D analysis of active particles and improve understanding of energy storage materials as a whole.

4.10: References.

[1] Blomgren, G. E. The Development and Future of Lithium Ion Batteries. *Journal of The Electrochemical Society*. **2017**, 164, A5019.

[2] Winter, M.; Brodd, R. What Are Batteries, Fuel Cells, and Supercapacitors? *Chemical Reviews*, **2004**, 104, 4245 – 4269.

[3] Goodenough, J.B.; Kim, Y. Challenges for Rechargeable Li Batteries. *Chemistry of Materials*, **2010**, 22, 587 – 603.

[4] Tarascon, J.M.; Armand, M. Issues and challenges facing rechargeable lithium batteries. *Nature*, **2001**, 414, 359 – 367.

[5] Moyassari, E.; Roth, T.; Kucher, S.; Chang, C.-C.; Hou, S.-C.; Spingler, F.B.; Jossen, A. The Role of Silicon in Silicon-Graphite Composite Electrodes Regarding Specific Capacity, Cycle Stability, and Expansion. *Journal of The Electrochemical Society*, **2022**, 169, A010504.

[6] An, S.J.; Li, J.; Daniel, C.; Mohanty, D.; Nagpure, S.; Wood, D.L.W. The state of understanding of the lithium-ion-battery graphite solid electrolyte interphase (SEI) and its relationship to formation cycling. *Carbon*, **2016**, 105, 52 – 76.

[7] Bruce, P.G.; Freunberger, S.A.; Hardwick, L.J.; Tarascon, J.M. Li-O_2 and Li-S batteries with high energy storage. *Nat. Mater.* **2012**, 11, 19 – 29.

[8] Wu, C.; Dou, S.-X.; Yu, Y. The State and Challenges of Anode Materials Based on Conversion Reactions for Sodium Storage. *Small*, **2018**, 14, A1703671.

[9] Yu, S.-H.; Lee, S. H.; Lee, D. J.; Sung, Y.-E.; Hyeon, T. Conversion Reaction-Based Oxide Nanomaterials for Lithium Ion Battery Anodes. *Small*, **2015**, 12, 2146 – 2172.

[10] Li, H.; Yamaguchi, T.; Matsumoto, S.; Hoshikawa, H.; Kumagai, T.; Okamoto, N. L.; Ichitsubo, T. Circumventing hugh volume strain in alloy anodes of lithium batteries. *Nat. Commun.* **2020**, 11, A1584.

[11] Chen, J.; Cheng, F. Combination of Lightweight Elements and Nanostructured Materials for Batteries. *Acc. Chem. Res.* **2009**, 42, 713 – 723.

[12] Arico, A. S.; Bruce, P.; Scrosati, B.; Tarascon, J.-M.; Schalkwijk, W. Nanostructured materials for advanced energy conversion and storage devices. *Nature Mater.* **2005**, 4, 366 – 377.

[13] Cook, J. B.; Detsi, E.; Liu, Y.; Liang, Y.-L.; Kim, H.-S.; Petrissans, X.; Dunn, B.; Tolbert, S. H. Nanoporous Tin with a Granular Hierarchical Ligament Morphology as a Highly Stable Li-Ion Battery Anode. *ACS Appl. Mater. Interfaces*, **2017**, 9, 293 – 303.

[14] Lim. C.-H.; Selvaraj, B.; Song, Y.-F.; Wang, C.-C.; Jin, J.-T.; Huang, S.-S.; Chuang, C.-H.; Sheu, H.-S.; Liao, Y.-F.; Wu, N.-L. Insight into microstructural and phase transformations in electrochemical sodiation-desodiation of a bismuth particulate anode. *J. Mater. Chem. A.* **2017**, 5, 21536 – 21541.

[15] Detsi, E.; Petrissans, X.; Yan, Y.; Cook, J. B.; Deng, Z.; Liang, Y.-L.; Dunn, B.; Tolbert, S. H. Tuning ligament shape in dealloyed nanoporous tin and the impact of nanoscale morphology on its applications in Na-ion alloy battery anodes. *Phys. Rev. Mater.* **2018**, 2, A055404.

[16] Wang, Y.; Pu, J.; Wang, L.; Wang, J.; Jiang, Z.; Song, Y.-F.; Wang, C.-C.; Wang, Y.; Jin, C. Characterization of typical 3D pore networks of Jiulaodong formation shale using nano-transmission X-ray microscopy. *Fuel*. **2016**, 170, 84 – 91.

[17] Chen-Wiegart, Y.-C. K.; Shearing, P.; Yuan, Q.; Tkachuk, A.; Wang, J. 3D morphological evolution of Li-ion battery negative electrode $LiVO_2$ during oxidation using X-ray nano-tomography. *Electrochem. Commun.* **2012**, 21, 58 – 61.

[18] Larsson, E.; Gürsoy, D.; Carlo, F. D.; Lilleodden, E.; Storm, M.; Wilde, F.; Hu, K.; Müller, M.; Greving, I. Nanoporous gold: a hierarchical and multiscale 3D test pattern for characterizing X-ray nano-tomography systems. *J. Synchrotron Radiat.* **2019**, 26, 194 – 204.

[19] Tang, F.; Wu, Z.; Yang, C.; Osenberg, M.; Hilger, A.; Dong, K.; Markötter, H.; Manke, I.; Sun, F.; Chen, L.; *et al*. Synchrotron X-Ray Tomography for Rechargeable Battery Research: Fundamentals, Setups, and Applications. *Small*, **2021**, 5, A2100557.

[20] Chen-Wiegart, Y.-C. K.; Liu, Z.; Faber, K. T.; Barnett, S. A.; Wang, J. 3D analysis of a $LiCoO_2$-$Li(Ni_{1/3}Mn_{1/3}Co_{1/3})O_2$ Li-ion battery positive electrode using x-ray nano-tomography. *Electrochem. Commun.* **2013**, 28, 127 – 130.

[21] Chen-Wiegart, Y.-C. K.; Cronin, J. S.; Yuan, Q.; Yakal-Kremski, K. J.; Barnett, S. A.; Wang, J. 3D Non-destructive morphologicl analysis of a solid oxide fuel cell anode using full-field X-ray nano-tomography. *J. Power Sources,* **2012**, 218, 348 – 351.

[22] Zhao, C.; Wada, T.; Andrade, V. D.; Gürsoy, D.; Kato, H.; Chen-Wiegart, Y.-C. K. Imaging of 3D morphological evolution of nanoporous silicon anode in lithium ion battery by X-ray nano-tomography. *Nano Energy,* **2018,** 52, 381 – 390.

[23] Pattammattel, A.; Tappero, R.; Ge, M.; Chu, Y. S.; Huang, X.; Gao, Y.; Yan, H. High-sensitivity nanoscale chemical imaging with hard x-ray nano-XANES. *Sci. Adv.* **2020**, 6, A3615.

[24] Liu, Y.; Meirer, F.; Wang, J.; Requena, G.; Williams, P.; Nelson, J.; Mehta, A.; Andrews, J. C.; Pianetta, P. 3D elemental sensitive imaging using transmission X-ray microscopy. *Anal. Bioanal. Chem.* **2012**, 404, 1297 – 1301.

[25] Nguyen, T.-T.; Villanova, J.; Su, Z.; Tucoulou, R.; Fleutot, B.; Delobel, B.; Delacourt, C.; Demortière, A. 3D Quantification of Microstructural Properties of $LiNi_{0.5}Mn_{0.3}Co_{0.2}O_2$ High-Energy Density Electrodes by X-Ray Holographic Nano-Tomography. *Adv. Energy Mater.* **2021**, 11, A2003529.

[26] Zeller-Plumhoff, B.; Laipple, D.; Slominska, H.; Iskhakova, K.; Longo, E.; Hermann, A.; Flenner, S.; Greving, I.; Storm, M.; Willumeit-Römer, R. Evaluating the morphology of the degredation layer of pure magnesium *via* 3D imaging at resolutions below 40 nm. *Bioact. Mater.* **2021**, 6, 4368 – 4376.

[27] Ge, M.; Coburn, D. S.; Nazaretski, E.; Xu, W.; Gofron, K.; Xu, H.; Yin, Z.; Lee, W.-K. One-minute nano-tomography using hard X-ray full-field transmission microscope. *Appl. Phys. Lett.* **2018**, 113, A083109.

[28] Lou, S.; Sun, N.; Zhang, F.; Liu, Q.; Wang, J. Tracking Battery Dynamics by Operando Synchrotron X-ray Imaging: Operation from Liquid Electrolytes to Solid-State Electrolytes. *Acc. Mater. Res.* **2021**, 2, 1177 – 1189.

[29] Mayorga-González, R.; Rivera-Torrente, M.; Nikolopoulos, N.; Bossers, K. W.; Valadian, R.; Yus, J. Seoane, B.; Weckhuysen, B. M.; Meirer, F. Visualizing defects and pore connectivity

within metal-organic frameworks by X-ray transmission tomography. *Chem. Sci.* **2021**, 12, 8458 – 8467.

[30] Yu, Z.; Li, R.; Cai, K.; Yao, Y.; Deng, J.; Lou, S.; Lu, M.; Pan, Q.; Yin, G.; Jiang, Z.; *et al*. Unraveling the advances of trace doping engineering for potassium ion battery anodes via tomography. *J. Energy Chem.* **2021**, 58, 355 – 363.

[31] Fathiannasab, H.; Kashkooli, A. G.; Li, T.; Zhu, K.; Chen, Z. Three-Dimensional Modeling of All-Solid-State Lithium-Ion Batteries Using Synchrotron Transmission X-ray Microscopy Tomography. *J. Electrochem. Soc.* **2020**, 167, A100558.

[32] Torayev, A.; Rucci, A.; Magusin, P. C. M. M.; Demortière, A.; Andrade, V. D.; Grey, C. P.; Merlet, C.; Franco, A. A. Stochasticity of Pores Interconnectivity in Li-O_2 Batteries and its Impact on the Variations in Electrochemical Performance. *J. Phys. Chem. Lett.* **2018**, 9, 791 – 797.

[33] Brennhagen, A.; Cavallo, C.; Wragg, D. S.; Sottmann, J.; Koposov, A. Y.; Fjellvåg, H. Understanding the (De)Sodation Mechanisms in Na-Based Batteries through Operando X-Ray Methods. *Batter. Supercaps*, **2021**, 4, 1039 – 1063.

[34] Wang, L.; Wang, J.; Guo, F.; Ma, L.; Ren, Y.; Wu, T.; Zuo, P.; Yin, G.; Wang, J. Understanding the intial irreversibility of metal sulfides for sodium-ion batteries *via operando* techniques. *Nano Energy*, **2018**, 43, 184 – 191.

[35] Li, T.; Lim, C.; Cui, Y.; Zhou, X.; Kang, H.; Yan, B.; Meyerson, M. L.; Weeks, J. A.; Liu, Q.; Guo, F.; *et al. In situ* and *operando* investigation of the dynamic morphological and phase changes of a selenium-doped germanium electrode during (de)lithiation processes. *J. Mater. Chem.* **2020**, 8, 750 – 759.

[36] Tan, C.; Daemi, S. R.; Taiwo, O. O.; Heenan, T. M. M.; Brett, D. J. L.; Shearing, P. R. Evolution of Electrochemical Cell Designs for In-Situ and Operando 3D Characterization. *Materials*, **2018**, 11, A2157.

[37] Obrovac, M.N.; Chevrier, V. L. Alloy Negative Electrodes for Li-Ion Batteries. *Chem. Rev.* **2014**, 114, 11444 – 11502.

[38] Park, C.-M.; Kim, J.-H.; Kim, H.; Sohn, H.-J. Li-alloy based anode materials for Li secondary batteries. *Chem. Soc. Rev*. **2010**, 39, 3115 – 3141.

[39] Zhao, Y.; Manthiram, A. High-Capacity, High-Rate Bi-Sb Alloy Anodes for Lithium-Ion and Sodium-Ion Batteries. *Chemistry of Materials*, **2015**, 27, 3096 – 3101.

[40] Augustyn, V.; Come, J.; Lowe, M. A.; Kim, J. W.; Taberna, P.-L.; Tolbert, S. H.; Abruña, H. D.; Simon, P.; Dunn, B. High-rate electrochemical energy storage through Li^+ intercalation pseudocapacitance. *Nature Mater.* **2013**, 12, 518 – 522.

[41] Cook, J. B.; Lin, T. C.; Detsi, E.; Weker, J. N.; Tolbert, S. H. Using X-ray Microscopy to Understand How Nanoporous Materials Can Be Used to Reduce the Large Volume Change in Alloy Anodes. *Nano Letters*, **2017**, 17, 870 – 877.

[42] Tian, H.; Xin, F.; Wang, X.; He, W.; Han, W. High capacity group-IV elements (Si, Ge, Sn) based anodes for lithium-ion batteries. *J. Materiomics*, **2015**, 1, 153 – 169.

[43] Liu, Y.; Meirer, F.; Williams, P. A.; Wang, J.; Andrews, J. C.; Pianetta, P. TXM-Wizard: A Program for Advanced Data Collection and Evaluation in Full-Field Transmission X-Ray Microscopy. *J. Synchrotron Radiat.* **2012**, *19* (2), 281–287.

[44] Gürsoy, D.; De Carlo, F.; Xiao, X.; Jacobsen, C. TomoPy: a Framework for the Analysis of Synchrotron Tomographic Data. *J. Synchrotron. Radiat.* **2014**, *21*, 1188−1193.

[45] Welborn, S. S. *TomoPyUI*; https://github.com/swelborn/tomopyui

[46] Gürsoy, D.; Hong, Y. P.; He, K.; Hujsak, K.; Yoo, S.; Chen, S.; Li, Y.; Ge, M.; Miller, L. M.; Chu, Y. S.; et al. Rapid Alignment of Nanotomography Data Using Joint Iterative Reconstruction and Reprojection. *Sci. Rep.* **2017**, *7*, 1−12.

[47] Pelt, D. M.; Gürsoy, D.; Palenstijn, W. J.; Sijbers, J.; De Carlo, F.; Batenburg, K. J. Integration of TomoPy and the ASTRA Toolbox for Advanced Processing and Reconstruction of Tomographic Synchrotron Data. *J. Synchrotron Radiat.* **2016**, *23*, 842− 849.

CHAPTER 5: Conclusions

Utilizing *operando* XRD and PDF, the stabilizing effects of nanoporous architectures on multicomponent alloy anodes was determined. In the representative multicomponent alloy anode system SbSn, the kinetics of phase separation between the Sb and Sn components is significantly improved when compared to the bulk counterpart, which reduces internal strain within particles and helps mitigate particle pulverization. The PDF data determined that the highest lithiated phase reached by Sn component to be Li_7Sn_3, though it is amorphous. By examining the cycling behavior of Sb when cycled with both lithium and sodium, the role of amorphous intermediates was explored. *Operando* XRD and TXM showed the remarkable reversibility of active Sb particles when cycled with sodium rather than lithium. This behavior, despite the increased size of the sodium ion, is attributed to the fact that Sb passes entirely through amorphous intermediates when (de)sodiated, whereas all intermediates are crystalline when (de)lithiated. The ductile nature of amorphous materials is shown to contribute greatly towards particle reversibility and stability.

Accessing *operando* 3D TXM tomography is a challenging experiment, but the design of the novel capillary cell has been demonstrated to successfully provide a low-tech, effective pipeline to gathering these data sets. The design and assembly parameters were published in order to provide access to this technique for any research group that would benefit from tomography data. A porous SbSn system was cycled and *operando* tomography data was gathered at several relevant states of charge. The 3D models reconstructed from this data provided a detailed glimpse into particle evolution during cycling, including particle true volume expansion and a glimpse into the evolution of interior pore structure.

APPENDIX A: Pouch Cell Assembly Procedures for *Operando* Synchrotron Cell

Before conducting *operando* TXM studies at SSRL, pouch cells must be assembled that will be able to perform electrochemically, isolate active particles for imaging, and will fit in the specific mount provided at the beamline. A lithium pouch cell consists of 6 major components: an active electrode, a Celgard separator, a piece of lithium, a small volume of lithium electrolyte, two nickel electrode tabs, and two pieces of Mylar cut into rectangles with dimensions of 1 inch by 3/4ths of an inch. A large portion of the cell assembly can be done in air, with only the final assembly steps requiring the inert atmosphere of a glovebox.

For battery slurry prep, a low mass loading is utilized to encourage particle separation for clear imaging of individual particles. The slurry by mass is prepared as 25% active material, 50% carbon additive, and 25% PVDF binder. PVDF is used in this case even though it isn't ideal for alloy anode materials, as PVDF shows increased stability during radiation exposure, while traditional CMC binder softens and allows particles to drift out of the field of view or become electronically disconnected entirely. This slurry, due to its abnormally high carbon content, can be much more challenging to prepare than a typical battery slurry, as the abundance of carbon can result in chunky, nonhomogeneous slurries. To alleviate some of these issues, the active material and carbon components are weighed out first, combined in a clean mortar, and gently crushed together for several minutes with a pestle. This can help incorporate the active material evenly in the carbon component, before mixing with the binder solution. The PVDF binder solution is then added to the same mortar that already contains the carbon and active components, and all are mixed together with a pestle. NMP is added dropwise until the slurry has reached a desired consistency, then the slurry is carefully scraped from the mortar. This slurry is then cast on a copper substrate,

using a doctor blade to ensure a slurry thickness of 25 μm, and dried overnight in a vacuum oven at 80 °C. Electrodes are then punched out of the dried slurry for use in pouch cell assembly.

The majority of pouch cell assembly can be done in atmosphere, so that the only steps needing to be done in inert atmosphere are the addition of air sensitive materials such as lithium metal and lithium electrolyte, significantly simplifying assembly procedure. Nickel electrode tabs are prepared for use by cutting to an appropriate length, ~3/4ths of an inch, with a pair of scissors. The square cut ends of these tabs are rounded off with scissors into semicircles, and then the cut section of the tab is gently rubbed with sandpaper to remove any potential metal burrs that could puncture Celgard separator or Mylar cell components. Once these nickel tabs are prepared, they are placed side by side between the two Mylar pieces, extending lengthwise into the cell. It is important to have the attached sealing pieces on nickel tabs in contact with one another at the top sealing edge of the cell, in order to prevent electrolyte leakage between the two tabs. The top of this Mylar and nickel tab assembly is then sealed using an induction sealer. One of the previously prepared active electrodes is attached to one of the nickel tabs using a small piece of electrochemically inert Kapton tape, making sure slurry side is facing into the “interior” of the cell, and the back of the copper substrate is making good electrical contact with the nickel tab. A piece of Celgard is then gently inserted between the electrode, making sure to split the two nickel tabs on opposite sides of the separator, and being sized appropriately so it doesn’t intrude on the three remaining sealing surfaces of the cell. This half assembled cell can then be carefully pumped into the glovebox for further assembly, using a weight to keep the antechamber vacuum from damaging or displacing the cell.

Inside the inert glovebox assembly, the rest of the cell assembly can be completed. A thin, polished lithium disk is slipped into the interior of the cell, on the opposite side of the Celgard

separator from the active electrode previously added. Careful care must be taken to ensure the lithium disk makes good electrochemical contact with the nickel tab, is in the center of the Mylar cell component, and completely covers the electrode on the other side of the Celgard in order to ensure complete lithiation of all active particles. With the insertion of this lithium disk, both sides of the Mylar cell are then sealed using an induction sealer, making sure the lithium disk doesn't slip out of position. At this time, the only part of the cell that should be open is the bottom edge. A 1 mL disposable syringe is used to inject ~100 μL of 1 M $LiPF_6$, making sure to not puncture Celgard separator or disrupt alignment of cell components with the needle, and allow electrolyte to be introduced without any fouling of the final sealing surface. After electrolyte addition, a small piece of Kimwipe can be used to make sure there is no electrolyte on the sealing surface of the bottom of the cell, and then the bottom edge of the cell can finally be sealed with an induction sealer. With cell fully assembled and sealed, OCV can be checked using a potentiostat to make sure no cell shortages have occurred. For transportation to SSRL, pouch cell is then sealed inside a secondary container filled with glovebox atmosphere to limit prolonged air exposure until the experiment begins, and this sealed cell container can then be safely pumped out of glovebox.

APPENDIX B: General Overview for TXM Beamline 6-2c Operation at SSRL for Single Energy and XANES Imaging Experiments

Before performing *operando* TXM studies at SSRL Beamline 6-2c, appropriate electrochemical cells must be assembled. For 2D TXM, pouch cell geometries are ideal, as discussed in Appendix A, and for 3D TXM a novel capillary cell described in Chapter 4 is employed.

For 2D TXM, the pouch cell must be fitted horizontally into the pouch cell mount so that the small imaging slit is overlaid with the active electrode position. The 4 corner screws must be tightened carefully, finger tight, in order to provide stack pressure necessary for proper electrochemical performance without rupturing the cell. For most alloy anode experiments, a beam energy of 8950 eV is utilized to avoid image interference from other inactive cell components, as it is right below the Cu k-edge. Once the cell is mounted, the radiation is on, and the imaging slit has been located on the instrument, appropriate particles must be selected for imaging. For most 2D *operando* experiments, a total of 10 particles is selected. This is to gather a representative dataset which allows for comparison between particles, and also prevents potential problems if a single selected particle fails to electrochemically perform. For the 10 particles, it is important to select a wide range of particle sizes to observe differences in (de)lithiation behavior. Large particles that fill up most of the field of view should be avoided, since these particles typically undergo significant volume expansion that can exceed the field of view and prevent any coherent areal expansion insight from being extracted from the gathered data. Particles should also be selected that are globally separated from one another across the entire visible electrode surface, ideally at distances of ~100 μm. Slurries do not deposit perfectly uniform, and certain areas of the

slurry may perform differently, so selecting particles all across the electrode can help prevent any misinterpretation of particle behavior.

The easiest way to select particles for imaging is to take mosaic images, typically 10 x 10, which provides a massive field of view to identify suitable particles. The images taken are stacked edge to edge to produce one large image for analysis. The individual particles that appear to be suitable can be traveled to from this mosaic, by right clicking on the particle of interest and selecting "Go to Position." Each selected particle must be focused individually to ensure high image quality, and the easiest way to do this is to use focal series imaging. A focal series takes a number of images while traveling a set distance in the Z-axis, allowing a researcher to easily identify if focus is improving between individual images. It is best to take a series of 9 images, so that there is one image in the center of the image stack that corresponds to the original focal position. Focal series distances should start off large (~2000 μm) and depending on focusing quality, ideally should decrease the distance traveled by half between each series (2000 μm, 1000 μm, 500 μm, etc). After scanning through the focal series and deciding which image shows the best focus, once again right click on that image and select "Go to Position" and begin the next focal series with reduced Z-axis travel distance. There is little reason to go below a total distance of 250 μm, as you begin to run up against the resolution threshold of the instrument, making differences between images impossible to distinguish. Once a particle has been selected, positioned in the center of the field of view, and appropriately focused, save this file with a serial naming scheme such as Particle A or Particle 1. These image files will be used when setting up XMFlex to image automatically while the cell runs.

Once all 10 particles have been selected and focused, XMFlex is used to generate a script that will operate the beam without the need for external input. This is advantageous as it allows

the researcher to get food or sleep if necessary while the system runs automatically. The imaging method labeled as NAverage should be selected, which takes a rapid series of N images that will be averaged together to smooth out any beam aberration. It is typical to take 10 images, at either 0.5 or 1 second exposures depending on beam quality. A reference image must be loaded into the XMFlex program, to provide motor positions at which the program will take references each time it cycles through the 10 selected particles. A wait step between repeats must be input, and the wait time must be chosen at the discretion of the researcher in response to selected cycle rate for targeted electrochemistry, and number of images desired for an entire electrochemical cycle. Finally, an appropriate number of scan cycle repeats must be chosen so that the script continues to take images throughout the duration of the electrochemical cycle. Once all appropriate parameters have been set, clicking on "Generate Scan" will open a prompt window for file selection if everything has been set up correctly. At this time, the 10 image files corresponding to the 10 selected particles must be selected all at once, and once these 10 image files are selected XMFlex will automatically generate a script. It can be beneficial to read over the script steps for the first cycle of particles, to ensure no glaring errors have been committed. Once it is confirmed that everything was input properly, the "Execute Scan" button is clicked to start the program running. It is important to run this first series of images BEFORE beginning electrochemical cycling in order to provide a pristine data set independent of the electrochemical events that will occur for active particles during cycling. Once the first imaging series has been completed, and the script is on the rest step before the second imaging series, the electrochemical experiment should be started on the attached potentiostat. Once the electrochemistry has been confirmed to be running as expected, and the first pristine series of images have been taken successfully by the XMFlex program, the rest of the

experiment will run autonomously. However, it is advised that the researcher checks in on both the electrochemical performance, and the image dataset quality every couple of hours.

For 2D XANES experiments, the steps above will be followed exactly the same, all the way up until the XMFlex script setup, with a couple small changes. Firstly, the beam energy will be different. For an experiment targeting As, beam energies of 11840 eV and 11890 eV will be utilized to closely bracket the As k-edge absorption edge of 11866 eV. For setting up XMFlex for a XANES experiment, NAverage will still be selected. However, the option for multiple energy scans must ALSO be selected, and the two energies of 11840 eV and 11890 eV will be input. This will produce a scan which takes a series of images at one energy, changes the beam energy to the second value, and takes another series of images at this new energy. These images will be processed much the same as single energy TXM imaging, except the image intensity of the scan below the As k-edge energy will be subtracted from the image intensity of the scan above the As k-edge energy, producing a TXM image consisting of only the As elemental component, allowing this element to be tracked within a particle during electrochemical cycling.

For a 3D *operando* TXM tomography experiment utilizing the novel capillary cell described in Chapter 4, the experimental setup is significantly different than the 2D TXM imaging described above. A detailed experimental procedure is described in an essential document at the SSRL 6-2c beamline, and that procedure should be followed closely. However, this *operando* 3D cell requires some important deviations from that listed procedure, and that is what will be described in this section. Most notably, the entire TXM tomography alignment is expected to be done in continuous imaging mode. However, the radiation exposure inflicted upon the *operando* cell during continuous imaging induces significant degradation in the electrolyte of the cell, forming H_2 bubbles that can grow large enough to break the continuity of the electrolyte between

the electrodes, and kill the cell. To mitigate this issue, single images with short exposure times of 0.5 s are used in place of continuous imaging. For example, the alignment procedure says to rotate the sample stage and observe which direction the particle drifts out of the field of view using continuous imaging. A better method to accomplish this for an *operando* cell is rather than rotate an abrupt 180 ° with continuous imaging, instead rotate 1 ° and take a single image. The direction the particle is drifting out of the field of view can be determined with just a few single images at 1 ° increments, and while this places more of a burden on the researcher, the significant reduction in cell radiation exposure far outweighs any other consideration. Unfortunately, it is impossible to accurately pair the timing of an XMFlex tomography script with the unpredictable cycle rate of the capillary cell, so it is up to the researcher to manually begin a tomography at each relevant state of charge where a tomography is desired, and then continue the electrochemistry when the tomography is completed.